The Dissertation Committee for Byungki Woo Certifies that this is the approved version of the following dissertation:

Development of a Resonant Repeater Tag for the Enhancement of Sensitivity and Specificity in a Wireless Eddy Current Sensing Scheme

Committee:

Dean P. Neikirk, Supervisor

Francis X. Bostick

Mircea D. Driga

A. Bruce Buckman

Sharon L. Wood

Development of a Resonant Repeater Tag for the Enhancement of Sensitivity and Specificity in a Wireless Eddy Current Sensing Scheme

by

Byungki Woo, B.S.; M.S.

Dissertation

Presented to the Faculty of the Graduate School of
The University of Texas at Austin
in Partial Fulfillment
of the Requirements
for the Degree of

Doctor of Philosophy

The University of Texas at Austin
May 2007

Dedication

To my lovely wife Yoojin and daughter Katherine (Chae-won),
for their patience, support, and love.

Acknowledgements

I would like to thank my supervisor professor, Dean Neikirk for his support and understanding throughout my study at Austin. With only his enthusiastic guidance and brilliant insight, I could complete this dissertation. I also would like to acknowledge the members of my dissertation committee, Dr. Francis X. Bostick, Dr. Mircea D Driga, Dr. A. Bruce Buckman, and Dr. Sharon L Wood for their valuable feedback and corrections.

I would like to express my appreciation and gratitude to former and present members of Team Neikirk, especially Dr. Jooyong Kim, Dr. Young-Soo Sohn, Dr. Byunghwa Park, Dr. Sangwook Han, Dr. Matthew Andringa, Jun Wan Kim, Yoon Sok Park, Praveen Pasupathy, and Joo-Yun Jung. In addition many colleagues deserve my appreciation for their valuable advice and friendship, particularly Dr. Chul-Jae Choi, Dr. Min-Soo Noh, Dr. Sung-Bo Hwang, Hyoung-Sub Kim, Dr. Jong-Jin Lee, Dr. Jaemin Ahn and Dr. Jino Choi. I would like to acknowledge the secretarial support of Jean L Toll at Microelectronic center and Melanie Gulick at Electrical and Computer Engineering Department of the University of Texas at Austin.

I am very grateful to my parents for their efforts they have made to support me, to my parents-in-laws for their affection and encouragement. I wish to express my special thanks to not only my brothers but also brothers and sisters-in-law. Finally, I would like to express my utmost gratitude to my wife Yoojin for everything. She and my daughter, Katherine, have been a wonderful source of joy, encouragement and love to me.

Development of a Resonant Repeater Tag for the Enhancement of Sensitivity and Specificity in a Wireless Eddy Current Sensing Scheme

Publication No._____________

Byungki Woo, Ph.D.
The University of Texas at Austin, 2007

Supervisor: Dean P. Neikirk

Eddy current sensing has been successfully used in various applications from testing heat exchange tubes for nuclear power plants to assessing dielectric thickness on printed circuit boards. However, in civil infrastructures cosmetic or cementitious surface material often keeps the probe or reader coil from accessing conductive medium inside the structure, resulting in reduced coupling as the distance increases between the DUT (device under test) and probe. Thus, the direct application of existing eddy current sensing technique is not very useful to detect flaws in civil infrastructures.

To address this weak coupling problem, a simple scheme is proposed in which a resonant passive repeater tag is placed between the reader coil and the conducting test target. The feasibility of detecting defects like cracks or fractures in conductive medium using a passive resonant tag and measuring the impedance as a method of interrogation is shown. The electromagnetic waves are transmitted into and detected from a resonant tag and the conductive medium underneath the tag without direct physical contact using a reader coil above the resonant repeater tag. Experimental data taken from simple setups to demonstrate the advantage of the proposed scheme are presented. In addition, the theoretical background, such as the self and mutual inductance, and image theory, are discussed extensively. It is also shown that the theories can be applicable to build the equivalent circuit with the proper calibration process. The analyses have been carried out to characterize the responses resulting from the various experiments. Furthermore, new measurands, the effective normalized inductance and resistance, were devised and employed to reanalyze the same experimental data. An effort to construct equivalent circuit model of the system has been made to correctly predict the response without the actual experiment. To improve the process of building the equivalent circuit, the total 4 types of tags and 6 types of DUT are built and tested. The analysis is also given for the constructed equivalent circuit model.

Table of Contents

List of Tables

List of Figures

Chapter 1

Introduction

1.1 STRUCTURAL HEALTH MONITORING

The reliability of structures and the cost of maintaining the reliability are significant concerns for the owners and operators of high value and critical assets. Such structures include:

- Transportation systems and vehicles – aircraft, space vehicles, trains, ships
- Civil structures - bridges, dams, tunnels, port facilities
- Power generation – nuclear, fossil fuel and hydroelectric plants
- High-value manufactured products – launch systems, satellites, semiconductor and electronic equipment
- Industrial equipment - oil and gas exploration, production and processing equipment, chemical process facilities, pulp and paper

Until recently, it was very difficult to maintain the stability of those structures due to limitation of available technologies. For example, the inspection techniques, such as visual or acoustic inspection technique, to find out whether the structure is reliable were obsolete. Moreover, it is not easy to collect and process data generated by the inspection methods. As a result, it is usually possible to discover damages with those crude inspection methods only after they are apparent or noticeable. Due to the failure in early detection of the damage, the instability incurred to those structures is so extensive or enormous that the structures often need to be rebuilt entirely. Since it is not an easy task to collect data that reflect the condition or stress-level of the structures, traditional maintenance procedures are based on schedule-driven manuals that rely on laboratory data and analytical predictions developed during the design and manufacturing stages. Furthermore, because in-service condition and failure modes experienced by structures is generally complex and unknown, conservative calendar-based or usage-based scheduled maintenance practice, which are frequently overly time-consuming, labor-intensive, and very expensive, needs to be used. Besides, as the structures age, maintenance service frequency and cost increase while the performance and availability decrease.

However, the structural health monitoring[1], which is defined by Sandia National Laboratories as the process of implementing a damage detection strategy, provides a much better ways of maintaining the stability of highly valuable structures through many technologies available recently. First of all, it offers the promise of a paradigm shift from traditional schedule-driven maintenance to condition-based maintenance of the assets. The built-in sensor networks on the structures play an important role to provide crucial information regarding the condition, damage state, and service environment of the structures. The diagnostic information from the sensors is used for prognosis of the health and/or reliability of the structures. In addition, the same data from the sensors can facilitates the decision process with respect to inspection and repair, e.g. repair vs. no repair. Since the maintenance of the asset can be arranged and done based on the actual health and performance of the structures, only the minimum failure and maintenance cost are required while the maximum reliability and readiness can be achieved.

As stated before, the structural health monitoring needs many technologies for the best result. They can be categorized into three groups according to their role in the structural health monitoring- data generation, data acquisition, and data analysis as

---

[1] Professor P. F. Chang of Stanford University defined it as “autonomous [system] for the continuous monitoring, inspection and damage detection of [a structure] with minimum labor involvement”

illustrated in the Fig. 1.1. Various laboratory analyses, such as structure analysis, material modeling, and dynamics and sensor technology should provide clear data which is the basis of decision. Generated data by sensors or sensor network can be collected through transducer with the help of communications and signal processing. Finally, collected data which may contain noisy information should be further processed for better test result using pattern recognition and so on. The necessity of such a vast list of technology shows the interdisciplinary aspect of the structural health monitoring.

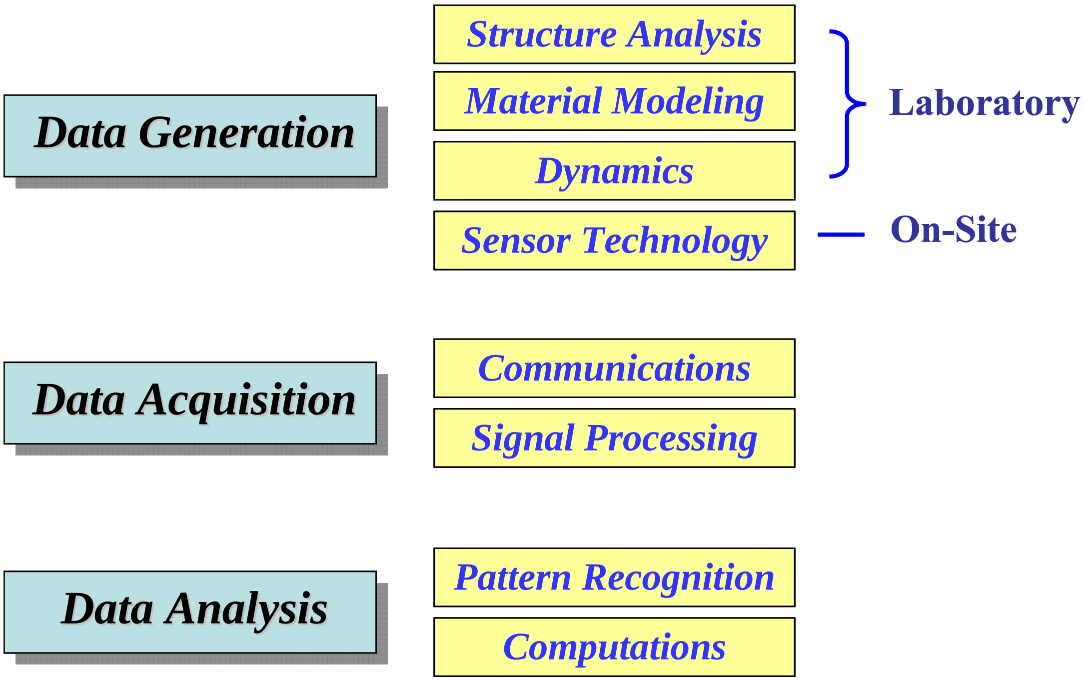

Figure 1.1: Many technologies can be categorized into three groups according to their role to the structural health monitoring- data generation, data acquisition, and data analysis.

Up to this point, the general aspect of the structural health monitoring is overviewed. However, depending on what kind of structures are monitored to maintain reliability, the specific details such as sensor technologies, method of data communications, etc. could be much different. Thus, it is our intention to focus research interest on the structural health monitoring of civil infrastructure. As a first step, overview of civil infrastructure is given next in terms of a specific target in the structural health monitoring.

1.1.1 Structural health monitoring of civil infrastructure

It is impossible to enumerate the conveniences and benefits civil infrastructures such as buildings, bridges, roadways and other such structures bring to us in our daily life. Except for the cases of rare natural disasters like an earthquake or man-made one like a bomb explosion during which structural steel and/or special moment resisting frames can be seriously damaged, the lifetime of such civil infrastructure usually depends on numerous conditions. Accordingly, it is not an easy task, by any means, to estimate the condition of such civil infrastructure and to correctly predict lifetime. Moreover, it is much harder to know when to perform preventive maintenance or repair damages before structural failure causes a serious problem or casualties.

Even in the case of earthquake the welded beam-column connections could be able to accommodate large rotations during an earthquake without damage if these structural systems are robust and ductile enough. However, critical welds were reported to be fractured in more than 200 buildings throughout the epicentral area, and structural engineers were forced to reevaluate this type of structural system after 1994 Northridge earthquake. If the buildings did not appear to have sustained serious structural damage even though critical welds were fractured by the earthquake or equivalent enormous stress, this could result in disastrous consequences. To avoid any calamity due to the neglect of possible damage done by the disturbance like earthquake, the civil structures should be checked or evaluated thoroughly. However, because the steel members are covered with cementitious materials for fireproofing, inspection of connections is difficult and expensive. Architectural finishes and fireproofing had to be removed before connections could be evaluated using ultrasonic testing techniques. The cost to the building owner was high for these inspections ($10,000 to $15,000 per joint), and the process was also disruptive to the occupants of the building. In addition, studies of buildings that sustained damage indicated that the results of structural analyses could not be used to identify the likely locations of damage within the structure. Hence, monitoring of the state or health of civil infrastructures in a simple but accurate manner has become an important subject for research at both universities and industries [1-7].

1.1.2 Nondestructive testing technique as a method of structural health monitoring of civil infrastructures

To develop a useful idea on the sensor and/or sensor networks necessary for the health monitoring of civil infrastructure, let us investigate nondestructive testing methods which are extensively used in research and industries. Nondestructive testing (NDT) has been defined as comprising those test methods used to examine an object, material or system without impairing its future usefulness. Nondestructive testing is concerned in a practical way with the performance of the test piece - how long may the piece be used and when does it need to be checked again? Therefore, nondestructive testing methods can be used for the same purpose as the structure health monitoring to maintain the performance of the object under test. However, nondestructive testing methods may be said to be a little different from the structural health monitoring in a strict sense because data for the diagnosis of the state of structures are generated on the basis of necessity, not a real-time and continuous way.

The NDT is the most actively investigated and developed methods because it saves so much expenses and efforts that other methods would have required if NDT had not been used. Modern nondestructive tests are used by manufacturers (1) to ensure product integrity, and in turn, reliability; (2) to avoid failures, prevent accidents and save human life; (3) to make a profit for the user; (4) to ensure customer satisfaction and maintain the manufacturer's reputation; (5) to aid in better product design; (6) to control manufacturing processes; (7) to lower manufacturing costs; (8) to maintain uniform quality level; and (9) to ensure operational readiness. For such benefits of the nondestructive testing, there have been developed so many different nondestructive methods which are dependent on both/either the purpose of the test and/or the characteristics of the object under the test as a result. In the table 1.1, nondestructive testing methods are classified into six major categories: visual, penetrating radiation, magnetic-electrical, mechanical vibration, thermal and chemical-electrochemical. Two additional categories are included to cover new methods. The similarity among the first six categories is that they are physical process requiring transfer of matter or energy to the object being tested. The processes described in two auxiliary categories provide transfer and accumulation of the information and evaluation of the raw signal and images common to nondestructive testing methods. The objective of each test method is tabulated in the table 1.2 according to the information about material parameters which it is intended to provide. The versatility of the nondestructive testing can be inferred from the number of applications as shown in the tables, 1.1 and 1.2.

Basic Categories	**Objectives**
Mechanical and optical	color, cracks, dimensions, film thickness, gaging, reflectivity, strain distribution and magnitude, surface finish, surface flaws, through-cracks
Penetrating radiation	cracks, density and chemistry variations, elemental distribution, foreign objects, inclusions, microporosity, misalignment, missing parts, segregation, service degradation, shrinkage, thickness, voids
Electromagnetic and electronic	alloy content, anisotropy, cavities, cold work, local strain, hardness, composition, contamination, corrosion, cracks, crack depth, crystal structure, electrical and thermal conductivities, flakes, heat treatment, hot tears, inclusions, ion concentrations, laps, lattice strain, layer thickness, moisture content, polarization, seams, segregation, shrinkage, state of cure, tensile strength, thickness, disbonds
Sonic and ultrasonic	crack initiation and propagation, cracks, voids, damping factor, degree of cure, degree of impregnation, degree of sintering, delaminations, density, dimensions, elastic moduli, grain size, inclusions, mechanical degradation, misalignment, porosity, radiation degradation, structure of composites, surface stress, tensile, shear and compressive strength, disbonds, wear
Thermal and infrared	bonding, composition, emissivity, heat contours, plating thickness, porosity, reflectivity, stress, thermal conductivity, thickness, voids

Chemical and analytical	alloy identification, composition, cracks, elemental analysis and distribution, grain size, inclusions, macrostructure, porosity, segregation, surface anomalies
Auxiliary Categories	**Objectives**
Image generation	dimensional variations, dynamic performance, anomaly characterization and definition, anomaly distribution, anomaly propagation, magnetic field configurations
Signal image analysis	data selection, processing and display, anomaly mapping, correlation and identification, image enhancement, separation of multiple variables, signature analysis

Table 1.1: Nondestructive testing methods categories [8-10].

Objectives	**Attributes Measured or Detected**
Discontinuities	
Surface anomalies	roughness, scratches, gouges, crazing, pitting Inclusions and imbedded foreign material
Surface connected anomalies	cracks, porosity, pinholes, laps, seams, folds, inclusions
Internal anomalies	Cracks, separations, hot tears, cold shuts, shrinkage, void, lack of fusion, pores, cavities, delaminations, diabonds, poor bonds, inclusions, segregations

Structure	
Microstructure	molecular structure, crystalline structure and/or strain, lattice structure, dislocation, vacancy, deformation
Matrix structure	gain structure, size, orientation and phase, sinter and porosity, impregnation, filler and/or reinforcement distribution, anisotropy, heterogeneity, segregation
Small structural anomalies	leaks(lack of seal or through-holes), poor fit, poor contact, loose parts, loose particles, foreign objects
Gross structural anomalies	assembly errors, misalignment, poor spacing or ordering, deformation, malformation, missing parts
Dimensions and metrology	
Displacement, position	linear measurement, separation, gap size, discontinuity size, depth, location and orientation
Dimensional variations	unevenness, nonuniformity, eccentricity, shape and contour, size and mass variations
Thickness, density	film, coating, layer, plating, wall and sheet thickness, density or thickness variations
Physical and mechanical properties	
Electrical properties	resistivity, conductivity, dielectric constant and dissipation factor
Magnetic properties	polarization, permeability, ferromagnetism, cohesive force

Thermal properties	conductivity, thermal time constant and thermoelectric potential
Mechanical properties	compressive, shear and tensile strength (and moduli), Poisson's ratio, sonic velocity, hardness, temper and embrittlement
Surface properties	color, reflectivity, refraction index, emissivity
Chemical composition and analysis	
Elemental analysis	detection, identification, distribution and/or profile
Impurity concentrations	contamination, depletion, doping and diffusants
Metallurgical content	variation, alloy identification, verification and sorting
Physiochemical state	moisture content, degree of cure, ion concentrations and corrosion, reaction products
Stress and dynamic response	
Stress, strain, fatigue	heat-treatment, annealing and cold-work effects, residual stress and strain, fatigue damage and life (residual)
Mechanical damage	corrosion, stress corrosion, phase transformation
Other damage	radiation damage and high frequency voltage breakdown

Dynamic performance	crack initiation and propagation, plastic deformation, creep, excessive motion, vibration, damping, timing of events, any anomalous behavior
Signature analysis	
Electromagnetic field	potential, strength, field distribution and pattern
Thermal field	isotherms, heat contours, temperatures, heat flow, temperature distribution, heat leaks, hot spots
Acoustic signature	noise, vibration characteristics, frequency amplitude, harmonic spectrum and/or analysis, sonic and/or ultrasonic emissions
Radioactive signature	distribution and diffusion of isotopes and tracers
Signal or image analysis	image enhancement and quantization, pattern recognition, densitometry, signal classification, separation and correlation, discontinuity identification, definition (size and shape) and distribution analysis, discontinuity mapping and display

Table 1.2: The Objectives of nondestructive testing methods [8-10].

1.1.3 The challenges for the conventional nondestructive eddy current testing technique

With the knowledge of the nondestructive testing, it is necessary to find out what id the crucial information to maintain the reliability of the civil infrastructures. That means what should be monitored to satisfy the purpose of the structural health monitoring described earlier. Since the modern civil infrastructure are mostly built with reinforced concrete or structural steels or special moment resisting frames which often support whole structures, it is important to monitor the condition of those key units to ensure the proper performance of civil infrastructures. Accordingly, it is appropriate to use a sensor technology related to the electromagnetic and electric nondestructive testing methods in the table 1.1 so that the good conductivity of steel or frames can be properly exploited.

Finally, to find an accurate but easily implementable evaluation method for the civil infrastructures, the eddy current nondestructive testing method - one of the electromagnetic and electric nondestructive testing methods - was chosen as the starting point for the study of the sensor technology needed for the structural health monitoring because it uses the conducting properties of object under test for the operation. Furthermore, new theoretical studies and experiments about the eddy current effect are performed to take advantages of technological advances in related areas; hence, nondestructive testing method using the eddy current is a more accurate and time-saving application than ever before.

However, it is not an easy task to get information on the condition of the steel beam or rebar located deep in the cementitious materials simply by scanning the surface with the conventional eddy current nondestructive testing equipment to conduct the structural health monitoring of civil infrastructures because the distance between the equipment and object under test can be an obstacle to the acquisition of a correct data without any direct connection from the testing instrument to the object under test as illustrated in Fig. 1. 2.

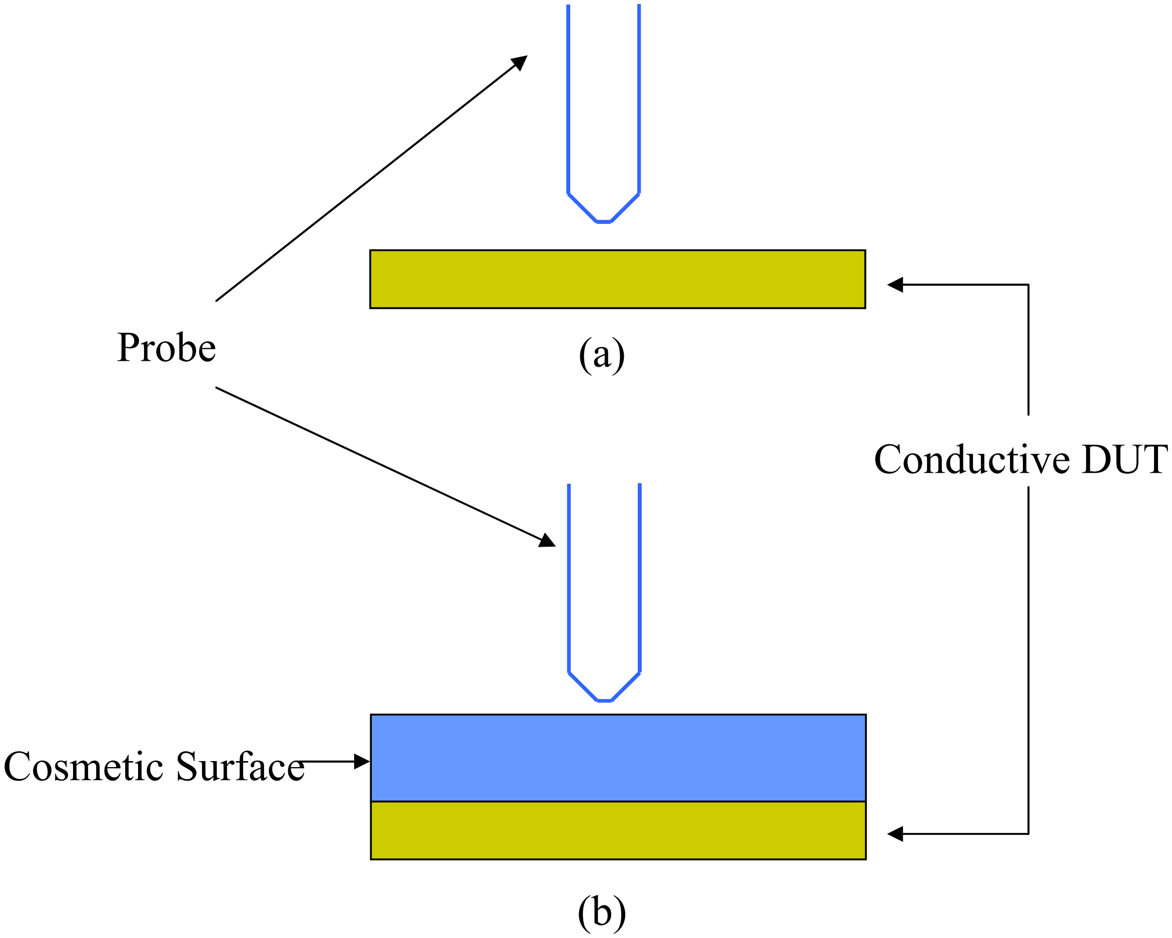

Figure 1.2: The challenges for adopting the conventional nondestructive eddy current testing method for the health monitoring of civil infrastructures (a) The probe can be brought very close to the surface of device under test in conventional nondestructive testing (b) It is not an easy task to get information on the condition of the steel beam or rebar located deep in the cementitious materials simply by scanning the surface with the traditional eddy current nondestructive testing equipment to conduct the structural health monitoring of civil infrastructures.

1.2 BACKGROUND RELATED TO THE EDDY CURRENT NONDESTUCTIVE TESTING

A brief historical overview of the eddy current phenomenon, followed by a set of present NDT technique using it is presented here. Then, various factors are introduced that will affect the response of materials under the test when an eddy current technique is applied. More involved topics on the eddy current can be found in the literature [11-16].

1.2.1 A short history of the eddy current

To understand the phenomenon of eddy current better, the electromagnetic induction discovered by Michael Faraday in 1831 is explained in the followings.

Faraday constructed various coils of wire by winding two conductors so that they should lie very close together while still separated by a cloth or a paper insulation as illustrated in Fig. 1.3. One conductor would form a circuit with the galvanometer. Through the other he would send a strong current from a battery. There was, disappointingly, no deflection of the galvanometer. However, he noticed a very slight disturbance of the galvanometer when the current was switched on and another when it was switched off. Pursuing this lead, he soon established beyond doubt that current in other conductor are induced, not by a steady current, but by a changing current. This is the effect that causes the eddy current to flow in the material. That is to say, an eddy current is the motion of electric charges induced entirely within a conducting material by a varying electric or magnetic field or by electromagnetic waves.

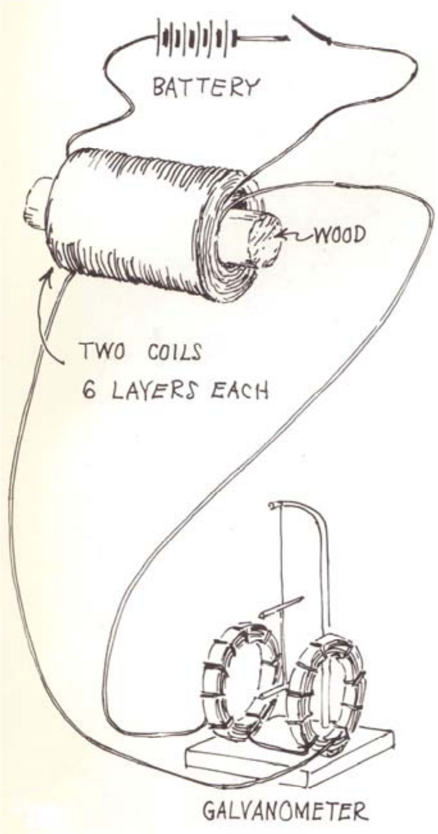

Figure 1.3: A possible illustration of Faraday's experiments described in his Experimental Researches in Electricity [17].

The direction of the induced eddy current or emf (electromotive force) from electromagnetic induction can be determined by the Lenz's law which states that the electromotive force induced in an electric circuit always acts in such a direction that the current it drives around a closed circuit produces a magnetic field which opposes the change in magnetic flux which produces the electromotive force. If the current flows clockwise in the loop in Figure 1.4, the induced eddy current in the bottom conductor should flows counterclockwise to counteract the magnetic flux produced by the current in the loop.

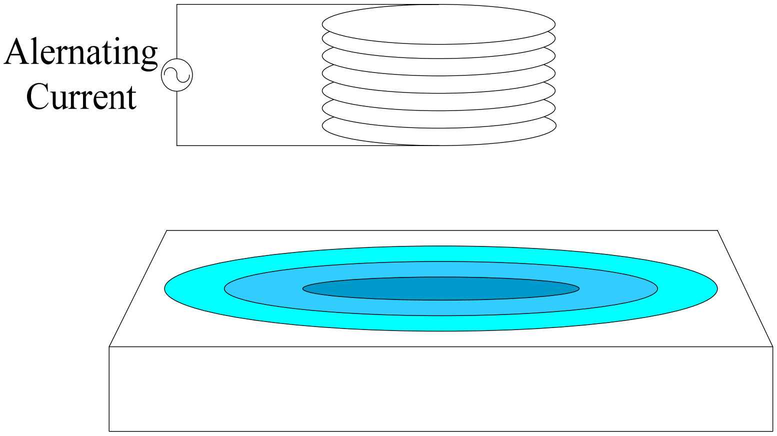

Figure 1.4: Induction of the eddy current in the conductive medium using an alternating current in the driving loop.

Eddy current was also called as Foucault current named after a French scientist who discovered the existence of it in a copper disk moving in a strong magnetic field [18]. In his experiments with an apparatus called Foucault's disk in Fig. 1.5, a geared-up copper wheel was rotated in the gap of an electromagnet. With no current through the magnet coils the wheel rotated easily. As soon as the magnet was energized, resistance to rotation was felt and the copper disk started to heat up. In one experiment, the temperature of the disk rose from 10ºC to 61ºC.

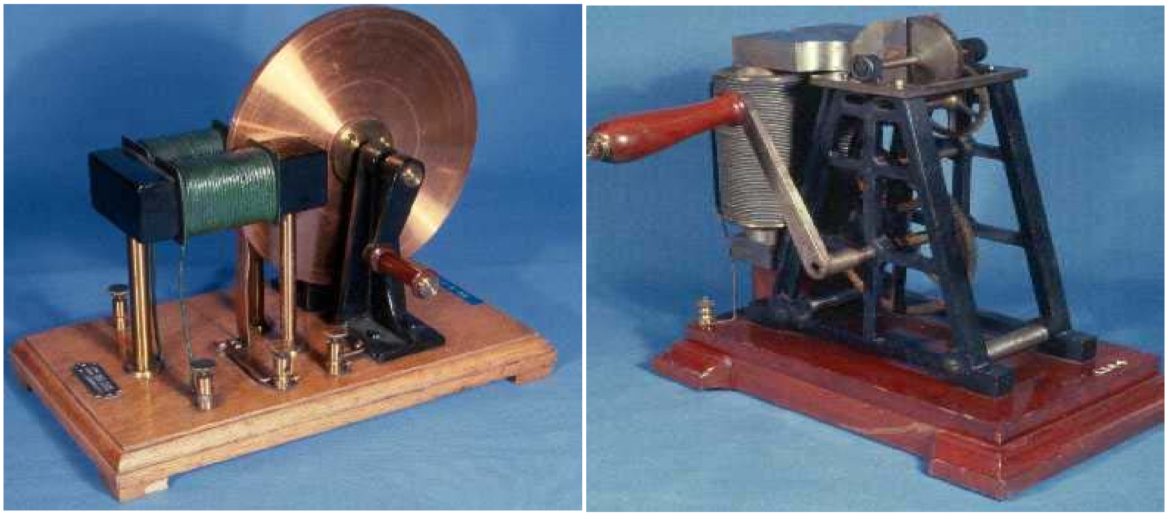

Figure 1.5: Foucault's disk [19].

In 1879 Hughes discovered that when a coil was brought into contact with metals of different conductivities and/or permeabilities with an alternating current flowing through it, the properties of the coil changed in accordance with the characteristics of metals. However, use of the eddy current method developed slowly, probably because such an inspection method was not needed and because further development of the electrical theory was necessary before it could be used for practical applications.

Vigners, Dinger, and Gunn described eddy current type flaw detectors for nonmagnetic metals in 1942, and in the early 1940s, Förster and Zuschlag developed eddy current inspection instruments. Based on these improvements of theory and practicality, eddy current methods were put into practical use for testing materials after the Second World War. For practical applications, particularly in the aircraft and nuclear industries, enormous research was done in the 1950s and 60s. As a result of much works, eddy current testing is now an accurate and well understood inspection technique.

1.2.2 The eddy current nondestructive testing techniques in use

Applications using eddy current encompass so wide range of capabilities that it is not suitable to explain all of them in this document. However, to see how eddy current testing methods are used in real life, a couple of examples are going to be explained below.

First, in petrochemical or power generation application [20-22], thousands of tubes are being used for heat exchange operation in which the contaminated water flows on one side of the tube (inside or outside) and the fresh water flows on the other side. The heat is transferred from the contaminated water to the fresh water and the fresh water is then returned back to its source, which is usually a lake or river.

Figure 1.6: NDT(Nondestructive Testing) technique of heat exchange tubing using eddy current [23].

Especially in a nuclear reactor, contamination of fresh water, which will be returned to the environment, may cause catastrophic problem. Thus, it is very important to keep the two water sources from mixing. To serve that purpose, the tubes and other equipment must be inspected as shown in the Fig. 1.6 and repaired periodically with power plants being shutdown. The eddy current test method and the related remote field testing method provide not only high-speed inspection techniques for these applications but also allow accurate estimation of the remaining life of the tubes so that an appropriate action on the tubes under the test can be determined according to the test result.

Another possible application of the eddy current is to assess the thickness of a coating or a wall, which may be non-conductive or conductive. The effect of liftoff on impedance is used to determine the thickness of nonmetallic coatings on metal substrates. This method has widespread use for measuring thickness of paint and plastic coatings. The coating serves as a spacer between the probe and the conductive surface. As the distance between the probe and the conductive base metal increases, the eddy current field strength decreases because less of the probe's magnetic field can interact with base metal. Thickness between 0.5 and 25 μm can be measured to an accuracy within 10% for lower values and 4% for higher values [24]. Contributions to impedance changes due to the conductivity variations should be phased out, unless it is known that the conductivity variations are negligible, as normally found at higher frequencies. Fairly precise measurements can be made with a standard eddy current flaw detector and a calibration specimen. For more complex case, where the coating is conductive, the following needs to be taken into consideration. The two materials must have different conductivities and/or relative permeabilities, and the top coating must be non-magnetic. Frequency of operation should be chosen so that it will make the effective depth of penetration equal to the nominal wall thickness. If the surface coating has higher resistivity than the lower coating, then by using a frequency that is sufficiently low to penetrate the surface coating, results will be similar to that for non-conductive coatings. Figure 1.7 illustrates some of the possible eddy current applications.

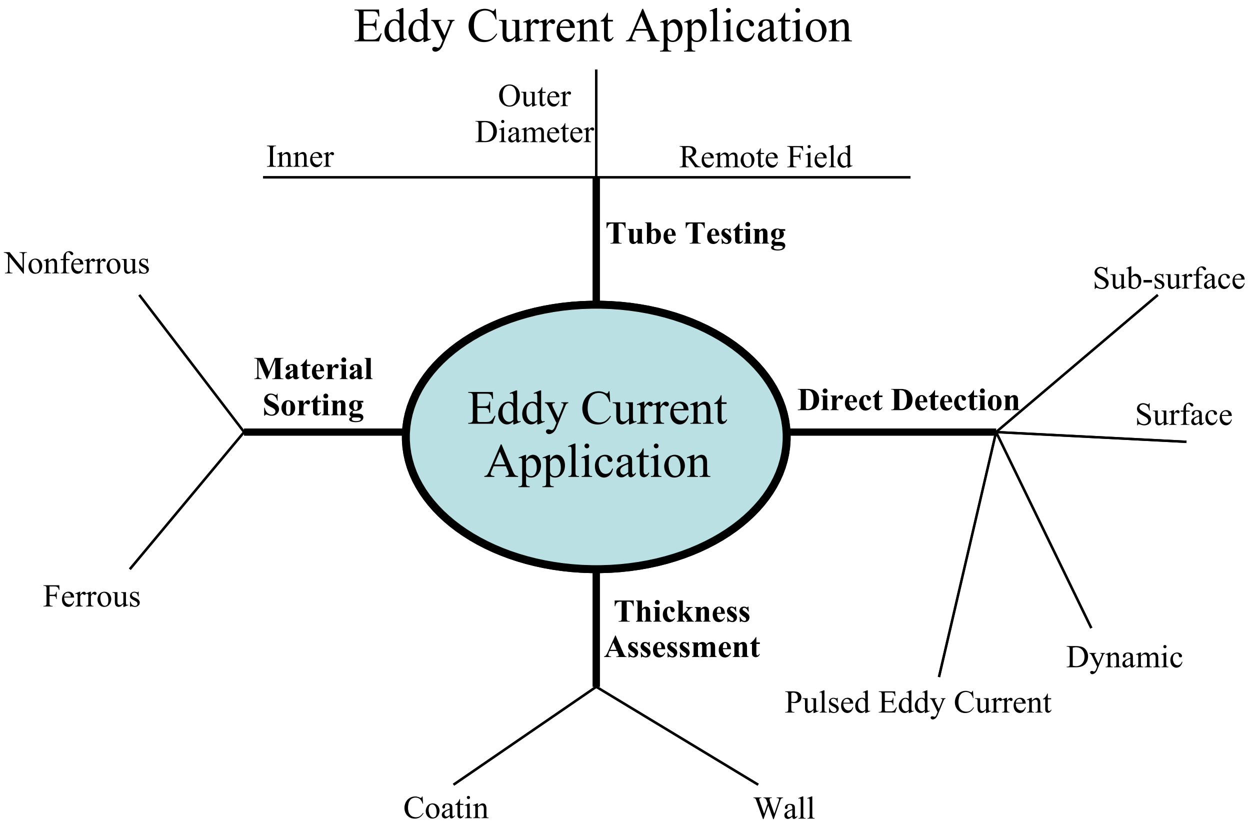

Figure 1.7: Illustration of some of possible eddy current application [25].

1.2.3 Factors affecting eddy current response [26]

To find an accurate but easily implementable and nondestructive evaluation method for the civil infrastructures, various factors should be taken into consideration that will affect the response of materials under test when an eddy current technique is applied. Although the generation of eddy currents is due to a time-varying field, it should be noted that the characteristics of the eddy current response are strongly affected by a number of factors. Therefore, it is worthwhile to consider material properties, material shapes, and operating conditions that control the eddy current response.

1. Material conductivity

The conductivity of a material has a very direct effect on the eddy current flow: the greater the conductivity of the material, the greater the flow of eddy currents on the surface. Conductivity is often measured by an eddy current technique, and inferences can then be drawn about the different factors affecting the conductivity, such as material composition, heat treatment, and work hardening.

2. Material Permeability

This may be described as the ease with which a material can be magnetized. For non-ferrous metals such as copper, brass, and aluminum, and for austenitic stainless steels the permeability is the same as that of ‘free space’, i.e., the relative permeability is one. For ferrous metals, however, the value of relative permeability may be several hundred, and this has a very significant influence on the eddy current response. In addition, it is not uncommon for the permeability to vary greatly within a metal part due to localized stresses and heating effects.

3. Frequency

If a single frequency is used for locating cracks, the eddy current response is greatly affected by the test frequency. That is because there are two contradicting effects of the frequency on eddy current response. First, the eddy current is damped while penetrating into the conductor (penetration effect). Thus, frequency dependence of the penetration implies that for deep lying cracks, low frequencies must be used for obtaining a sufficient current density in the vicinity of the crack. Secondly, due to the induction law, the induced current density at the surface is diminished when using lower frequency. Therefore, in total, there is a certain excitation frequency which results in a maximum response field from the crack. Fortunately, this is one of the properties we can control.

4. Geometry

Since it is rare that an ideal geometric condition exists in real objects or materials, such as perfectly flat surfaces or samples of infinite size, geometrical features such as curvature, edges, and grooves will exist and will affect the eddy current response. Test techniques must recognize this. For example, the probe will normally be moved along parallel to the edge so that small changes may be easily detected in testing an edge for cracks. Where the material thickness is less than the effective depth of penetration this will also affect the eddy current response.

Although the generation of eddy currents is due to a time-varying field, it should be noted that the characteristics of the eddy current response is strongly affected by a number of factors. Therefore, it is worthwhile to consider material properties, material shapes, and operating conditions that control the eddy current response.

1.3 COMPARISON BETWEEN CONVENTIONAL AND PROPOSED SCHEME

1.3.1 Conventional eddy current nondestructive testing

The eddy current NDT technique, which is illustrated with a block diagram in the Figure 1.8, is successfully used as a method for monitoring the condition of fail-critical components like airplane propeller blades, power plant gas turbine blades, and surface on the wings of airplanes.

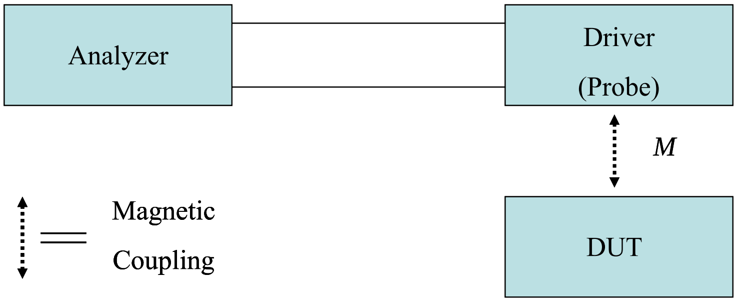

Figure 1.8: The block diagram for the conventional eddy current nondestructive testing technique.

Nonetheless, it is not easy to apply the present eddy current NDT method to health monitoring for civil infrastructures because present eddy current applications are developed under the assumption that the surface of inspected material would be accessible to the probe. Therefore, the rough surface finish, as is often the case with civil infrastructures, may degrade the sensitivity of a detection test. Another important limitation that should be taken into consideration is that there is not the strong enough magnetic coupling between driver and DUT due to the considerable gap between the driver and material under inspection. Thus, the read range of present eddy current NDT technique is not long enough to ensure the direct application of present techniques to the health monitoring of civil infrastructures in which objects under the test are usually embedded deeply in the surface material far from the probe.

1.3.2 Proposed scheme using passive repeater tag and its benefits

To address the limitation inherent to the present eddy current NDT application and improve the sensitivity, our proposed scheme is to place an additional passive repeater close to DUT like steel bar (or rebar), as illustrated in Fig. 1.9.

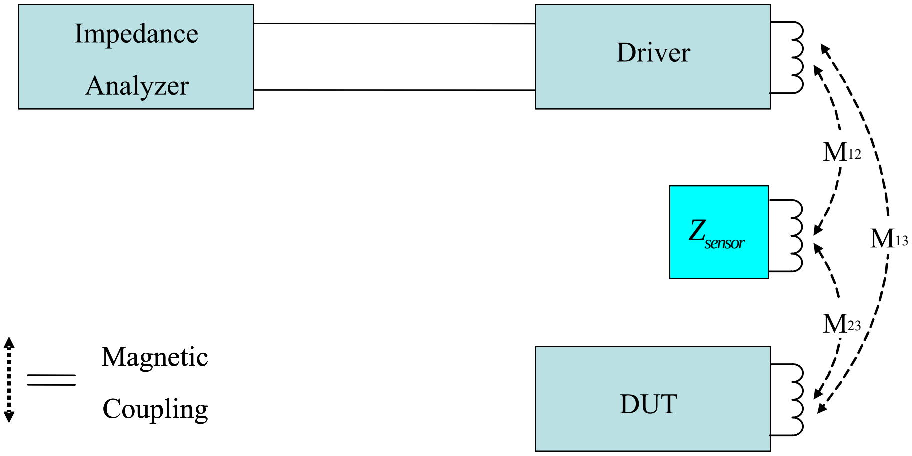

Figure 1.9: Block diagram for the proposed system using additional passive repeater located between the driver and the DUT.

The inserted passive repeater has different characteristics depending on how much the condition of DUT has changed so that the properties of the sensor can be exploited to detect the status of the DUT. For example, the total impedance looking into the driver from the impedance analyzer can be used to determine the status of the DUT if the inserted passive repeater has characteristics of varying impedance according to the state of the DUT.

Here we limit the inserted repeater to be passive, which can be represented as an equivalent circuit element having impedance, Z_{sensor}, which may be frequency-dependent, connected to a transformer representing the induced currents generated by the AC current in the driver coil. The reason we choose passive elements as a performance enhancer is obvious if we compare the lifetime of civil infrastructures with that of a battery in a powered sensor. Active sensors with their own power supplies may provide more information and better sensitivity; however, it also raises the cost and effort necessary whenever the batteries would need to be replaced due to their shorter life cycle compared to civil infrastructure. Moreover, a passive repeater can be more cost-effective than active sensors which may require expensive IC processing and packaging.

Given that the repeater should be passive and modeled as an impedance of Z_{sensor}, it is worthwhile to see how two extreme values of Z_{sensor} affect the total impedance seen at the impedance analyzer. First, let us consider the case when Z_{sensor} is infinite. It is evident that there is no change at all in the total impedance because no eddy current can be induced in the passive repeater to reflect the condition of the DUT below the passive repeater. On the other hand, if a short-circuited passive element is inserted, the driver would induce more eddy current in the repeater that would then screen the effect of the DUT on the driver. Consequently, even if two completely different types of DUTs are placed under a short-circuited passive repeater, changes in the total impedance can hardly be detected due to the screening effect of a short-circuited repeater.

Among the possible candidate configurations for a passive repeater, an LC resonant circuit can satisfy our requirements for the passive repeater in a simple manner. The basic idea of using an LC resonant circuit as a passive repeater is that the resonant frequency of the circuit depends on the state of the material under test. For example, if a highly conductive material lies right below a passive repeater, the induced eddy current in the conducting medium changes the effective inductance of the passive repeater, which results in a shift of resonant frequency of the passive repeater.

However, whenever there happens to be changes in the conductive DUT, such as flaws or cracks, they would block the path of induced eddy current and force it to flow in a different route. That hindrance of normal current flow makes the induced eddy current in the DUT have less effect on the passive repeater. Thus, the resonant frequency of the passive repeater does not shift as much as the case when there are no defects in the DUT.

Likewise, since the corrosion process on the surface of steel bar would decrease the induced eddy current in the material under test due to reduced conductivity, it would not shift resonant frequency of the passive repeater as much as the case when there is no corrosion on the surface of a steel bar. Hence, it may also be possible to use this type of repeater as a corrosion detector. In summary, the overall response of whole system including driver, passive repeater, and material under test depends on how much the resonant frequency is shifted from original one.

However, it should be mentioned that since any metallic object that comprises the inductor component has its own resistance, a realistic circuit model of the proposed passive repeater is actually an RLC resonant circuit. Thus, the passive repeater consists of resistive (R), inductive (L), and capacitive (C) components. A series resonant circuit configuration was selected to be used as a passive repeater for the enhancement of sensitivity. The reason for choosing the series RLC resonant circuit as the repeater rather than a parallel RLC circuit is because the series circuit has the lowest impedance value at the resonant frequency so that the induced eddy current in the sensor will be maximized at that frequency

In addition to the enhanced sensitivity, a series RLC resonant arrangement can minimize the effect of surroundings on the target or material because it uses locally limited current distribution - the eddy current is induced right beneath and very close to the sensor - to locate defects. The proposed design can be considered as a sort of wireless point sensor because it does not need any electrical connection to the sensor and sample material under the sensor. No explicit connection from the sensor to the driver makes it easier to use and leads to a low loading effect. If the driver and the sensor have the correct geometry they can be modeled accurately in an equivalent circuit and a wide range of operating frequencies can be chosen.

For example, an EAS (Electronic Article Surveillance) tag, which is a very common form of passive wireless sensor, can be modeled as a series RLC resonant circuit. Therefore, it can be used as a sensor in our proposed scheme with little modification. That means the cost of building a sensor can be very low as the fabrication process is relatively simple and fully developed. Thus, manufacturability of the proposed sensor system can be quite excellent.

Chapter 2

Preliminary Experiment

2.1 INTRODUCTION

To verify the idea presented in the previous section, a series of measurement has been taken using an HP 4194A Impedance/Gain-Phase Analyzer. If the driver configuration and cabling to the impedance analyzer are fixed as in the Figure 1.9, it is the sensor and the DUT that can change the system impedance seen at the impedance analyzer in our proposed method. However, only the DUT can be a loading to the driver in the conventional eddy current NDT scheme. Thus, for comparison of the sensitivities between the proposed and conventional method, the fixed distance between the driver and the DUT was used for the whole experiment. With the fixation of the distance between the driver and the DUT, it is only the sensor that can change the total response seen at test equipment. Consequently, whether the sensor inserted in between the driver and the DUT would improve the sensitivity or not can be determined by comparing the system impedance data of each incident acquired from impedance analyzer.

2.2 THE SYSTEM IMPEDANCE RESPONSE USING CONVENTIONAL SCHEME

The magnitude and phase plot of the system impedance are given in the Figure 2.1 when only the driver is present for the measurement. The driver is about 3 turns of wire which are tightly wound on a hollow cylinder of a circular cross section with a radius of 2.6cm. As can be seen in the data plot, the magnitude is monotonically increasing, but phase is almost constant in the frequency range of interest.

(a)

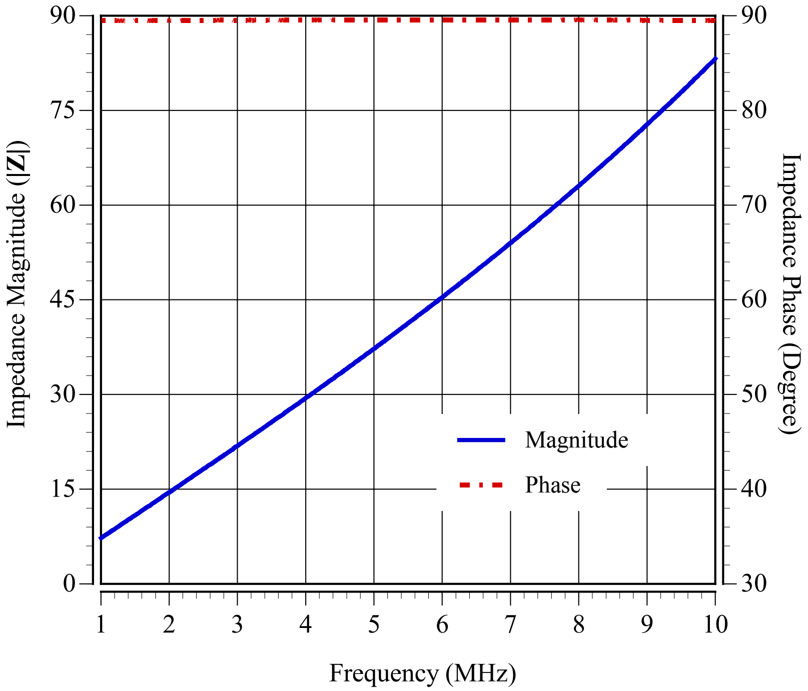

(b)

Figure 2.1: (a) The experiment setup for the impedance measurement. (b) The magnitude and phase of the system impedance when only the driver is connected to the impedance analyzer.

Figure 2.2 shows a swept-frequency measurement of the system impedance when both driver and DUT were present in the system. A copper coated plate was used as DUT and was apart about 3cm from driver. Next plot shown in Figure 2.3 was measured in exactly same condition as Figure 2.2 except that a copper coated plate has a slit in it and the driver was divided into two parts by the slit when seen from above as in Figure 2.3d.

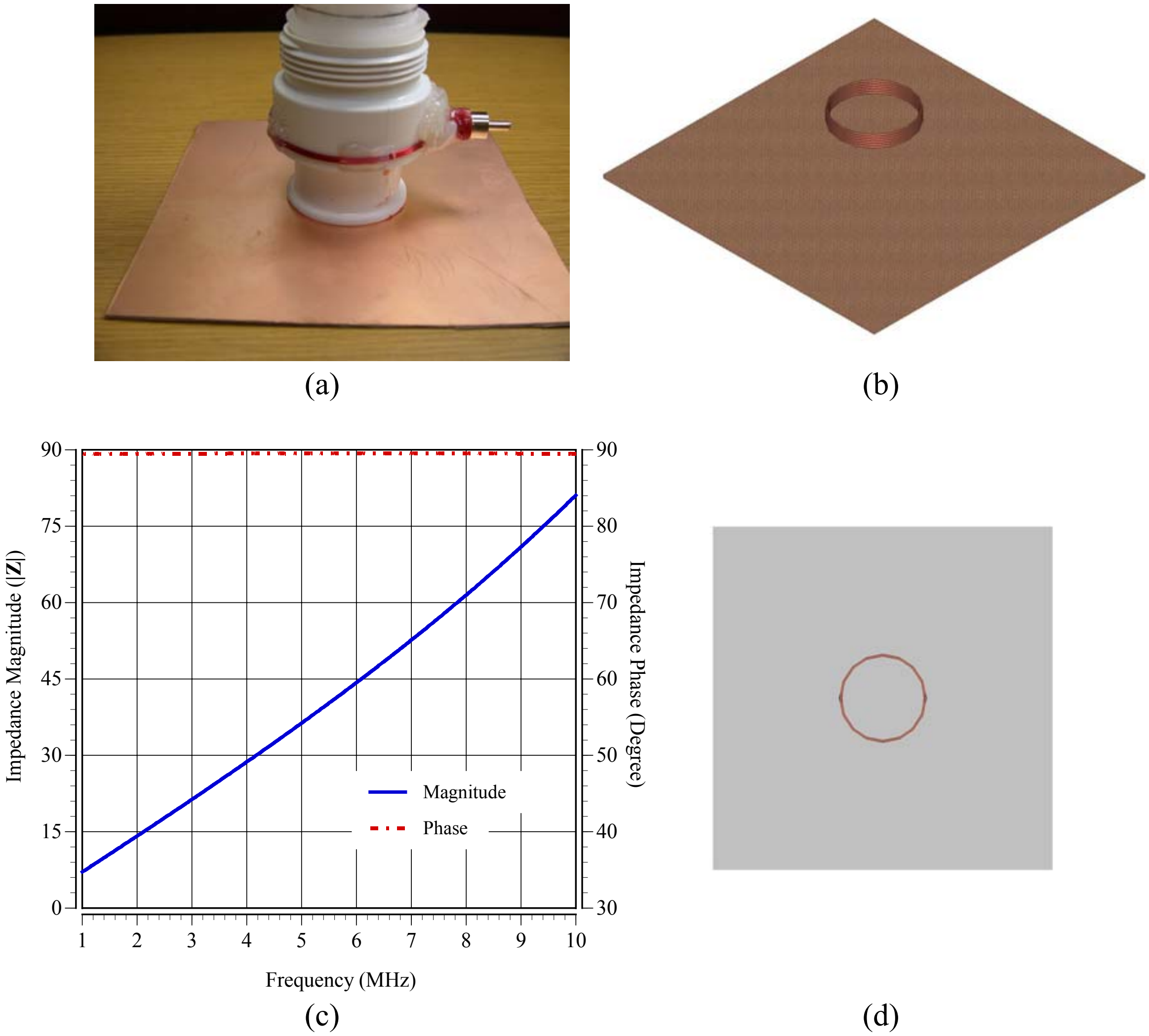

(a) (b)

(c) (d)

Figure 2.2: (a) The experiment for the system impedance measurement (b) Illustration of experimental setup: a coil is located 3cm above copper plate (c) The system impedance plot (magnitude and phase) when both driver and DUT were present in the system. A copper coated copper plate was used as DUT and apart about 3cm from driver (d) Top-down view of experimental setup.

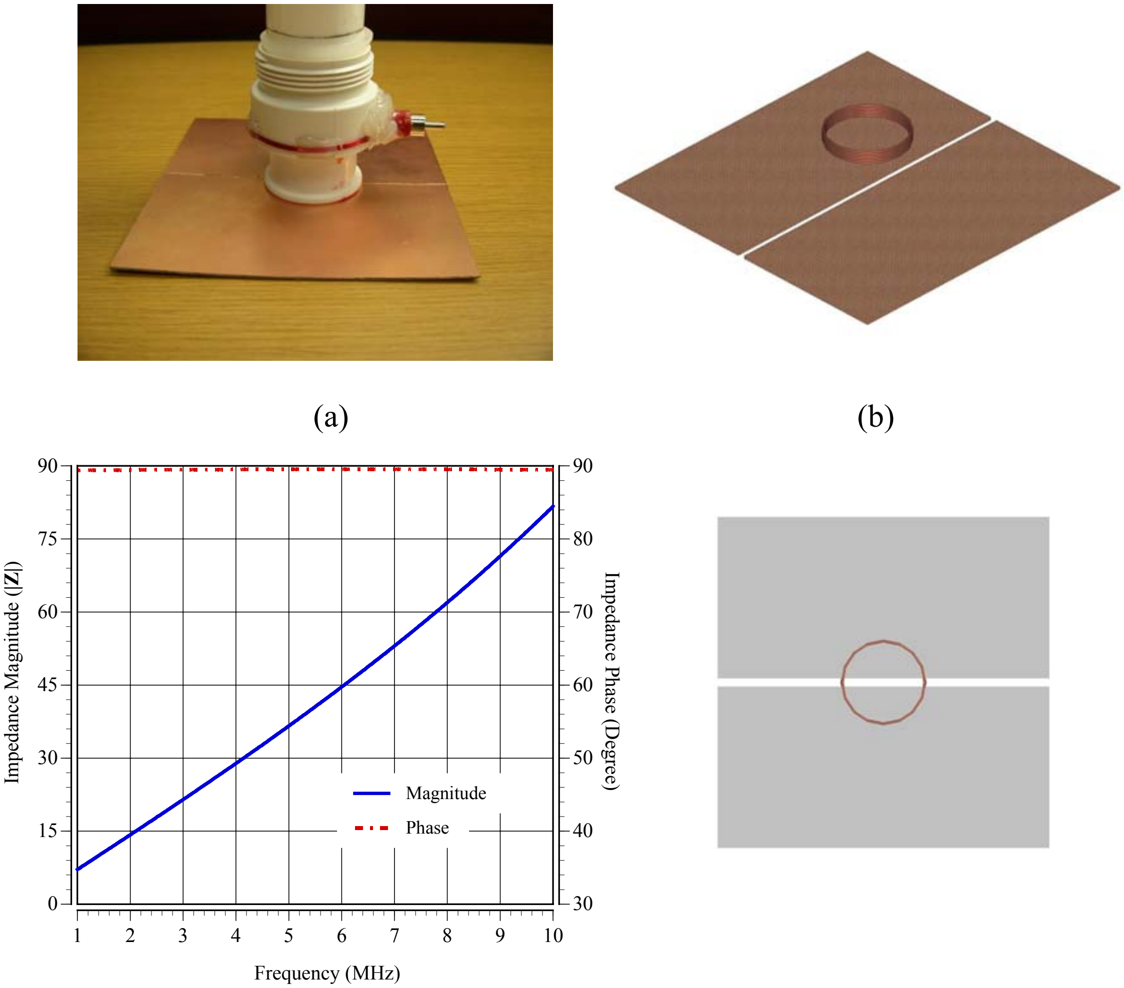

(a) (b) (c) (d)

Figure 2.3: (a) The experiment for the impedance measurement (b) Illustration of experimental setup: a coil is located 3cm above copper plate which has a slit in it (c) Magnitude and phase of the system impedance drawn from exactly same condition as Figure 2.2 except that a copper coated copper plate has slit in it and driver was located right above it. The driver was divided into two parts by the slit when seen from above. (d) Top-down view of experimental setup.

Although the condition of the DUT in the Figure 2.3 is totally different from that of the DUT used for the Figure 2.2, any noticeable difference between them cannot be found. Moreover, those two system impedance plots in Figure 2.2 and 2.3 are almost identical to the one that was taken when only the driver was considered. It can be inferred from the above results that the induced eddy currents do not affect the driver loop even in highly conductive material like copper coated copper plate if the driver is located further than 3cm from the copper plate in our test experiment setup. Consequently, if it is necessary to remotely detect a crack or slit in the conductive medium without a direct connection, utilization of a conventional eddy current technique does not provide enough sensitivity to determine correct status of copper plate which is a DUT of test experiment.

2.3 THE SYSTEM IMPEDANCE RESPONSE USING PROPOSED SCHEME

Next plot in the Figure 2.4 is the impedance extracted from measurement when only a series RLC resonant circuit loads the driver. The inflection of magnitude and dip of phase response occur at the resonant frequency of the sensor and are given by [27]

$$f = \frac{1}{2\pi\sqrt{L_{sensor}C_{sensor}}} \tag{2.1}$$

where L_{sensor} is the inductance of the sensor and C_{sensor} is the capacitance of the sensor.

The Figure 2.4 was used as a reference to determine how much change has occurred when conductive mediums with different states were brought close to the sensor.

(a)

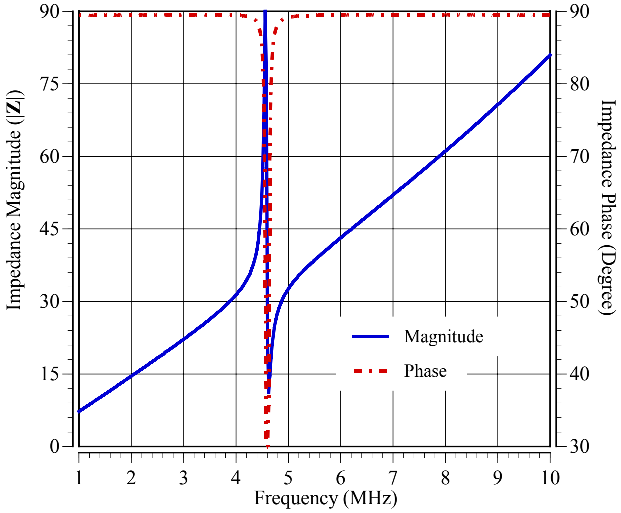

(b)

Figure 2.4: (a) The experiment for the impedance measurement (b) The system impedance extracted from measurement when only a series RLC resonant passive repeater loads the driver.

The system impedance shown in the Figure 2.5 is taken when proposed sensor was inserted between the driver and a non-defective copper plate. From the Lenz's law, it is expected that there are induced eddy currents both in the sensor loop and the copper plate. However, the direction of the currents is opposite to each other. Then, the opposite polarity of the currents results in the reduction of effective inductance of the sensor loop. As a result, the inflection of the magnitude response is shifted to higher frequency than one in the Figure 2.4, and the dip of phase response is diminished significantly.

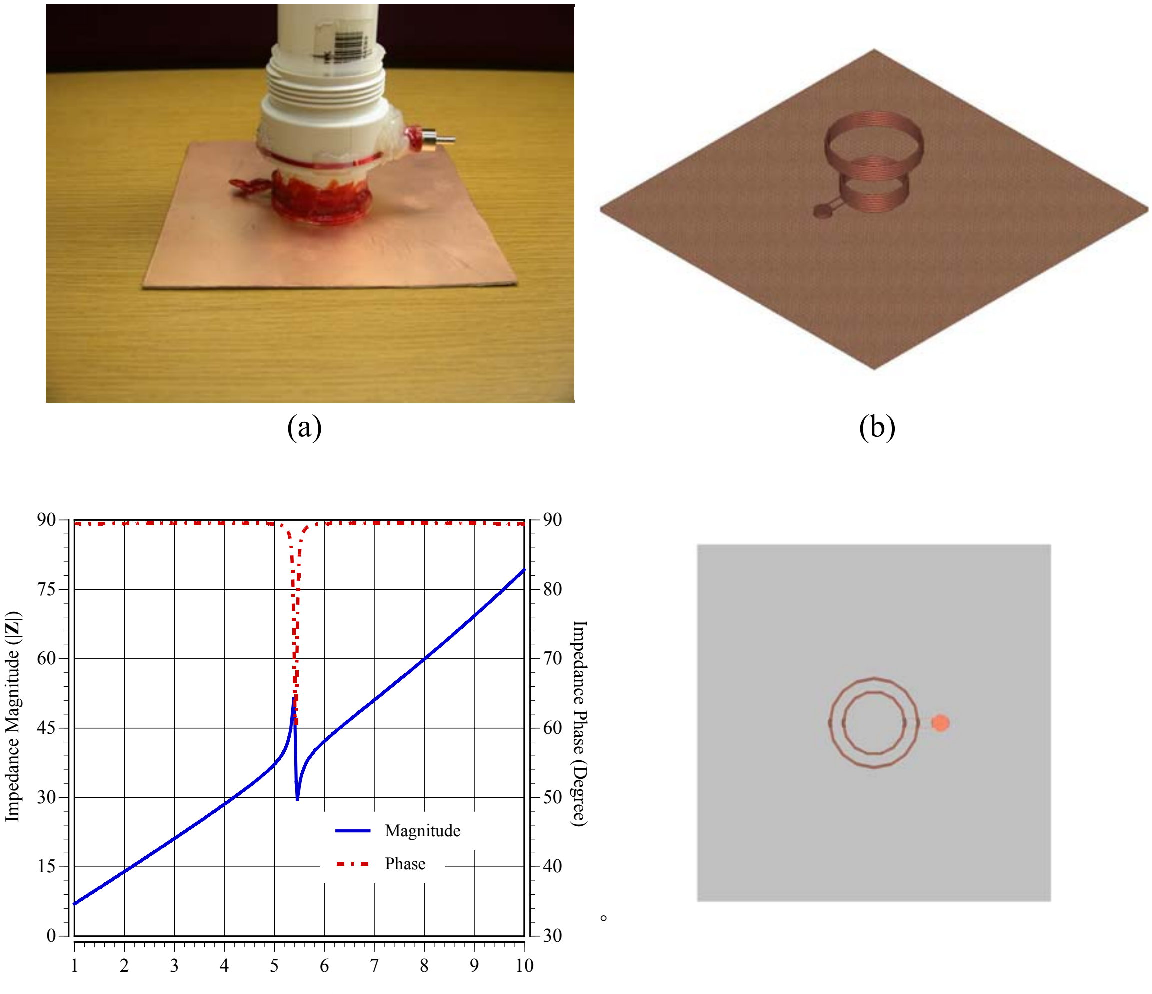

(a) (b) (c) (d)

Figure 2.5: (a) The experiment for the impedance measurement (b) Illustration of experimental setup: a coil is located 3cm above copper plate and a passive repeater is 2.7cm apart from driver (c) The impedance taken when proposed series RLC resonant circuit sensor was inserted between the driver and copper plate without slit. (d) Top-down view of experimental setup.

If there is a slit which causes a discontinuity in the path of eddy current induced in the copper plate used as a DUT, the mutual interaction between the sensor and the DUT will dramatically be weakened depending on the size of slit. Accordingly, if a sensor is placed some distance above a slit in a way that it (slit) halves the projected image of a circular-shaped sensor onto copper plate, magnitude of the eddy in the sensor is not much different from the case when there is no copper plate below the sensor. Thus, as can be seen in the Figure 2.6, the inflection frequency of the total impedance does not shift much from the original resonant frequency of the sensor compared to the response shown in the previous Figure 2.5. Note also that the phase dip is deeper than that in the Figure 2.5.

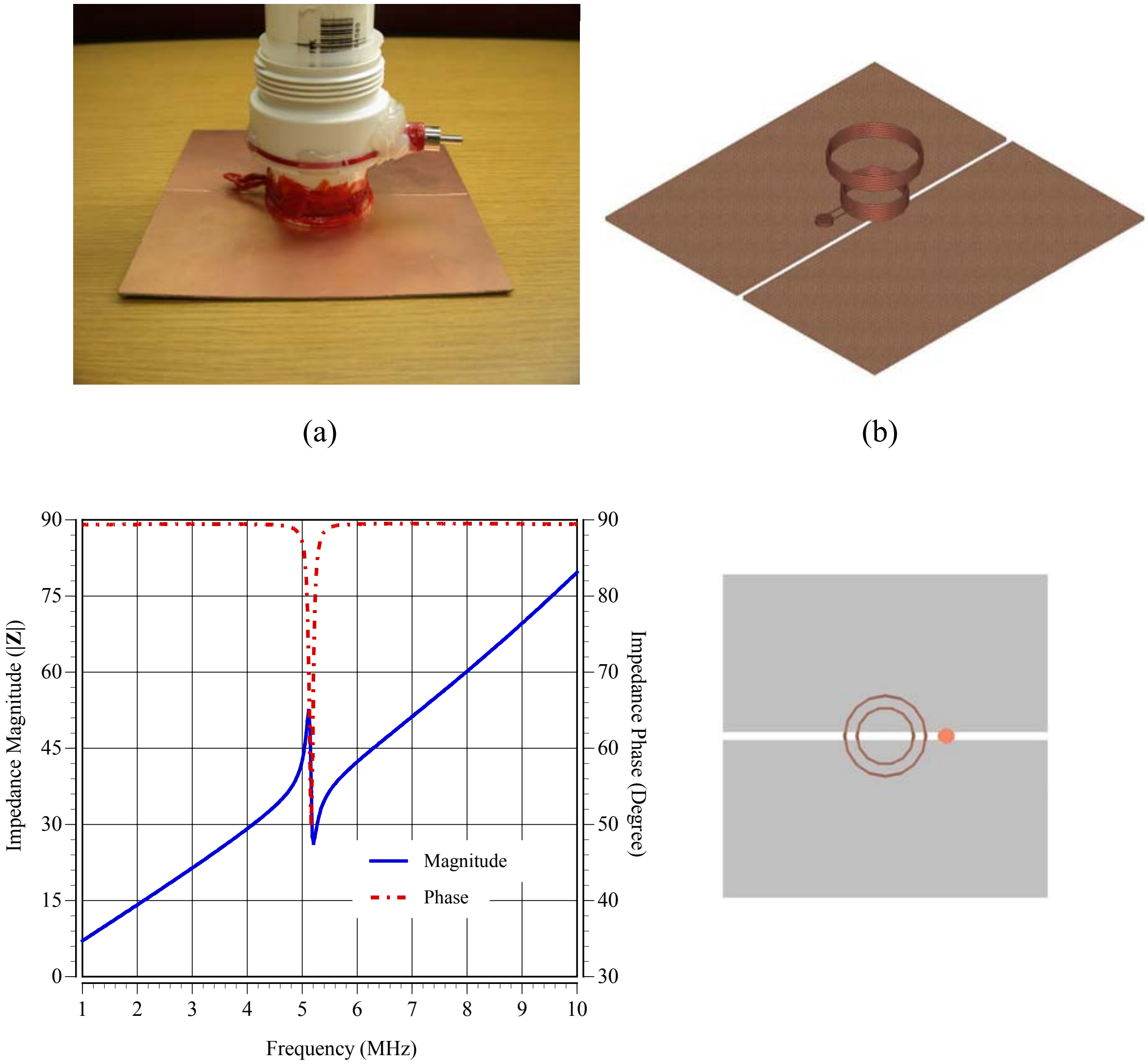

(a) (b)

(c) (d)

Figure 2.6: (a) The experiment for the impedance measurement (b) Illustration of experimental setup: a coil is located 3cm above copper plate which has slit in it and a passive repeater is 2.7cm apart from driver (c) The impedance taken when proposed series RLC resonance repeater was inserted between the driver and copper plate board with slit. (d) Top-down view of experimental setup.

Chapter 3

Inductance and Image Theory

As noted in the preliminary experiments, the crucial idea behind the proposed scheme is to use the change of inductance of a repeater by the influence of the eddy current induced on the conductive medium. That means since the repeater is also magnetically coupled to the driver, the inductive change introduced into the repeater will result in the modification of total inductance looking into the driver in the previous chapter.

As the inductance plays a central role in analyzing experimental results and finding equivalent circuits, this chapter presents a through review of inductance and mutual inductance under quasi-static field assumption along with application of the rigorous definitions to practical aspect of calculations.

3.1 SELF AND MUTUAL INDUCTANCE IN THEORY

3.1.1 Summary of an Electromagnetic Result[22]

For the following discussion on inductance, the form utilizing the scalar potential and the magnetic vector potential is particularly useful. Under the assumption that the differential form of Maxwell's equations holds and that the material are uniform, then

$$\overline{B} = \nabla \times \overline{A} \tag{3.1}$$

$$\overline{E} = -\nabla \Phi - \frac{\partial \overline{A}}{\partial t} \tag{3.2}$$

where $\overline{A}$ is the magnetic vector potential, $\overline{B}$ is the magnetic flux density, Φ is the electric scalar potential, and $\overline{E}$ is the electric field intensity. The equations for $\overline{A}$ and

Φ, which are given by for quasi-static conditions which is appropriate for circuit analyses.

$$\overline{A}(\overline{r}) = \frac{\mu}{4\pi}\iiint_V \frac{\overline{J}(r')}{\left|\overline{r}-\overline{r'}\right|}dV' \tag{3.3}$$

and

$$\overline{\Phi}(\overline{r}) = \frac{1}{4\pi\varepsilon}\iiint_V \frac{\rho_v(r')}{\left|\overline{r}-\overline{r'}\right|}dV',$$

where $\overline{J}$ is the current density and ρ_v is the volume charge density.

Voltages and currents are used for circuit modeling and simulation. Voltage is defined by

$$v = -\int \overline{E}\bullet\overline{dl}\,, \tag{3.4}$$

and current by

$$i = \iint_S \overline{J}(\overline{r})\bullet\overline{ds}\,.$$

While the computed voltage depends on the path chosen for the path integral at high frequency, voltage can be computed as a unique value for quasi-static field. In contrast, current is uniquely defined by the area, and its calculation is unambiguous at all frequencies.

3.1. 2 Definitions of (Self) Inductance

The definition of inductance can be rigorously based on the Maxwell's equations in general form, and successful application of the inductance concept relies on careful and strict interpretation of the meaning of closed line integrals and surface integrals.

Faraday's law in integral form is

$$\oint_C \overline{E}\bullet\overline{dl} = -\frac{d}{dt}\iint_S \overline{B}\bullet\overline{ds}\,, \tag{3.5}$$

where $\oint_C \overline{E} \bullet \overline{dl}$ sums the tangential component of the electric field around closed path given by contour C, and $\iint_S \overline{B} \bullet \overline{ds}$ sums the normal component of the magnetic flux density through the area enclosed by C. These relationships are sketched in Figure 3.1.

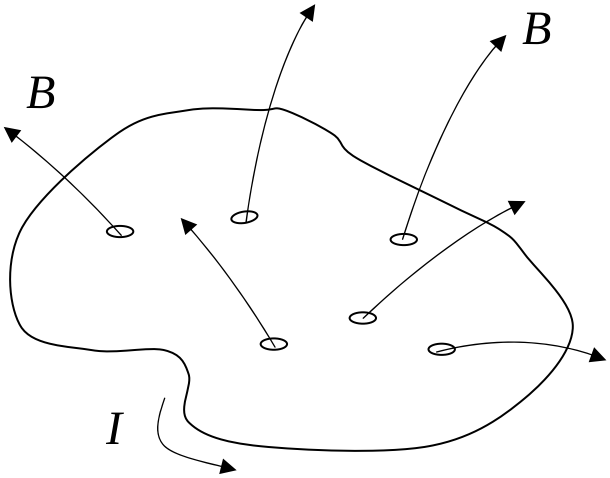

Figure 3.1: Contour and area sketch for interpretation of the integral relationship in Faraday's law[28].

Substituting (3.1) into (3.5) and applying Stokes' theorem,

$$\iint_S \left(\nabla \times \overline{A}\right) \bullet \overline{ds} = \oint_C \overline{A} \bullet \overline{dl}, \tag{3.6}$$

true for any vector field $\overline{A}$, yields

$$\oint_C \overline{E} \bullet \overline{dl} = -\frac{d}{dt} \oint_C \overline{A} \bullet \overline{dl}. \tag{3.7}$$

Under quasi-static conditions, substituting (3.3) to eliminate $\overline{A}$ gives

$$\oint_C \overline{E} \bullet \overline{dl} = -\frac{d}{dt} \oint_C \left(\frac{\mu}{4\pi} \iiint_V \frac{\overline{J}(r')}{\left|\overline{r} - \overline{r'}\right|} dV' \right) \bullet \overline{dl}. \tag{3.8}$$

For a circuit consisting of thin wire and small components, the current density vanishes for point off the contour, C, and it travels in a direction tangential to the contour. Executing the volume integral yields the simplified form

$$\oint_C \overline{E} \bullet \overline{dl} = -\frac{d}{dt} \oint_C \left(\frac{\mu}{4\pi} \oint_{C'} \frac{\bar{i}(r')}{\left|\overline{r} - \overline{r'}\right|} \overline{dl'} \right) \bullet \overline{dl} , \tag{3.9}$$

where i is the current on the thin wire. According to the quasi-static assumption, the current is constant on the contour, and (3.9) can be rearranged into time-constant and time-varying parts as

$$\oint_C \overline{E} \bullet \overline{dl} = -\oint_C \left(\frac{\mu}{4\pi} \oint_{C'} \frac{1}{\left|\overline{r} - \overline{r'}\right|} \overline{dl'} \right) \bullet \overline{dl} \frac{di}{dt} . \tag{3.10}$$

The complexity of Maxwell's equations is then capture in a time-constant, geometrically-dependant factor called inductance, defined by

$$L = \frac{\mu}{4\pi} \int_C \int_{C'} \frac{\overline{dl} \bullet \overline{dl'}}{\left|\overline{r} - \overline{r'}\right|} . \tag{3.11}$$

The left side of (3.10) can be cast using definition of voltages in (3.4) Incorporating (3.4) and (3.5) into (3.3) provides the classical voltage-current relationship for inductance as

$$v = L \frac{di}{dt} , \tag{3.12}$$

where v represents the voltage around a closed loop. So a time-varying current produces a voltage on the closed loop, where the value is given by the time derivative of the current scaled by the inductance.

Equation (3.12) is valid in general, even though the formula for L in (3.11) is valid only for thin wire. To obtain a more general formula valid for all cases, the use of field quantities is required. The right-hand side of (3.12) can be equated to the right-hand side of Faraday's law in (3.5) to obtain

$$L\frac{di}{dt}=\frac{d}{dt}\iint_S \overline{B}\bullet\overline{ds}\,. \tag{3.13}$$

Integrating (3.13) with respect to time, and noting that the integration constant vanishes since fields do not exist without current in the circuit. Then

$$L=\frac{\iint_S \overline{B}\bullet\overline{ds}}{i}\,. \tag{3.14}$$

In terms of field quantities, inductance is given by the total flux passing through a surface divided by the current magnitude in the circuit producing the magnetic flux.

A related field-based definition using the magnetic vector potential can be found by substituting (3.1) into (3.14) and then (3.6) to obtain

$$L=\frac{\oint_C \overline{A}\bullet\overline{dl}}{i}\,. \tag{3.15}$$

However, the reliance on the appropriate construction and application of a surface and the related surface integral can lead to difficulties in problem setup for (3.14). Through the use of energy relationships, a field-based inductance formulation involving only volume integrals is possible. From circuit theory, the energy stored in an inductor is

$\mathrm{E}=\frac{1}{2}Li^2$, (3.16)

While the result from electromagnetic field theory is

$$\mathrm{E}=\frac{1}{2}\iiint_V \overline{B}\bullet\overline{H}dV\,, \tag{3.17}$$

Where $\overline{H}$ is the magnetic field intensity, Equating these two definitions and solving for L yields

$$L=\frac{1}{i^2}\iiint_V \overline{B}\bullet\overline{H}dV\,, \tag{3.18}$$

Because of the relative simplicity of setup, (3.18) is often used to compute inductance in general-purpose electromagnetic simulators, where the computation of the field over a volume is straightforward but manipulation of surface definition is not.

3.1.3 Definition of mutual inductance

It is necessary to investigate the voltage induced on one circuit by the time-varying magnetic flux densities produced by another. The derivation and concept developed in previous section for inductance are extended in this section to investigate mutual inductance.

Consider a system consisting of two closed contour that are in close proximity so that the magnetic flux from one contour penetrates the area enclosed by the other. This system is sketched in Fig. 3.#. The total magnetic density is the sum of that produced by each circuit. So $\overline{B_t} = \overline{B_1} + \overline{B_2}$. Faraday's law applied to C_2 is

$$\oint_{C_2} \overline{E} \bullet \overline{dl} = -\frac{d}{dt} \iint_{S_2} \overline{B_1} \bullet \overline{ds} - \frac{d}{dt} \iint_{S_2} \overline{B_2} \bullet \overline{ds} . \tag{3.19}$$

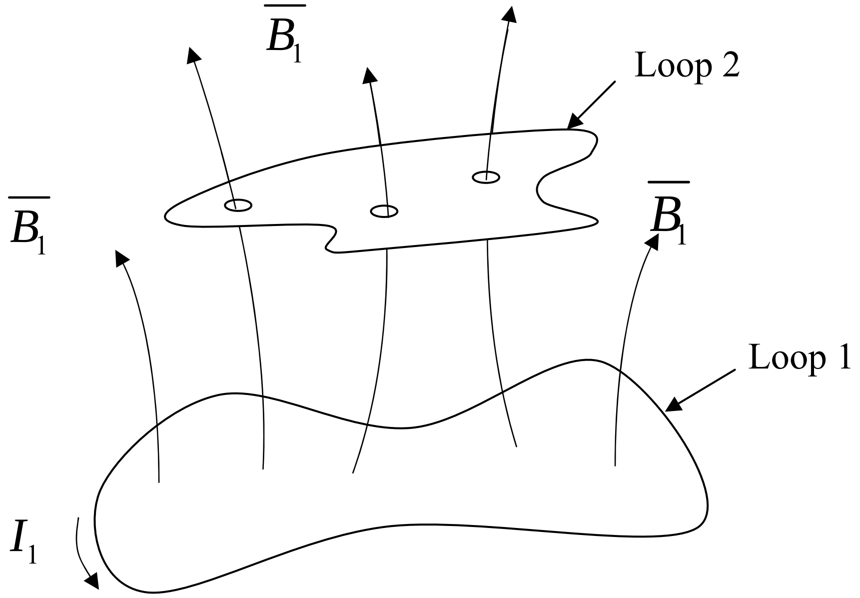

Figure 3.2: Contour and area sketch for interpretation of the integral relationship in Faraday's law for the case of mutual inductance [28].

Substituting (3.1) and applying Stokes' theorem from (3.6) yields

$$\oint_{C_2} \overline{E}\bullet\overline{dl} = -\frac{d}{dt}\oint_{C_2} \overline{A_1}\bullet\overline{dl} - \frac{d}{dt}\oint_{C_2} \overline{A_2}\bullet\overline{dl}\,. \tag{3.20}$$

Replacing the magnetic vector potential from (3.3) gives

$$\begin{aligned}\oint_{C_2} \overline{E}\bullet\overline{dl} = &-\frac{d}{dt}\oint_{C_2}\left(\frac{\mu}{4\pi}\iiint_V \frac{\overline{J_1}(r')}{\left|\overline{r}-\overline{r'}\right|}dV'\right)\bullet\overline{dl}\\ &-\frac{d}{dt}\oint_{C_2}\left(\frac{\mu}{4\pi}\iiint_V \frac{\overline{J_2}(r')}{\left|\overline{r}-\overline{r'}\right|}dV'\right)\bullet\overline{dl}\,.\end{aligned} \tag{3.21}$$

For quasi-static operation with thin wires and small components, the current densities vanish off the contour, and since the current travels in the same direction as the contour, then

$$\begin{aligned}\oint_{C_2} \overline{E}\bullet\overline{dl} = &-\frac{d}{dt}\oint_{C_2}\left(\frac{\mu}{4\pi}\oint_{C_2} \frac{\overline{i_1}(r')}{\left|\overline{r}-\overline{r'}\right|}\overline{dl'}\right)\bullet\overline{dl}\\ &-\frac{d}{dt}\oint_{C_2}\left(\frac{\mu}{4\pi}\oint_{C_2} \frac{\overline{i_2}(r')}{\left|\overline{r}-\overline{r'}\right|}\overline{dl'}\right)\bullet\overline{dl}\,.\end{aligned} \tag{3.22}$$

The current i_1 and i_2 are constant on the contours according to the quasi-static assumption, so (3.22) can be rearranged into time-constant and time-varying parts as

$$\oint_{C_2} \overline{E}\bullet\overline{dl} = -M_{12}\frac{di_1}{dt} - L_2\frac{di_2}{dt}\,, \tag{3.23}$$

where

$$M_{12} = \frac{\mu}{4\pi}\int_{C_2}\int_{C_1}\frac{\overline{dl'}\bullet\overline{dl}}{\left|\overline{r}-\overline{r'}\right|} \tag{3.34}$$

is the mutual inductance between contour C_1 and C_2 and is Neumann's formula for mutual inductance, and

$$L_2 = \frac{\mu}{4\pi}\int_{C_2}\int_{C_2}\frac{\overline{dl'}\bullet\overline{dl}}{\left|\overline{r}-\overline{r'}\right|} \tag{3.35}$$

is self-inductance for contour C_2. Note that the only difference between self- and mutual inductance is in the contours of integration: for self-inductance, integration is over the same contour while for mutual inductance, integration is over both contours.

Applying the definition of voltage from (3.4) to (3.23) provides a result completely in circuit quantities as

$$v_2 = M\frac{di_1}{dt} + L_2\frac{di_2}{dt}, \tag{3.36}$$

where v_2 is the voltage on the closed contour, C_2. Note that if the role of the contour C_1 and C_2 are reversed, then the formula for the mutual inductance in (3.34) remains unchanged.

$$M = M_{12} = \frac{\mu}{4\pi}\int_{C_2}\int_{C_1}\frac{\overline{dl'}\bullet\overline{dl}}{\left|\overline{r}-\overline{r'}\right|} = \frac{\mu}{4\pi}\int_{C_1}\int_{C_2}\frac{\overline{dl}\bullet\overline{dl'}}{\left|\overline{r}-\overline{r'}\right|} = M_{21}. \tag{3.37}$$

Therefore, inductance is reciprocal.

As done for definition of (self) inductance, more general formula for inductance can be found by equating the right-hand side of (3.36) to the negative of the right-hand side of (3.19) to obtain

$$M\frac{di_1}{dt} + L_2\frac{di_2}{dt} = \frac{d}{dt}\iint_{S_2}\overline{B_1}\bullet\overline{ds} + \frac{d}{dt}\iint_{S_2}\overline{B_2}\bullet\overline{ds}. \tag{3.38}$$

Integrating with a zero constant of integration yields

$$Mi_1 + L_2 i_2 = \iint_{S_2}\overline{B_1}\bullet\overline{ds} + \iint_{S_2}\overline{B_2}\bullet\overline{ds}. \tag{3.39}$$

from which it is apparent that

$$M = \frac{1}{i_1}\iint_{S_2}\overline{B_1}\bullet\overline{ds}. \tag{3.40}$$

Mutual inductance is given by the flux generated by the current in loop 1 that is coupled into loop 2, then normalized by the current in loop 1. In other word, it is the flux linked into loop 2 that is the root cause of mutual inductance.

Energy-based mutual inductance formula can be also derived as

$$\begin{aligned}M_{12} &= M_{21} \\ &= \frac{1}{i_1 i_2}\iiint_V \overline{B_1}\bullet\overline{H_2}\,dV \\ &= \frac{1}{i_1 i_2}\iiint_V \overline{B_2}\bullet\overline{H_1}\,dV .\end{aligned} \tag{3.41}$$

The subscript on the field quantities $\overline{B}$ and $\overline{H}$ imply the use of superposition. If both loops are simultaneously driven with current, then just one set of $\overline{B}$ and $\overline{H}$ exist. Using superposition, loop 1 is driven to produce $\overline{B_1}$ and $\overline{H_1}$ while the source on loop 2 is open-circuited ($i_2 = 0$). These fields are stored and the process is repeated with $i_1 = 0$ to obtain $\overline{B_2}$ and $\overline{H_2}$. These two solutions, picking either $\overline{B_1}$ and $\overline{H_2}$ or $\overline{B_2}$ and $\overline{H_1}$, are used in (3.41) to find the mutual inductance. Note that $\overline{B_1}$ and $\overline{H_1}$ alone determine the inductance of loop according to (3.11), while $\overline{B_2}$ and $\overline{H_2}$ determine the inductance of loop 2.

3.1.4 Calculation of inductance with Neumann's Formula

While Neumann's formula is an excellent means to discuss inductance, its direct application to calculation has limitations. For a filamental loop, $|r - r'|$ in (3.11) becomes zero when both loops traverse the same point. Thus, the integral is not defined for a filamental loop. The source of this difficulty is that the contour has zero cross-sectional area in contrast to real wire. However, it is possible to take care of finite wire radius through a mutual inductance calculation.

It is common to split the flux in a loop into two components to incorporate finite wire radius. One component defined as internal inductance is owing to the magnetic flux crossing internal portion of conductor volume. The other, external inductance, is due to magnetic flux outside conductor volume but still passing through the closed contour. The inductance is the sum of these two components.

The inductors are built by winding copper wire many times around a cylinder for the preliminary experiment in the previous chapter. By computing the inductance of those inductors using the theory described, it can be shown how the theory can be applied to real inductor. However, a single turn circular coil will be used to make things simple as seen in Figure 3.3. A bird's eye view of this loop is shown along with two thin wires located at the center of the finite radius wire ($C^{'}$) and along with the inner edge (C). The important observation is that the external inductance of the finite radius wire is determined by the flux inside C, while the mutual inductance between loop $C^{'}$ and C is also determined by this flux. Therefore, the external inductance of the thick wire can be computed as the mutual inductance between the thin wires. Neumann's formula for self-inductance is avoided. Note that the calculation is not complete until the internal inductance is added.

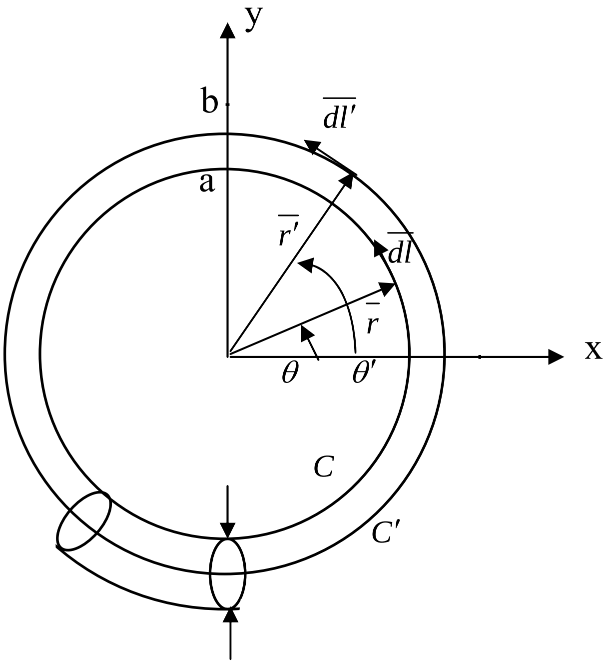

Figure 3.3: Concentric closed contours for computing external inductance using Neumann’s formula for mutual inductance[29].

To find the external inductance of the loop through the calculation of the mutual inductance between loop C' and C in Figure 3.3, let

$$\overline{r'} = b\cos\theta'\hat{x} + b\sin\theta'\hat{y}$$
$$\overline{r} = a\cos\theta\hat{x} + a\sin\theta\hat{y}$$
$$\overline{dl'} = b\,d\theta'(-\sin\theta'\hat{x} + \cos\theta'\hat{y})$$
$$\overline{dl} = a\,d\theta(-\sin\theta\hat{x} + \cos\theta\hat{y}) \tag{3.42}$$

then

$$\begin{aligned} \left|\overline{r} - \overline{r'}\right| &= \left|(a\cos\theta - b\cos\theta')\hat{x} + (a\sin\theta - b\sin\theta')\hat{y}\right| \\ &= \sqrt{a^2 + b^2 - 2ab(\cos\theta\cos\theta' + \sin\theta\sin\theta')} \\ &= \sqrt{a^2 + b^2 - 2ab\cos\left(\theta - \theta'\right)} \end{aligned}$$
$$\overline{dl'}\bullet\overline{dl} = ab\cos(\theta - \theta')\,d\theta'\,d\theta\,. \tag{3.43}$$

Filling out Neumann's formula for mutual inductance in (3.34), then

$$\begin{aligned} M &= \frac{\mu}{4\pi}\int_0^{2\pi}\int_0^{2\pi} \frac{ab\cos\left(\theta - \theta'\right)}{\sqrt{a^2 + b^2 - 2ab\cos\left(\theta - \theta'\right)}}\,d\theta\,d\theta' \\ &= 2\mu b\left[K\left(\frac{a}{b}\right) - E\left(\frac{a}{b}\right)\right], \end{aligned} \tag{3.44}$$

where K and E are the complete elliptic functions of the first and second kind respectively.

For thin wire, $a/b \simeq 1$, K and E can be approximated as

$$K\left(\frac{a}{b}\right) \simeq \ln\left(\frac{4}{\sqrt{1 - \left(\frac{a}{b}\right)^2}}\right) = \ln\left(\frac{4}{\sqrt{\frac{2r}{b} - \left(\frac{r}{b}\right)^2}}\right) \simeq \ln\left(\frac{4}{\sqrt{\frac{2r}{b}}}\right) \tag{3.45}$$

and

$$E\left(\frac{a}{b}\right) \simeq 1, \tag{3.46}$$

where r is the wire radius which is defined as $r = b - a$.

Thus, a simplified formula for the external inductance of the round loop of a finite radius real wire is

$$L_{\text{external}} = M = \mu b\left[\ln\left(\frac{8b}{r}\right) - 2\right]. \tag{3.47}$$

For internal inductance calculation, the thin-wire approximation does not apply, so Neumann's formula is inappropriate. Inductance must be computed with a field-based formulation such as (3.18). In Figure 3.4, a circular cross section of real wire with finite radius is shown, with a current I assumed to be uniformly distributed over the area. This assumption is valid only at low frequencies, since skin effect at high frequencies forces the current to be concentrated at the outer surface. With the conductor of radius a, Ampere's law gives

$$\overline{H} = \frac{Ir}{2\pi a^2}\hat{\phi} \ \text{ and } \ \overline{B} = \frac{\mu Ir}{2\pi a^2}\hat{\phi}. \tag{3.48}$$

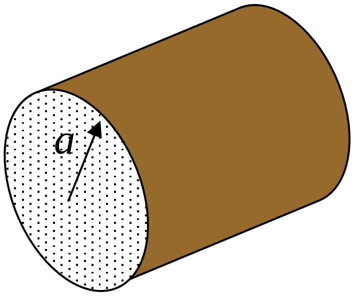

Figure 3.4: A circular cross section of finite radius real wire with a current I assumed to be uniformly distributed over the area.

The straight piece of conductor shown in the Figure 3.4 must be imagined as a short section of an infinite length wire. Using the expression in (3.18) and integrating over the volume of the wire yields

$$L_{\text{internal}} = \frac{l}{i^2}\int_0^a \left(\frac{\mu I}{2\pi a^2} r\right)\left(\frac{I}{2\pi a^2} r\right) 2\pi r\, dr \ , \tag{3.49}$$

where integration over the length, l, and the angular variation are already included. Completing the computation yields

$$L_{\text{internal}} = \frac{\mu l}{8\pi i^2} \ , \tag{3.50}$$

which is the internal inductance of a round wire in isolation. Note that this result is independent of the radius of the wire; all round wire of a given length have the same internal inductance.

To conclude the computation of inductance for the circular loop of real wire with a finite radius, the external and internal inductance should be added together to provide the inductance of the loop. Adding (3.47) and (3.50) with $l = 2\pi b$ gives

$$L = \mu b\left[\ln\left(\frac{8b}{r}\right) - \frac{7}{4}\right]. \tag{3.51}$$

3.2 MEASURING THE INDUCTANCE

Up to this point, how the inductance of a round loop can be computed theoretically is explained. To complete the discussion on the inductance, it is necessary to compare the theoretically computed inductance with that from actual measurement. Thus, it is to be described in the next how to extract the inductance after a measurement using the instrument like an impedance analyzer.

The coil of which the inductance needs to be evaluated is connected to the impedance analyzer as seen in Figure 3.5. However, the measured value also contains the parasitic since the coil is connected to the measurement instrument via the cable and fixture. Thus, the calibration process is discussed in the next through which this parasitic can be removed from the measurement.

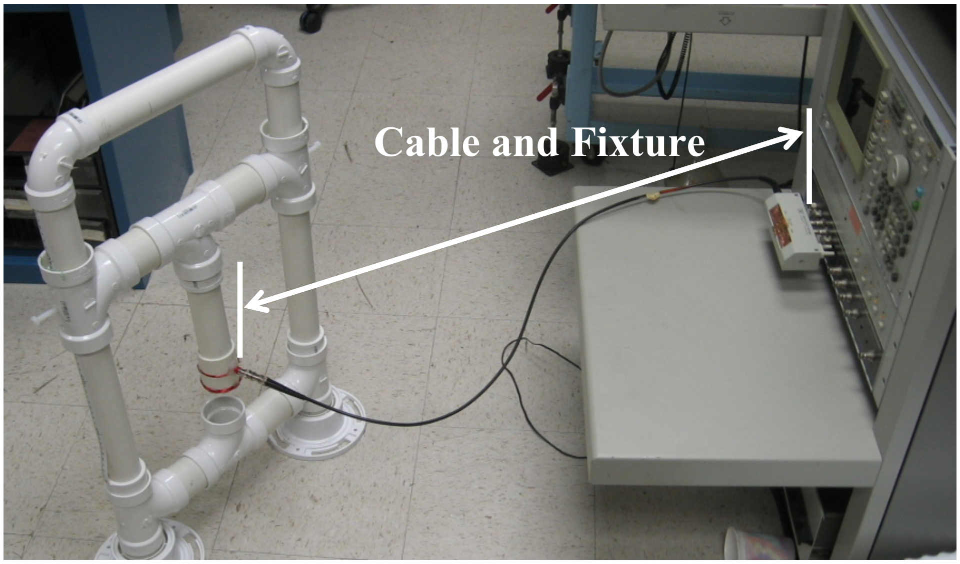

Figure 3.5: The coil is connected to the impedance analyzer via cable and fixture. However, the measured value also contains the parasitic of the since the coil is connected to the measurement instrument via the cable and fixture.

3.2.1 Calibration process to remove the parasitic

Parasitic elements are not concerns when measuring the impedance at low frequency so that a pair of wires is used to connect the measurement equipment to a device and it can be assumed without causing any problems that the reading reflects the impedance of the device under test (DUT). However, at high frequencies the influences of the parasitic elements have to be taken into account for the purpose of the accuracy of experiments. The typical circuit representation of the measurement arrangement is shown below in Figure 3.6.

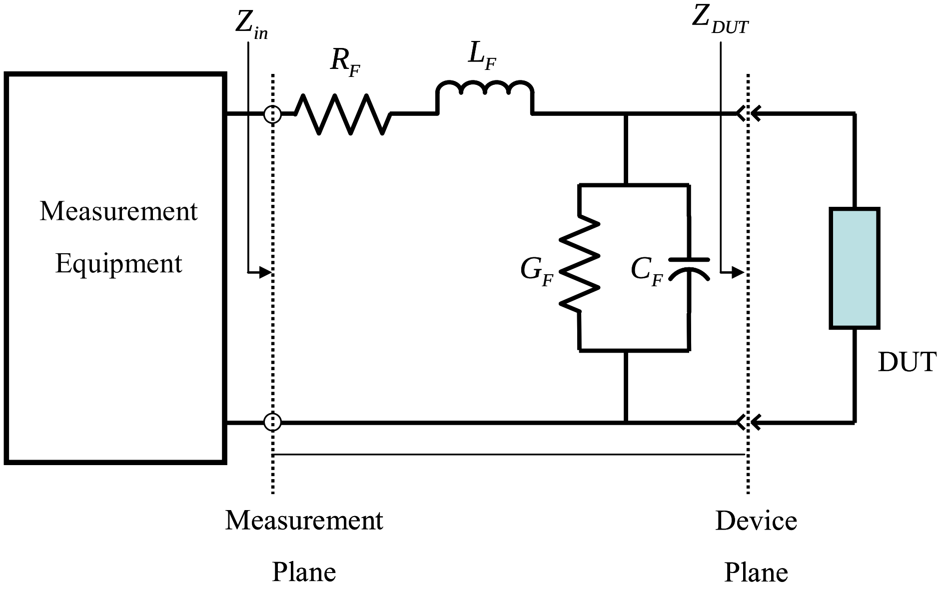

Figure 3.6: The typical circuit representation of the measurement arrangement.

Here the fixture and cables are replaced by an equivalent circuit of the lead impedance ($Z_F = R_F + j\omega L_F$) and stray admittance ($Y_F = G_F + j\omega C_F$). Ideally, the measurement should be performed at the device plane. Nevertheless, due to the influence of the fixture, the measurement plane is shifted away from DUT.

To accurately measure the impedance of the DUT, the test fixture with connecting cables has to be taken into consideration. A way to nullify those consequences of test fixtures plus cablings is to compensate for undesirable, fixture-related influences through an open- and short-circuit calibration, which is the methodology adopted by the most manufactures. The procedure with all necessary equations will be explained as follows. The first step is to replace the DUT by a short circuit and measure the resulting impedance as shown in Figure 3.7a. As a result of the parasitic due to fixtures and cables, the recorded impedance ($Z_{mea,s}$) is not equal to zero. However, a little reasoning leads to the conclusion that this measured impedance is approximately equal to the lead impedance ($Z_F = R_F + j\omega L_F$) of the fixture. This can be written in equation as follows.

$$Z_{mea,s} = Z_F \,. \tag{3.52}$$

Next, the short circuit is replaced by an open circuit as illustrated in Figure 3.7b and the impedance is recorded again. If the new impedance is assumed to be $Z_{mea,o}$, it is equal to the series combination of the lead impedance ($Z_F = R_F + j\omega L_F$) and "stray impedance", that is inverse of stray admittance ($Y_F = G_F + j\omega C_F$), because open circuit does not load the input to measurement equipment. Thus, the stray admittance can be found by the substitution of $Z_{mea,s}$ for Z_F as shown below.

$$Z_{mea,o} = Z_F + \frac{1}{Y_F}$$

$$Y_F = \frac{1}{Z_{mea,o} - Z_F} = \frac{1}{Z_{mea,o} - Z_{mea,s}} \,. \tag{3.53}$$

As a consequence, these two measurements allow us to quantify the parasitic influence of the fixture. After the calibration process described above, the DUT can be connected and the input impedance (Z_{in}) can be measured. The equivalent circuit representation is shown in Figure 3.6. Now it is straightforward to extract the impedance of the DUT (Z_{DUT}) from the measured input impedance (Z_{in}). The total impedance seen from measuring equipment into the DUT is the sum of parasitic fixture impedance (Z_F) and inverse of sum of two admittances, stray admittance (Y_F) and admittance of the DUT (Y_{DUT}). That is

$$Z_{in} = Z_F + \frac{1}{Y_F + Y_{DUT}} \,. \tag{3.54}$$

The equation (3.54) can be rearranged in terms of Y_{DUT} as below

$$Y_{DUT} = \frac{1}{Z_{in} - Z_F} - Y_F \,. \tag{3.55}$$

By substituting Z_F and Y_F with proper equivalences derived from calibration processes, it becomes

$$Z_{DUT} = Y_{DUT}^{-1} = \left[\frac{1}{Z_{in} - Z_{mea,o}} - \frac{1}{Z_{mea,o} - Z_{mea,s}} \right]^{-1} . \tag{3.56}$$

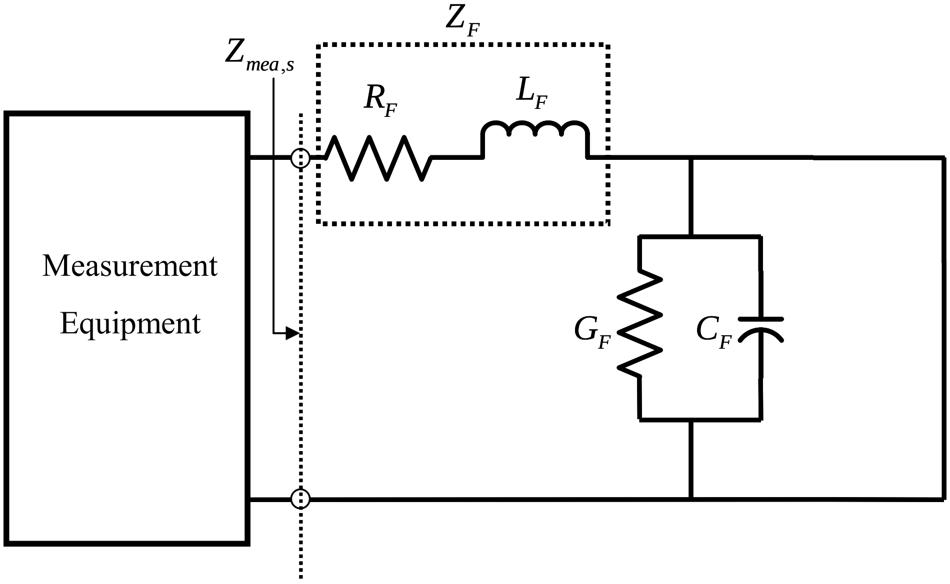

(a)

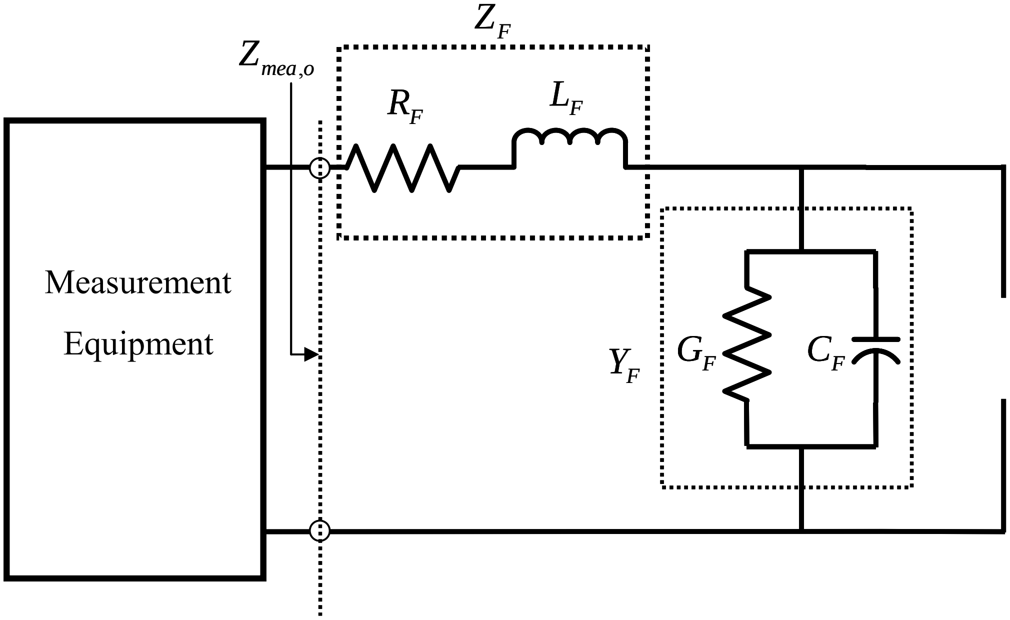

(b)

Figure 3.7: The circuit representation of the arrangement to compute the lead impedance and stray admittance. (a) The DUT replaced by a short circuit. (b) The DUT replaced by an open circuit.

3.2.2 Comparison between theory and measurement after a calibration

To remove the parasitic due to the fixture and cables, the calibration techniques was discussed in previous section. The calibration process is essential for the acquisition of the accurate value whenever the device under test is connected to measuring instrument via a fixture and a cable.

Since how the parasitic can be removed is now established, it is worthy to compare theory on the inductance with the actual measurement data using the calibration.

For the experiment, a single turn circular loop with a radius of 1.85cm is built with a round 19AWG (American Wire Gauge) copper wire which has the diameter of 0.91186mm. The theoretically evaluated inductance of the loop is 93.75nH using (3.51). The result is plotted in the Figure 3.8.

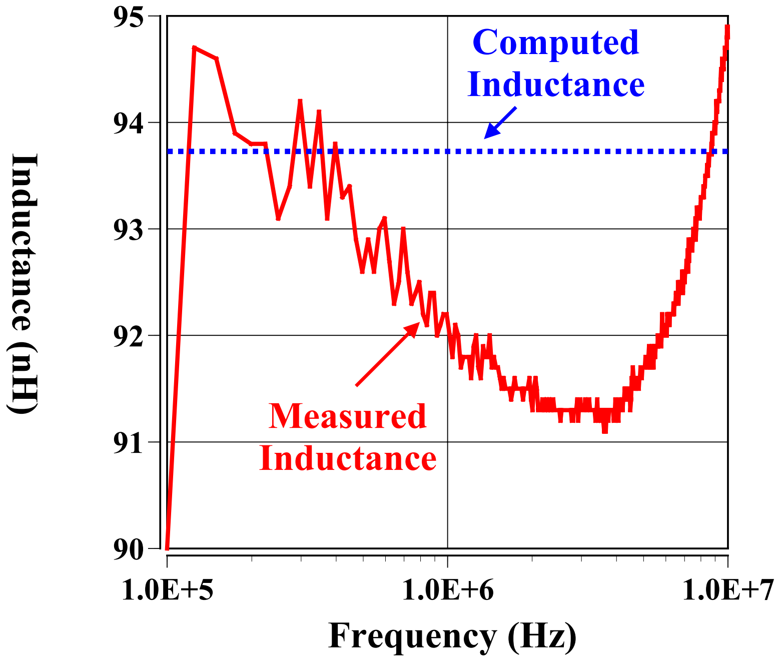

Figure 3.8: Comparison between theory on the inductance and the actual measurement data using the calibration. The measured inductance of a circular loop is plotted in solid line. From the theory, the inductance of the loop is 93.75nH.

As can be seen in Figure 3.8, the predicted value from the theory on the inductance is very close to the measured one after the calibration.

Although only the inductance of circular loop is computed and compared with the experimental data, the inductance of lumped elements can be predicted with reasonable accuracy [30-36].

3.3 IMAGE THOERY

The image principle gives a simple method to treat electromagnetic problems involving interfaces of materials media by replacing the structures behind the interface by an equivalent image sources in a homogeneous medium [37, 38]. Most probably the first definition of the image concept in electricity and magnetism was given by William Thomas (later Lord Kevin) in 1849 [39]:

> The term Electric Images, which will be applied to the imaginary electrical point or groups of electrical points, is suggested by the received language of Optics; and the closed analogy of optical images will, it is hoped, be considered as a sufficient justification for the introduction of a new and extremely convenient mode of expression into the Theory of Electricity.

Formulating an electromagnetic problem involving a physical structure in terms of an image source can be compared to working the Green function associated with the boundary-value problem. The image principle may well be the simpler choice because in many structures it can be expressed in closed form while the Green function cannot. Actually, the Green function can always be written in the form of an integral of the image source. Because the image source is a quasi-physical concept, physical intuition can help in the computation of fields. In fact, fields arise from image sources in the same way as they do from physical sources. Also, image sources can be approximated like the physical sources to simplify the computation, even if the image source might exist in complex space. Furthermore, image sources can take the role of unknown in integral equation.

3.3.1 Simple examples of image theory

As one of simple example, consider a point charge, q, at distance z' above a large, plane, conducting sheet, which may be effectively considered to be infinite in extent as in Figure 3.9. Since this sheet is grounded, its potential is zero.

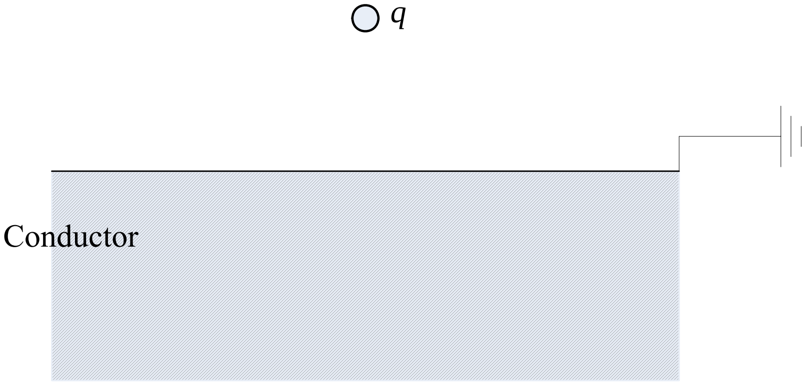

Figure 3.9: A point charge, q, at distance z' above a large, plane, conducting sheet which effectively considered infinite in extent.

Let's see how to find the potential and electric field in the space containing q using the method of image [40]. In the figure, this is region of space above ground plane. First, assume the origin is located just beneath the charge q, on the surface of the conductor. As a result, since there is clearly symmetry about the z axis, cylindrical coordinates are appropriate for this example. Next, the realization of a zero potential for the plane z=0 is simply achieved by adding to the potential due to q, a potential due to an imaginary image charge, -q, located a distance z' beneath plane z=0 as illustrated in

Figure 3.10. Consequently the potential and electric field for $z \geq 0$ is simply that due to two point charges q and $-q$ separated by a distance $2z'$. The potential may be written as

$$V(\mathbf{r}) = \frac{1}{4\pi\varepsilon_0} \cdot \left(\frac{q}{|\mathbf{r} - \hat{\mathbf{z}}z'|} + \frac{-q}{|\mathbf{r} + \hat{\mathbf{z}}z'|} \right) \qquad z \geq 0 \quad . \tag{3.57}$$

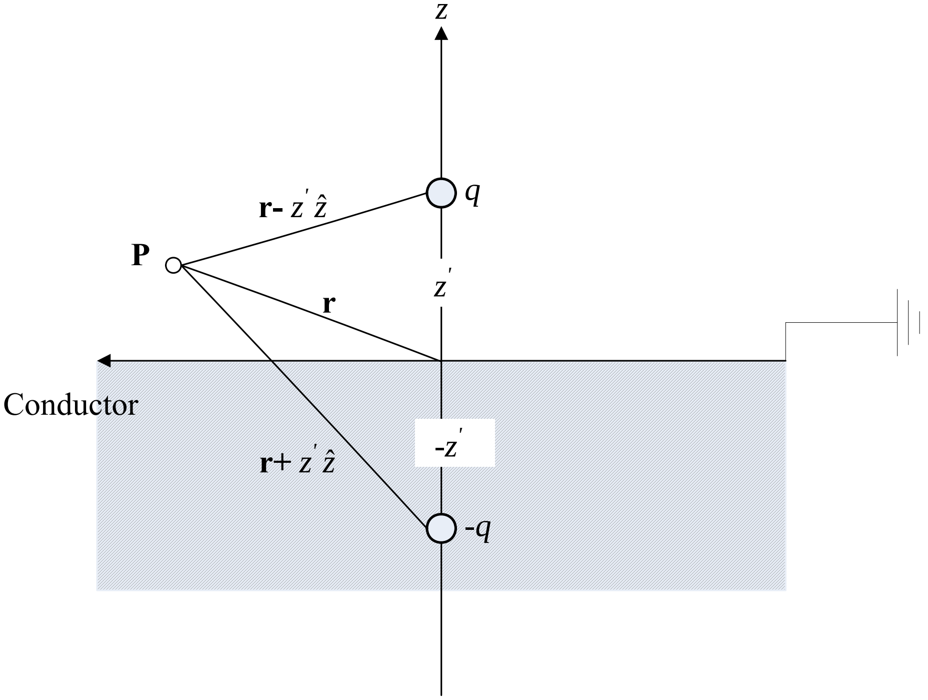

Figure 3.10: A point charge q near a large, grounded conducting plate. Also shown is an image charge -q whose field when added to that of the real one gives the correct field.

In cylindrical coordinates, $\mathbf{r} = \rho\hat{\boldsymbol{\rho}} + z\hat{\mathbf{z}}$ and $|\mathbf{r} \pm z'\hat{\mathbf{z}}|^2 = \rho^2 + (z \pm z')^2$ where $\hat{\boldsymbol{\rho}}, \hat{\mathbf{z}}$ are unit vectors. The electric field can be obtained from the expression $\mathbf{E}(\mathbf{r}) = -\nabla V(\mathbf{r})$ or, more directly, from Coulomb's law for two point charges

$$\mathbf{E}(\mathbf{r}) = \frac{1}{4\pi\varepsilon_0} \cdot \left(\frac{q(\mathbf{r} - \hat{\mathbf{z}}z')}{|\mathbf{r} - \hat{\mathbf{z}}z'|^3} + \frac{-q(\mathbf{r} + \hat{\mathbf{z}}z')}{|\mathbf{r} + \hat{\mathbf{z}}z'|^3} \right) \qquad z \geq 0 \quad . \tag{3.58}$$

On the ground surface for which $z = 0, \mathbf{r} = \rho\hat{\boldsymbol{\rho}}$, we get

$$\mathbf{E}(\rho) = \frac{q}{4\pi\varepsilon_0} \cdot \left(\frac{\rho\hat{\boldsymbol{\rho}} - z'\hat{\mathbf{z}}}{\left(\rho^2 + z'^2\right)^{3/2}} - \frac{\rho\hat{\boldsymbol{\rho}} + z'\hat{\mathbf{z}}}{\left(\rho^2 + z'^2\right)^{3/2}} \right) = \frac{q}{4\pi\varepsilon_0} \cdot \left(\frac{-2z'\hat{\mathbf{z}}}{\left(\rho^2 + z'^2\right)^{3/2}} \right) \quad . \quad (3.59)$$

From the above result, the actual surface charge density on the *z*=0 face of the conductor can be found by

$$\sigma = \varepsilon_0 \left(\mathbf{E} \cdot \hat{\mathbf{z}} \right)_{z=0} = \frac{-q}{2\pi} \frac{z'}{\left(\rho^2 + z'^2\right)^{3/2}} \quad . \quad (3.60)$$

The induced charge density, as expected, is negative. It has maximum value at $\rho = 0$, and falls off with the dependency of $1/\rho^3$ as ρ becomes large compared to z'. It is this induced charge plus the original charge located at z' that produces the actual solution, even though the solution was derived on the assumption of the original *q* and its “image charge”, -*q*, by utilizing the superposition principle. It is easy to verify that the total induced surface charge *Q* is equal to –*q*, implying that all the lines of force terminate on the conductor.

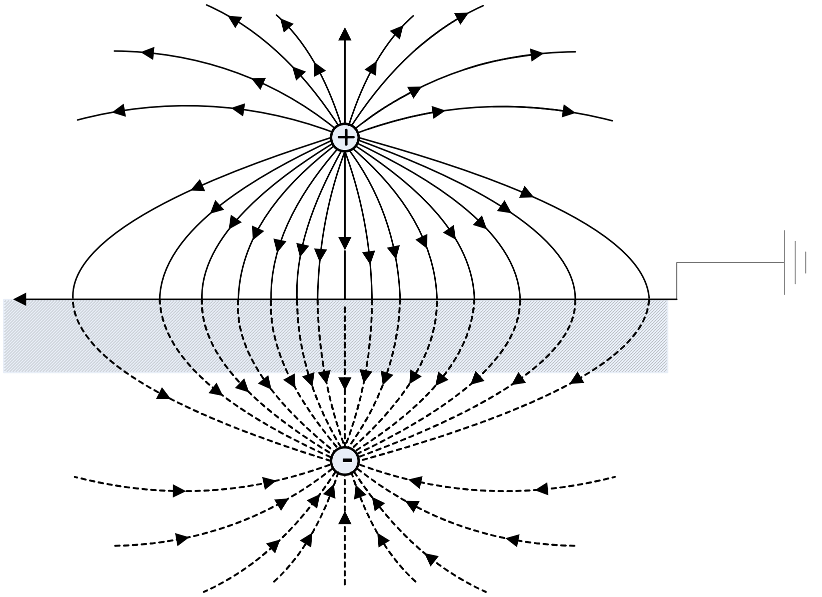

Figure 3.11: The lines of force between a point charge and a nearly grounded conducing plate.

In the previous example, the ground plane was a plane of symmetry on which the boundary condition that the tangential electric field was zero has to be satisfied. As a dual of above example, the requirement that the magnetic field intensity be tangential to the boundary can be satisfied by symmetrically mounting source distributions on both sides of the plane. Superposition of charge pairs of opposite sign, placed symmetrically on two sides of a plane, results in an electric field that is normal to the plane of symmetry; however, symmetrically mounting current sources leads to the zero normal magnetic flux conditions. The most obvious example is an infinitely long line current at z' from a perfectly conducting plane. The appropriate image is then an oppositely directed line current located at a distance z' to the other side of perfectly conducting plane. Next example, involving a three-dimensional field, is to show that the method of images is not confined to the two-dimensional situations. As shown in Figure 3.13, a current loop with time-varying current *i* is mounted a distance *h* above a perfectly conducting plane.

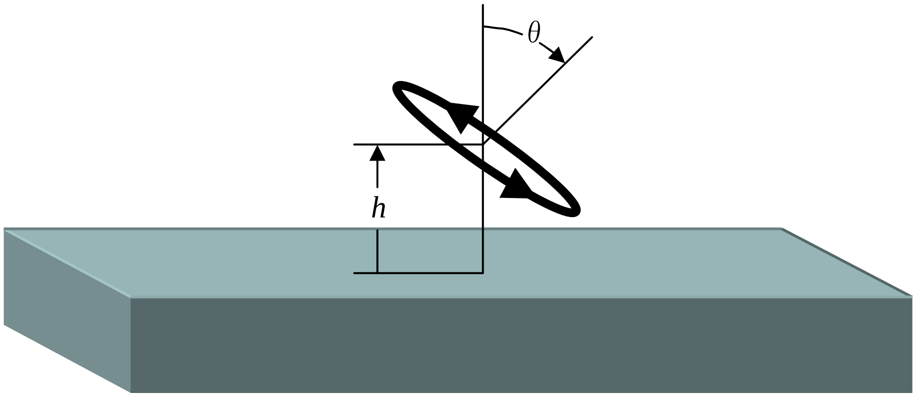

Figure 3.12: Current loop at distance *h* above a perfectly conducting plane.

An image loop should be mounted to satisfy the boundary condition in the plane of the perfectly conducting plane as shown in Figure. 3.13. For each current segment in the actual loop, there is a segment in the image loop giving rise to an oppositely directed vertical component of magnetic field intensity, **H.** Thus, the net normal flux density in the plane of the perfect conductor is zero.

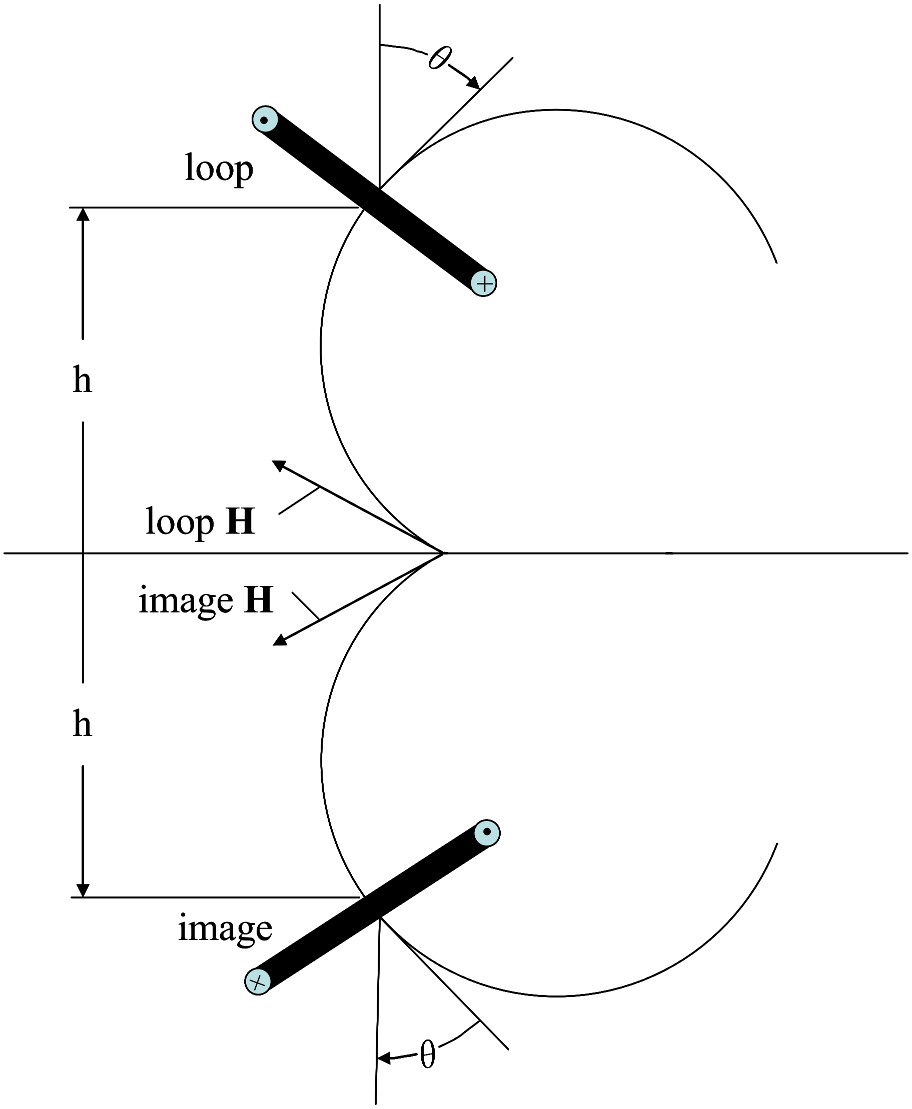

Figure 3.13: Cross-section of configuration of Figure 3.14, showing image dipole giving rise to field that cancels the flux density normal to the planar perfect conductor [41].

3.3.2 Experimental verification of image theory

In the previous section, it was illustrated through examples how the theory of image can be exploited to simplify the electrostatic or magnetostatic problems. The theory of image is a well-established principle; however, the experiments to prove the effectiveness of the theory in a non-ideal condition such as a ground plane of finite conductivity have been done in this section.

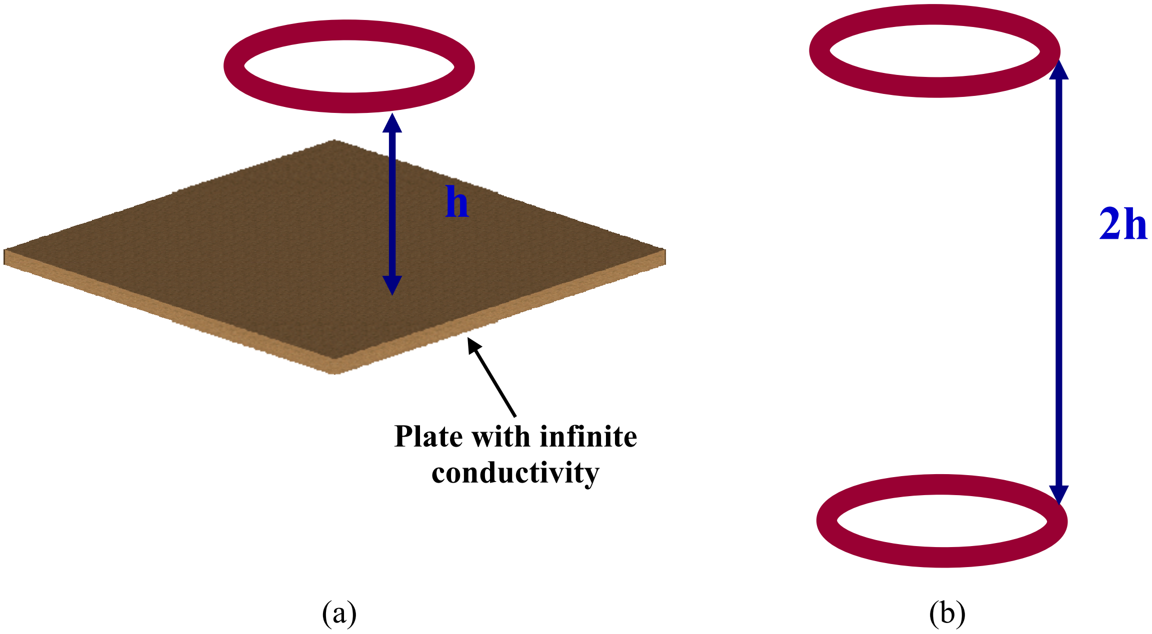

Figure 3.14: Application of image theory to a circular loop over a perfect conducting plate. (a) A circular loop through which the current flows is located above a conducting slab of finite thickness. (b) The perfect conducting plated is replaced by the image loop of the circular loop.

As noted earlier, the examples on the image theory was based on the assumption that the ground plane is a perfect conducting plane. To see if the theory of image is really useful in actual application, it is necessary to compare value from the experiment done in non-perfect condition and that from perfect image theory. A circular loop through which the current flows is located above a conducting slab of finite thickness as in Figure 3.14a. The material of the finite thickness plate with infinite conductivity is assumed to be placed under the current loop. The circular loop is located parallel to the dividing surface. By applying the image theory, the perfect conducting plated is replaced by the image loop of the circular loop as in Figure 3.14b. The circular loop is chosen because it can be easily built using copper wires and also has a very simple closed-form formula for the calculation of the inductance. The plate of infinite conductivity is replaced by a copper plate and a copper circular wire is used for the measurement.

The single turn circular loop that is used to test the theory on the inductance is used to experiment the image theory. The result is plotted in Figure 3.15. From the figure, the conclusion is that the actual measured data is consistent with the image theory.

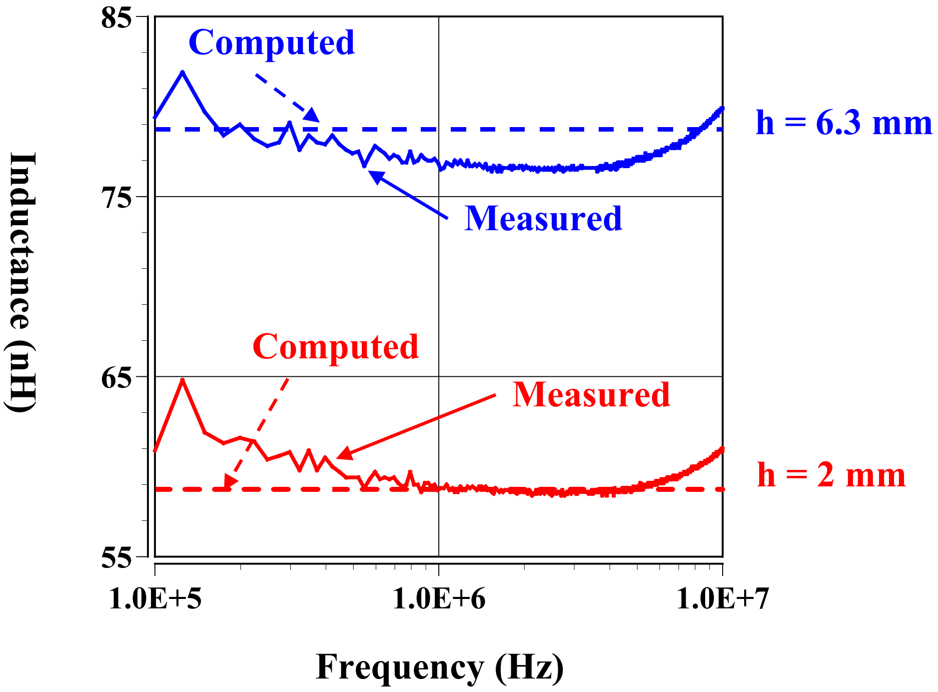

Figure 3.15: The result plot from the experiment illustrated in Figure 3.14a. The solid line represents data from actual measurement and dotted line does theoretical value computed by applying image theory.

Chapter 4

Equivalent Circuit Modeling

In the previous chapters, the result of preliminary experiment, which demonstrates the usefulness of our proposed scheme, was presented. In addition, the fundamental theory crucial to conducting this research was investigated in detail.

4.1 OVERVIEW OF EQUIVALENT CIRCUIT MODELING

Based upon the theory of self and mutual inductance and the image theory, it is possible to construct equivalent circuit model of the system. The system is meant to be such an entity that is responsible for the impedance response through the direct connection or magnetic coupling. For example, the system includes the driver coil, the repeater tag, and the copper plate (DUT) in Figure 4.1. However, the external surrounding is not part of the system. Thus, the objects that constitute the system are related to the impedance response through the localized interaction with the driver coil in the experiment setup treated so far.

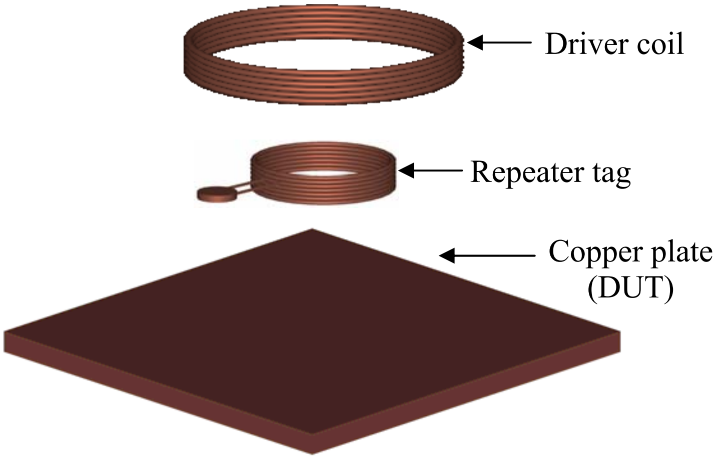

Figure 4.1: The system is meant to be such an entity that is responsible for the impedance response through the direct connection or magnetic coupling. The system includes the driver coil, the repeater tag, and the copper plate (DUT) for the setup above.

For the setup in Figure 4.1, a plausible equivalent circuit based solely on the image theory can be represented as given in Figure 4.2.

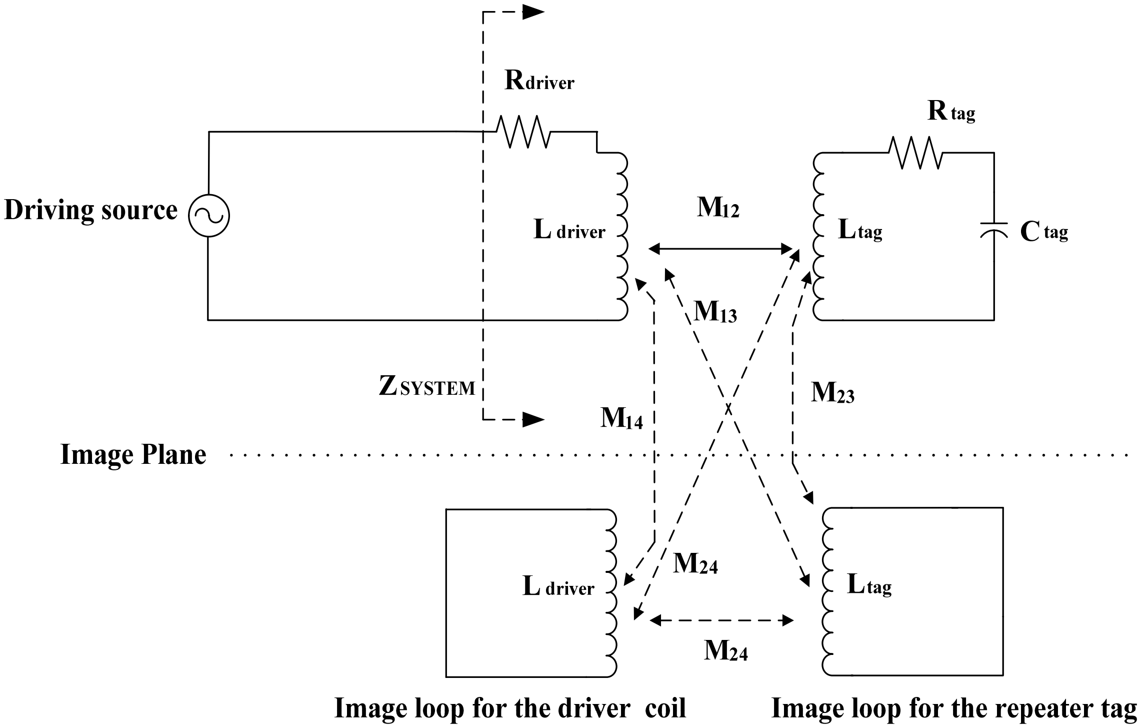

Figure 4.2: A plausible equivalent circuit representation of the setup in Figure 4.1.

In Figure 4.2, the inductances and resistances can be computed with the theory described earlier. However, since there is always the possibility of discrepancy between the theory and the actual measurement using an impedance analyzer, our approach will utilize a black box in each loop to remove the discrepancy. However, if an equivalent circuit with black box on every loop is to be built, it would be a daunting task to simultaneously find the values for each black box in Figure 4.1. Consequently, the equivalent circuit for the simplest system will be built first and then more complex one are to be done based on the simpler one which is constructed before.

4.2 BUILDING AN EQUIVALENT CIRCUIT MODEL

4.2.1 The system consisting of the driver coil

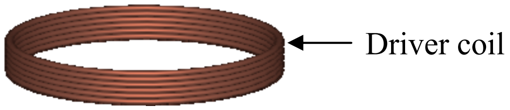

(a)

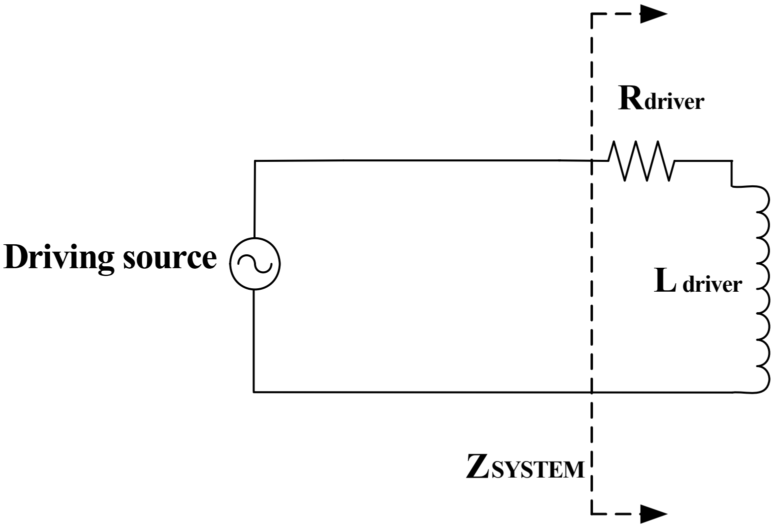

(b)

Figure 4.3: (a) The simplest system is one that consists only of driver coil. (b) The inductance and resistance are expected to capture correctly the system impedance response due to the driver coil.

The simplest system is one that consists only of driver coil as illustrated in Figure 4.3a. An equivalent circuit of the system can be constructed as given in Figure 4.3b since the inductance and resistance are expected to capture the system impedance response correctly due to the driver coil. The system impedance can be found by applying basic network theory to the loop. The result of the network theory can be expressed as [43]

$$Z_{system} = \frac{V_s}{I_{driver}} = R_{driver} + j\omega L_{driver}\,, \tag{4.1}$$

where V_s is the driving source voltage and I_{driver} is the current of the driver coil.

The resistance and inductance value are plotted in Figure 4.4. Those values are evaluated from actual measurement using calibration and will be used for building an equivalent circuit for more complex systems.

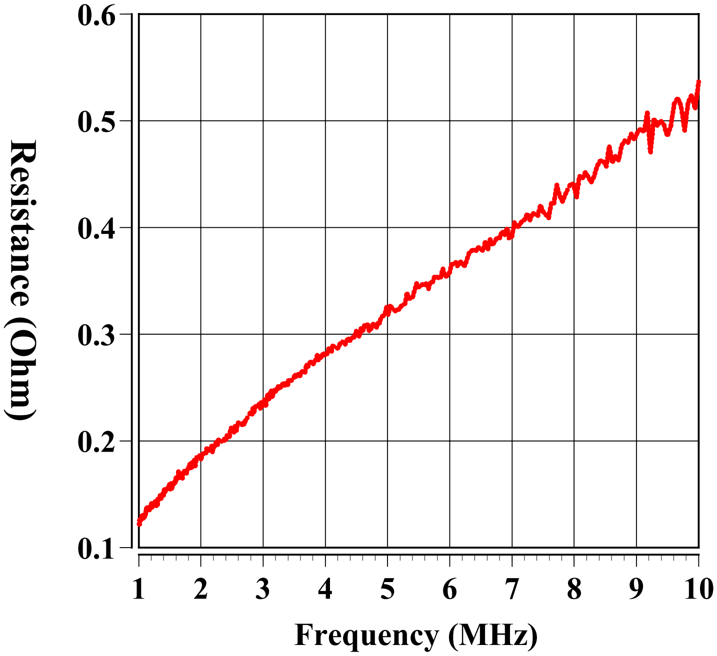

(a)

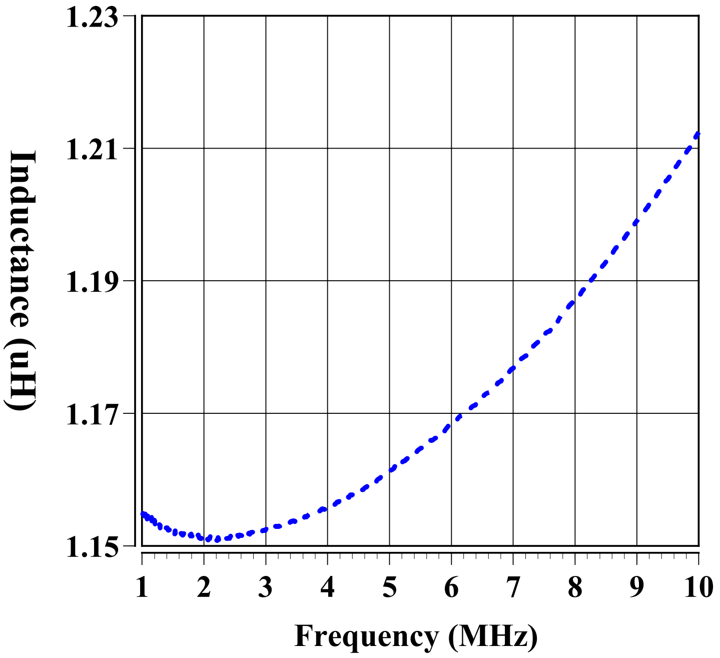

(b)

Figure 4.4: The values for the equivalent circuit representation in Figure 4.3b. (a) The resistance of the driver coil. (b) The inductance of the driver coil.

4.2.2 The system consisting of the driver coil and the repeater tag

Since the resistance and inductance of the driver coil have been determined, the next step is to build an equivalent circuit of the system when both the driver coil and the repeater tag are present in the system as Figure 4.5a. An equivalent circuit representation for the system is given in Figure 4.5b. Except for the Z_{tag}, all other circuit parameters, such as the resistances, the self and mutual inductances, and the capacitance in the equivalent circuit representation, are already known. The black box, Z_{tag}, is inserted to compensate for mismatch between the computed values and the actual measurement. The resistance and inductance of the driver coil have determined by the process explained in the previous section. Since the capacitance of the repeater tag is known and the system resonant frequency can be found from the measurement, the inductance of the repeater tag can be computed using (4.9) which is repeated here.

$$L_{eff} = \frac{1}{\left(2\pi f_{sys}\right)^2 C_{tag}}. \tag{4.2}$$

With a capacitor of 471pF and the resonant frequency at 4.57MHz, the inductance of the repeater tag is evaluated to be 2.57uH. The mutual inductance can be evaluated based on the geometrical information between the driver coil and the repeater tag. Thus, applying the network theory to the equivalent circuit leads to

$$\begin{bmatrix} R_{driver} + j\omega L_{driver} & j\omega M_{12} \\ j\omega M_{12} & R_{tag} + j\omega L_{tag} + \dfrac{1}{j\omega C_{tag}} + Z_{tag} \end{bmatrix} \begin{bmatrix} I_{driver} \\ I_{tag} \end{bmatrix} = \begin{bmatrix} V_s \\ 0 \end{bmatrix}. \tag{4.3}$$

By properly manipulating (4.3) and using the measurement data after calibration, the real and imaginary of Z_{tag} are found as in Figure 4.6. As expected, the values of Z_{tag} are small. The real part of the Z_{tag}, which has the characteristics of a resistance, is very small in magnitude and randomly varies in the frequency range of interest. From this observation, it can be assumed without a significant error that the real part is zero which compensates for the mismatches between the computation and the actual measurement. The imaginary part of the Z_{tag} varies within 0 and 40nH. Compared to the inductance of the repeater tag, the inductance is only about 1/500 of the repeater tag. Thus, it is acceptable not to take that parasitic inductance into account for the equivalent circuit modeling. Therefore, the values computed based only on the theory can be said to be reasonably good enough for building an equivalent circuit in Figure 4.5b.

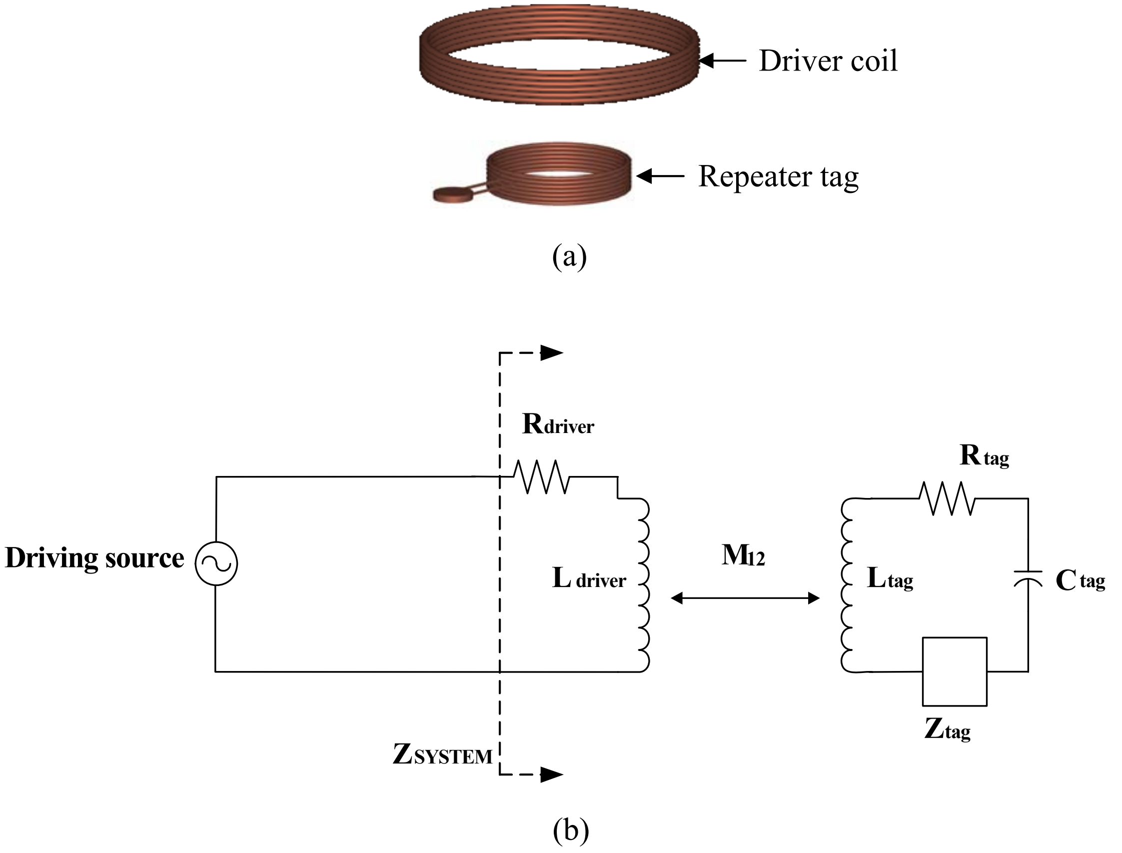

Figure 4.5: (a) The system consists of driver coil and the repeater tag. (b) An equivalent circuit representation for the system.

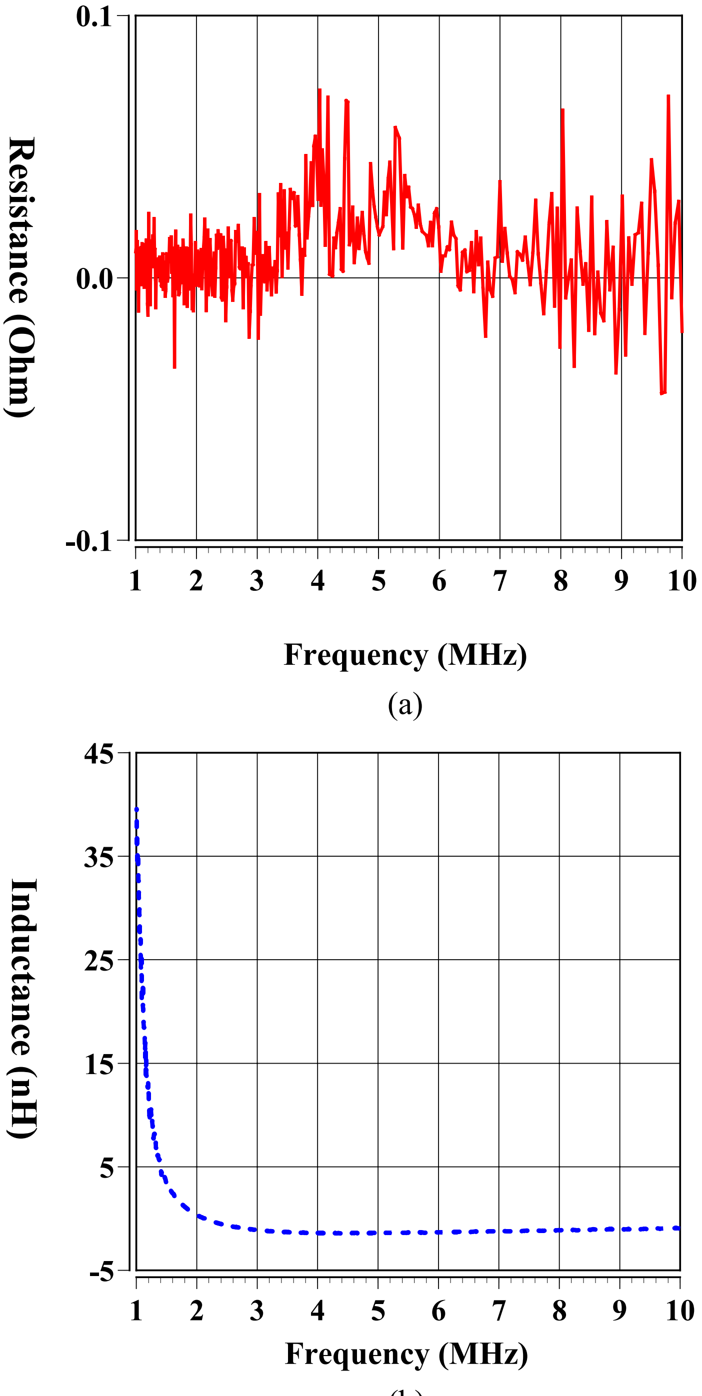

(a)

(b)

Figure 4.6: The values for the black box, Z_{tag} , in the equivalent circuit representation in Figure 4.5b. (a) The resistance of Z_{tag} . (b) The inductance of Z_{tag} .

4.2.3 The system consisting of the driver coil, the repeater tag, and the DUT

4.2.3.1 Various types of tag

Up to this point, only the repeater tag is used for the experiment and analysis. Based on the reasoning given in Chapter 1, the repeater tag is made by connecting a closely wound cylindrical coil to a capacitor in series. Additionlay, to build the repeater tag, an inductor or a resistor can be connected to the coil instead of a capacitor. Furthermore, a closely wound coil itself can be a repeater tag.

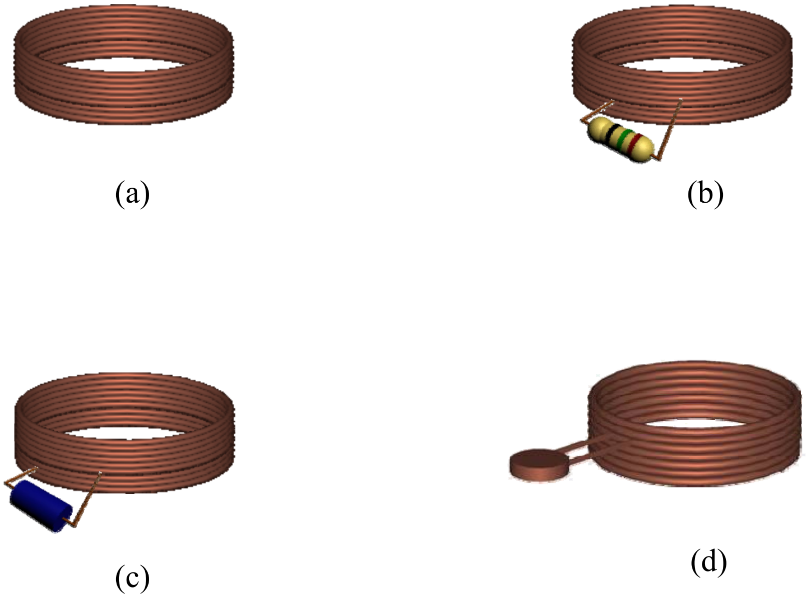
(a) (b)

(c) (d)

Figure 4.7: Various types of tag. (a) The type I tag: a closely wound coil. (b) The type II tag: a coil with a 150 ohm resistor connected to it in series. (c) The type III tag: a coil with a 3.9 uH shielded inductor connected to it in series. (d) The original repeater tag: a coil with a 471 pF ceramic capacitor connected to it in series.

With a purpose of testing as many combinations of the repeater tags and DUT as possible, all the repeater tags mentioned above are built as seen in Figure 4.7. To differentiate the other repeater tags from the original one, they are named as type I tag, type II tag and so on. The tag type I is a closely wound coil which can be modeled equivalently with the inductance and resistance of the coil. The type II tag is a coil with a resistor connected to it in series. Thus, the inductance and resistance are needed to model the tag type II in an equivalent circuit. However, both the resistor and the coil itself contribute to the resistance of an equivalent circuit. Compared to the resistor, the resistance of the coil may be negligible. The type III tag is one which has a wound coil connected to an inductor in series as in Figure 4.7. Likewise, the type III tag is modeled equivalently with the resistance and the inductance. The inductance and resistance comes from both the wound coil and the inductor.

4.2.3.2 Various types of DUT

Copper plates with two different conditions, a copper plate with a slit and a perfect copper plate which has no slit, are used for the preliminary experiment. For additional detailed experiment in this chapter, more types of DUT are manufactured by soldering a lumped circuit element, such as a resistor, an inductor, and a capacitor, across the slit in the copper plate as illustrated in Figure 4.8. The total 6 types of DUT are made as explained in the Figure 4.8. The first type is a perfect copper plate which has no slit. The second type DUT is a copper plate with slit on its surface. The type III DUT is a copper plate with a 10 ohm resistor soldered across the slit. The type IV DUT has the same configuration as the type III but it has a 10 kilo ohm resistor soldered across the slit instead of 10 ohm resistor. The type V DUT is a copper plate with a 3.9 uH (micro Henry) coil molded shielded inductor connected across the slit. A capacitor of 471 pF (pico Farad) is soldered across the slit on the copper plate surface for the type VI DUT. The idea behind the additional types of DUT is that the lumped circuit elements across the slit will help to characterize the slit so that a better equivalent circuit of the system could be built.

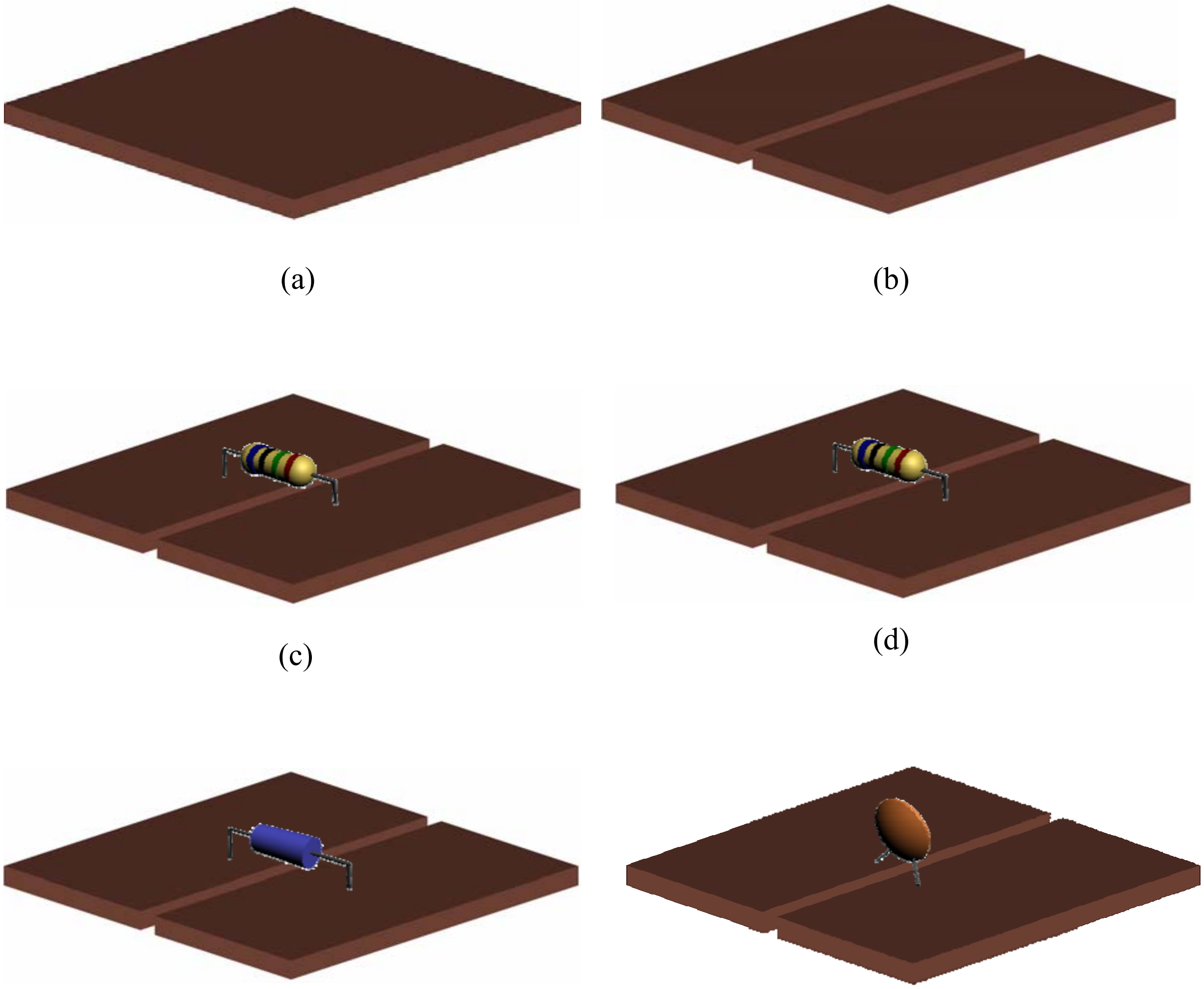
(a)

(b)

(c)

(d)

(e)

(f)

Figure 4.8: Various types of DUT. (a) The type I DUT: a perfect copper plate which has no slit. (b) The type II DUT: a copper plate with slit on its surface. (c) The type III DUT: a copper plate with a 10 ohm resistor soldered across the slit. (d) The type IV DUT: a copper plate with a 10 kilo ohm resistor soldered across the slit. (e) The type V DUT: a copper plate with a 3.9 uH inductor soldered across the slit. (f) The type VI DUT: a copper plate with a 471 uF capacitor soldered across the slit.

4.2.3.2 An equivalent circuit representation

An equivalent circuit is given in Figure 4.9 that can be applicable for the every combination of the repeater tags and the types of DUT discussed in the previous sections. In the figure, $L_{tag\,coil}$ and $R_{tag\,coil}$ stand for the inductance and resistance value attributed to the wound coil of the repeater tag. Z_{lumped} could be the resistance, inductance, capacitance or nothing depending on what kind of a lumped circuit element is connected in series with a closely wound coil to form the repeater tag. The error box in the repeater tag loop can be added to account for the error due to discrepancy between the theory and the measurement as explained in section 4.2.2. Although the copper plate with different conditions is used as DUT, it has such a high conductivity that it can be replaced with the image loops of the driver and the repeater tag as done in Figure 4.9. The solid line represents mutual interaction between real loops. However, the dashed line symbolizes mutual interaction between real and image loop, or between image loops. Z_{box} is inserted so that the equivalent circuit representation matches the measurement data with whatever copper plate depicted in section 4.2.3.1 is used as a DUT. To characterize the effect of slit in the copper plate with circuit elements, Z_{box} should be constructed in terms of passive circuit elements.

From the equivalent circuit representation in Figure 4.9, it is possible to obtain mathematical expression with an application of linear network theory to the equivalent circuit. The result is

$$\begin{bmatrix} R_{driver} + j\omega L_{driver} & j\omega M_{12} & j\omega M_{13} & j\omega M_{14} \\ j\omega M_{12} & R_{tag\,coil} + j\omega L_{tag\,coil} + + Z_{lumped} & j\omega M_{23} & j\omega M_{24} \\ j\omega M_{13} & j\omega M_{23} & j\omega L_{tag\,coil} + Z_{box} & j\omega M_{34} \\ j\omega M_{14} & j\omega M_{24} & j\omega M_{34} & j\omega L_{driver} \end{bmatrix} \begin{bmatrix} I_{driver} \\ I_{tag} \\ I_{tag,i} \\ I_{driver,i} \end{bmatrix} = \begin{bmatrix} V_s \\ 0 \\ 0 \\ 0 \end{bmatrix}$$

. (4.4)

Since all the values except Z_{box} are known or can be determined in the matrix equation in (4.4), Z_{box} can be computed with the measurement data with a little manipulation of the equation.

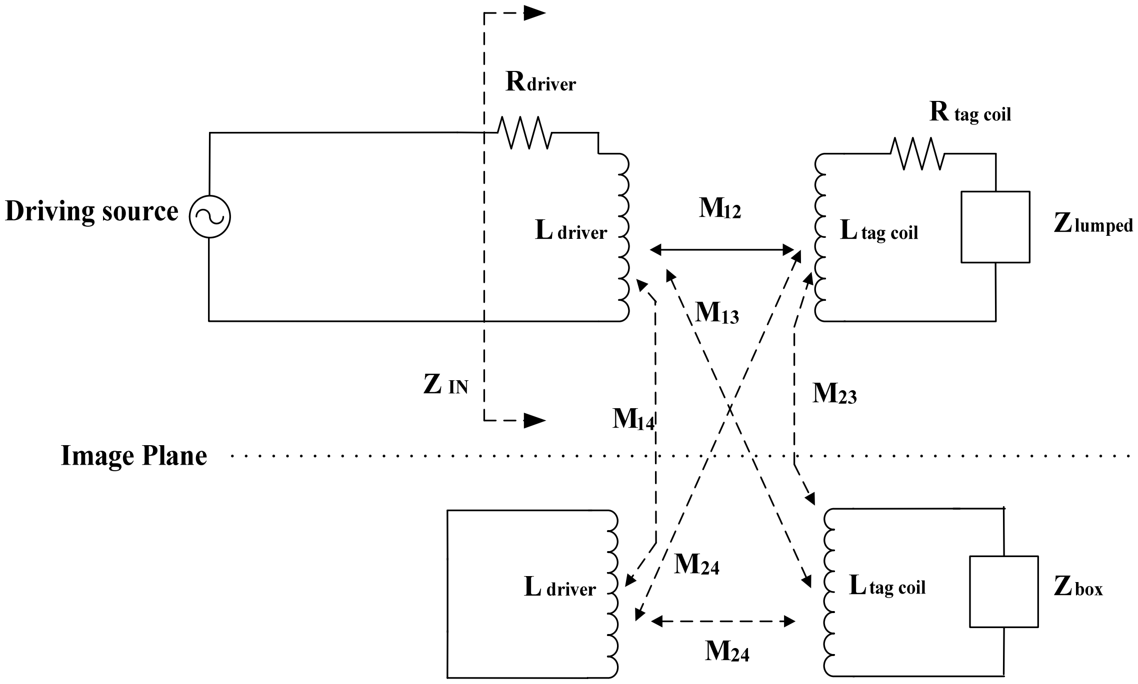

Figure 4.9: An equivalent circuit that can be applicable for the every combination of the tag and DUT types discussed in the previous sections.

4.2.3.3 Experiment with the system of the driver, the type I tag and various types of DUT

Here are the result regarding the experiment done with the system of the driver and the type I tag, and various types of DUT. The type I tag is a closely wound coil itself. Therefore, Z_{lumped} can be removed safely from the equivalent circuit representation without a significant error. The real and imaginary part of Z_{box} are presented in the Figure 4.10 through Figure 4.15. The real part of Z_{box} is less than 0.1 Ω and varies randomly around the zero. The imaginary part is negative but linearly increases in magnitude as the frequency increases, corresponding to a value of about -3.05 micro Henries (μH). For comparison, note the inductance of the repeater tag for these measurements is about 3.38 micro Henries (μH). The characteristics of the real and imaginary part are tabulated in the Table 4.1. The plots don’t seem to depend on the different types of the DUT. Consequently, the characteristic of the slit cannot be determined from the experiment done with the type I tag and various types of DUT.

Figure	Tag	DUT	$\mathrm{Re}\left(Z_{box}\right)$	$\mathrm{Im}\left(Z_{box}\right)$
4.10	Coil Loop	No Slit	1. ~ shape 2. $\frac{\sigma(\mathrm{Re})}{avg(\mathrm{Re})}$ = -2.047267	1. Linearly dependent on frequency 2. Slope = -3.05 uH
4.11	Coil Loop	Slit	1. ~ shape 2. $\frac{\sigma(\mathrm{Re})}{avg(\mathrm{Re})}$ = -1.495684	1. Linearly dependent on frequency 2. Slope = -3.04 uH
4.12	Coil Loop	Slit + Resistor (10 ohm)	1. ~ shape 2. $\frac{\sigma(\mathrm{Re})}{avg(\mathrm{Re})}$ = -1.323541	1. Linearly dependent on frequency 2. Slope = -3.05 uH
4.13	Coil Loop	Slit + Resistor (10Kohm)	1. ~ shape 2. $\frac{\sigma(\mathrm{Re})}{avg(\mathrm{Re})}$ = -1.494807	1. Linearly dependent on frequency 2. Slope = -3.04 uH
4.14	Coil Loop	Slit + Inductor (3.9 uH)	1. ~ shape 2. $\frac{\sigma(\mathrm{Re})}{avg(\mathrm{Re})}$ = -1.280767	1. Linearly dependent on frequency 2. Slope = -3.04 uH
4.15	Coil Loop	Slit + Capacitor (471 uF)	1. ~ shape 2. $\frac{\sigma(\mathrm{Re})}{avg(\mathrm{Re})}$ = -1.534676	1. Linearly dependent on frequency 2. Slope = -3.05 uH

Table 4.1: Summary of the characteristics of the real and imaginary part of the Z_{box} in the plots from Figure 4.10 through Figure 4.15

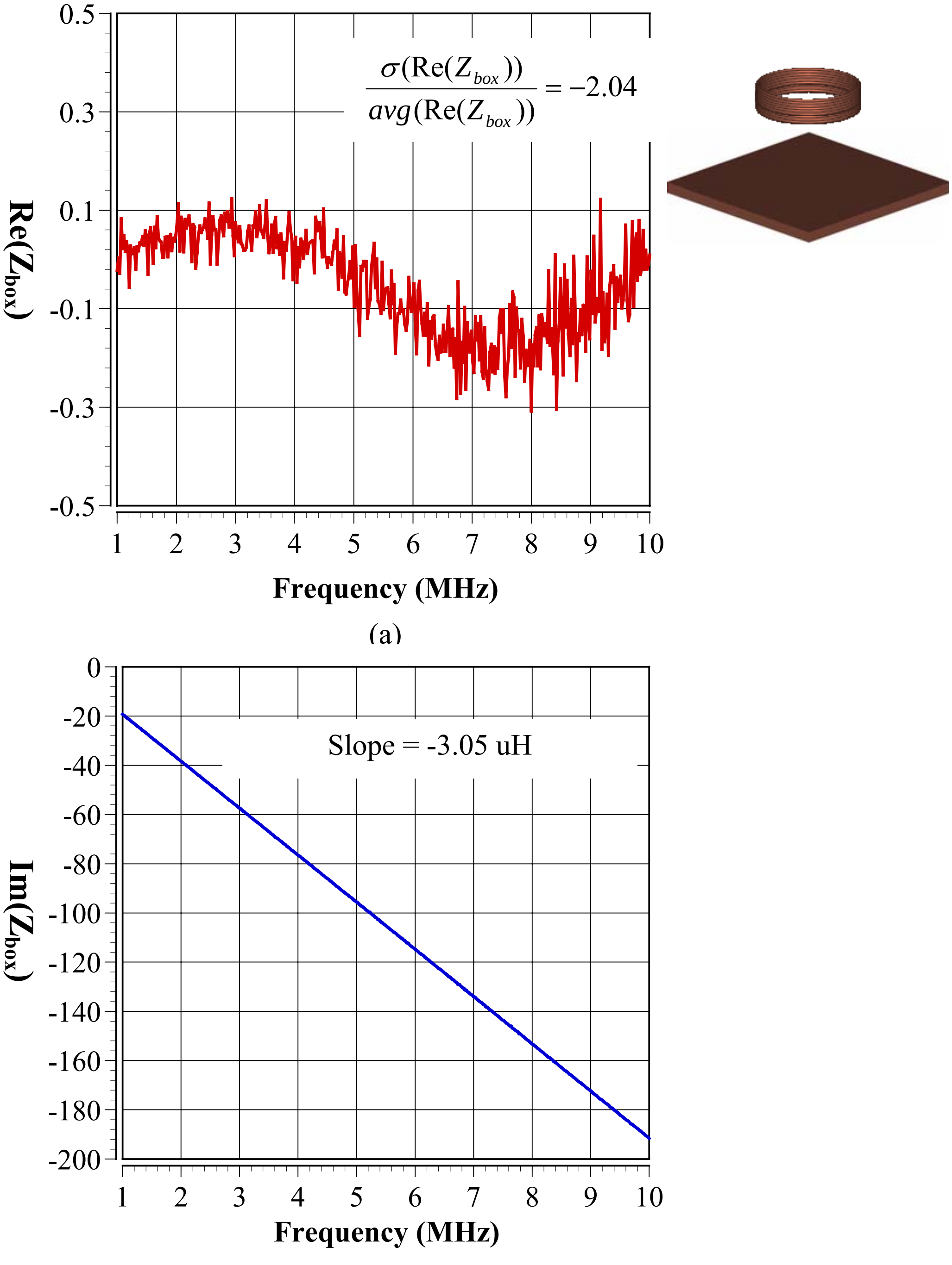

(a)

(b)

Figure 4.10: Z_{box} is computed for the system of the driver coil, the type I tag and the type I DUT. (a) The real part of Z_{box}. (b) The imaginary part of Z_{box}.

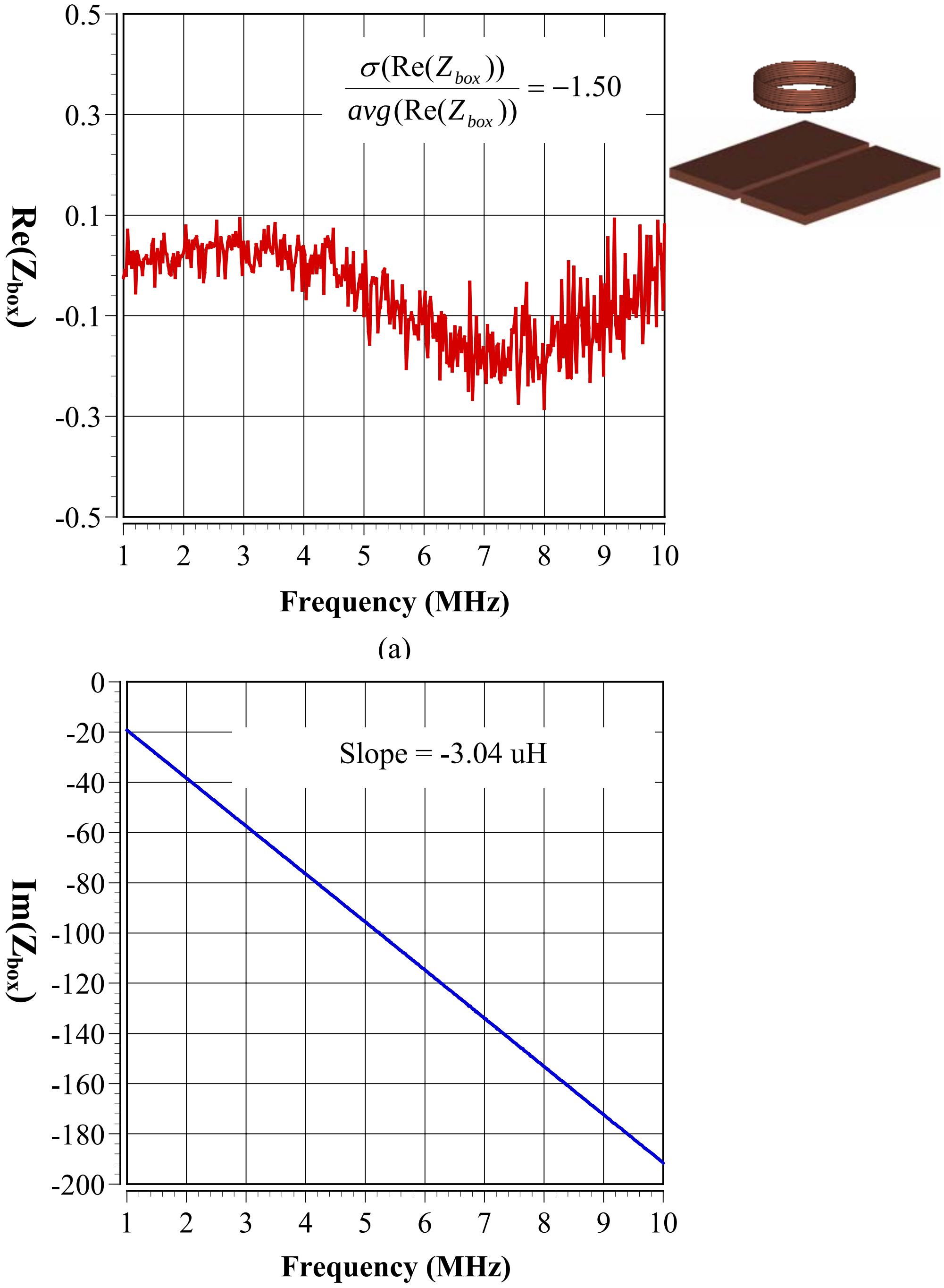

(a)

(b)

Figure 4.11: Z_{box} is computed for the system of the driver coil, the type I tag and the type II DUT. (a) The real part of Z_{box}. (b) The imaginary part of Z_{box}.

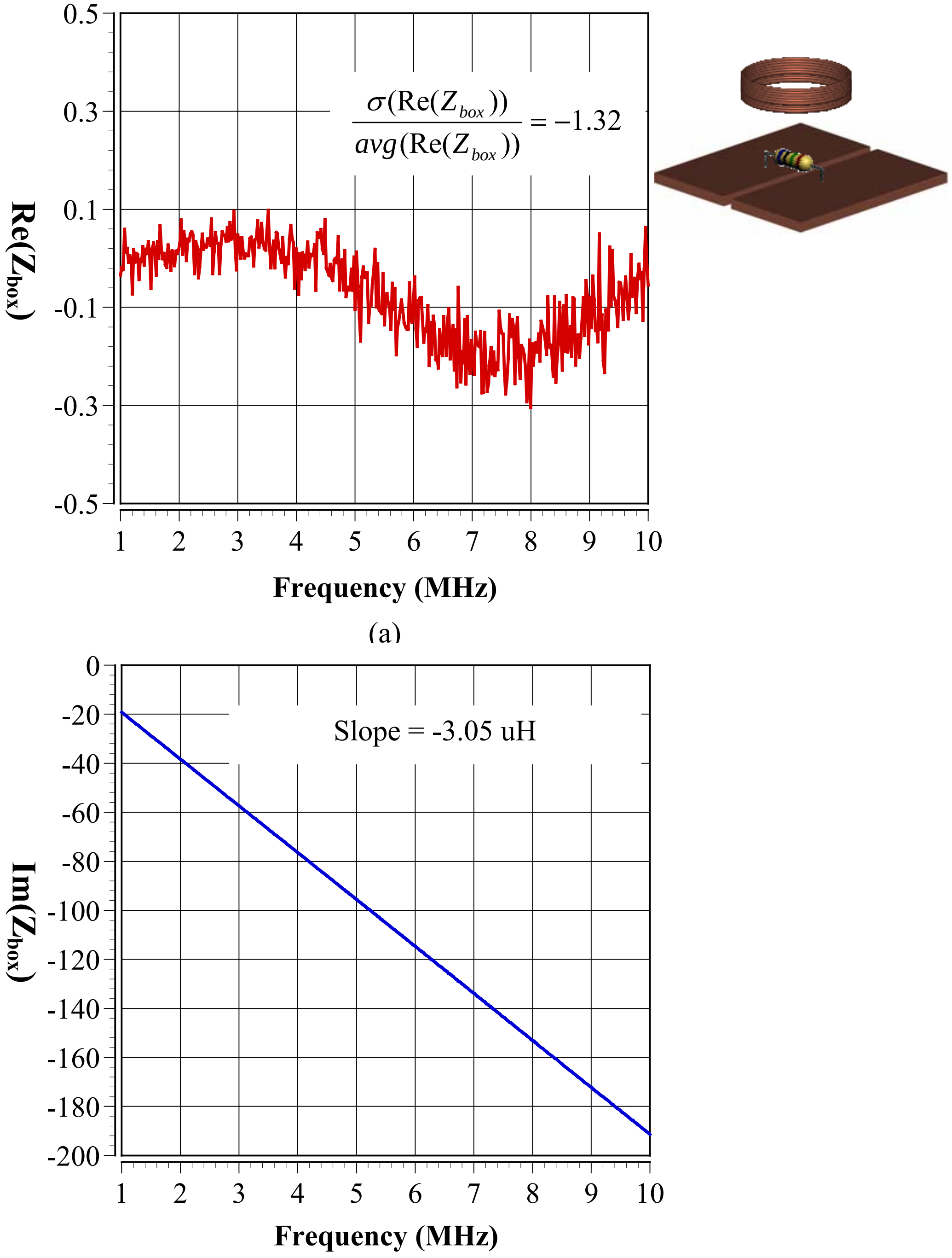

(a)

(b)

Figure 4.12: Z_{box} is computed for the system of the driver coil, the type I tag and the type III DUT. (a) The real part of Z_{box}. (b) The imaginary part of Z_{box}.

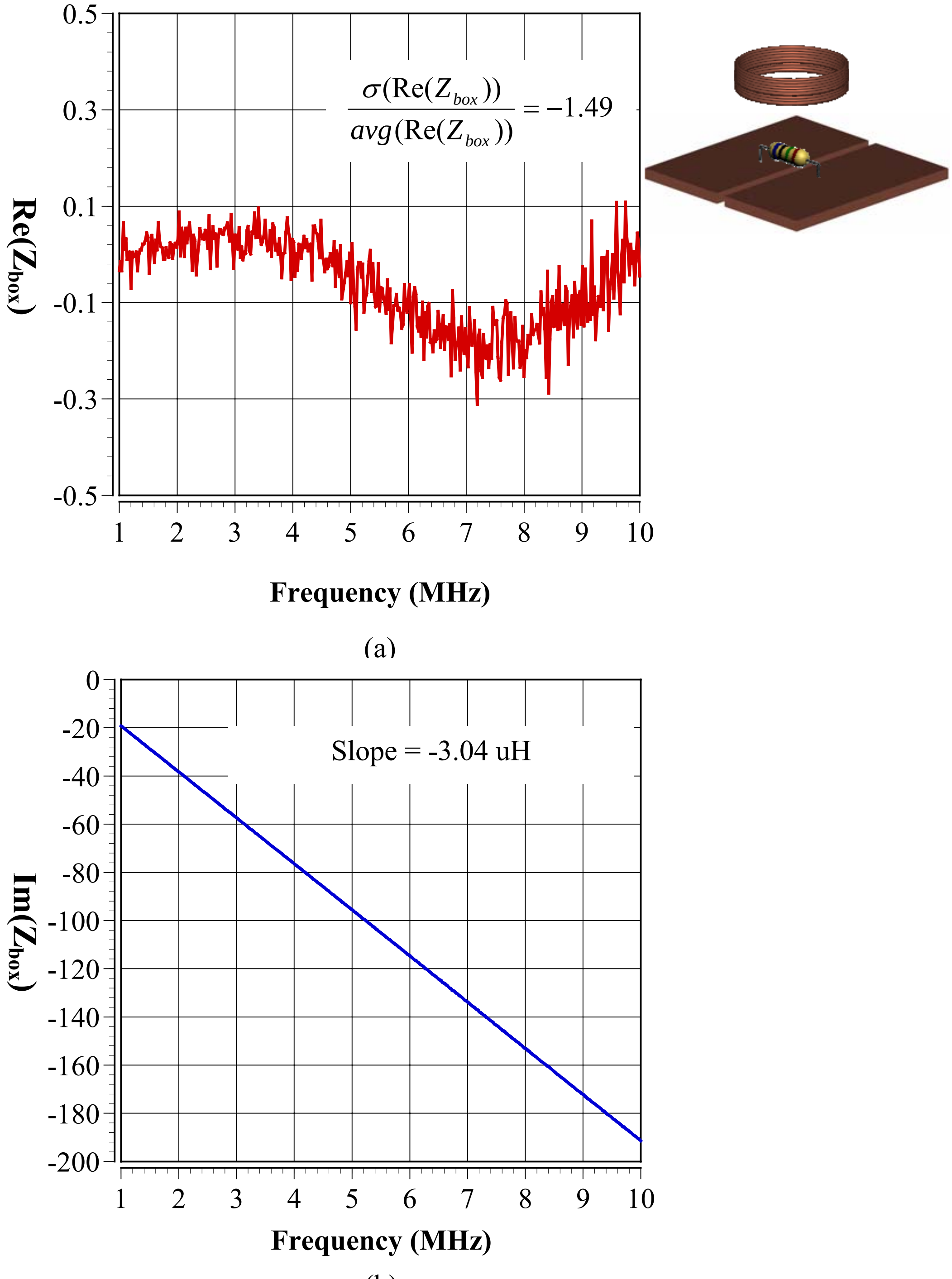

(a)

(b)

Figure 4.13: Z_{box} is computed for the system of the driver coil, the type I tag and the type IV DUT. (a) The real part of Z_{box}. (b) The imaginary part of Z_{box}.

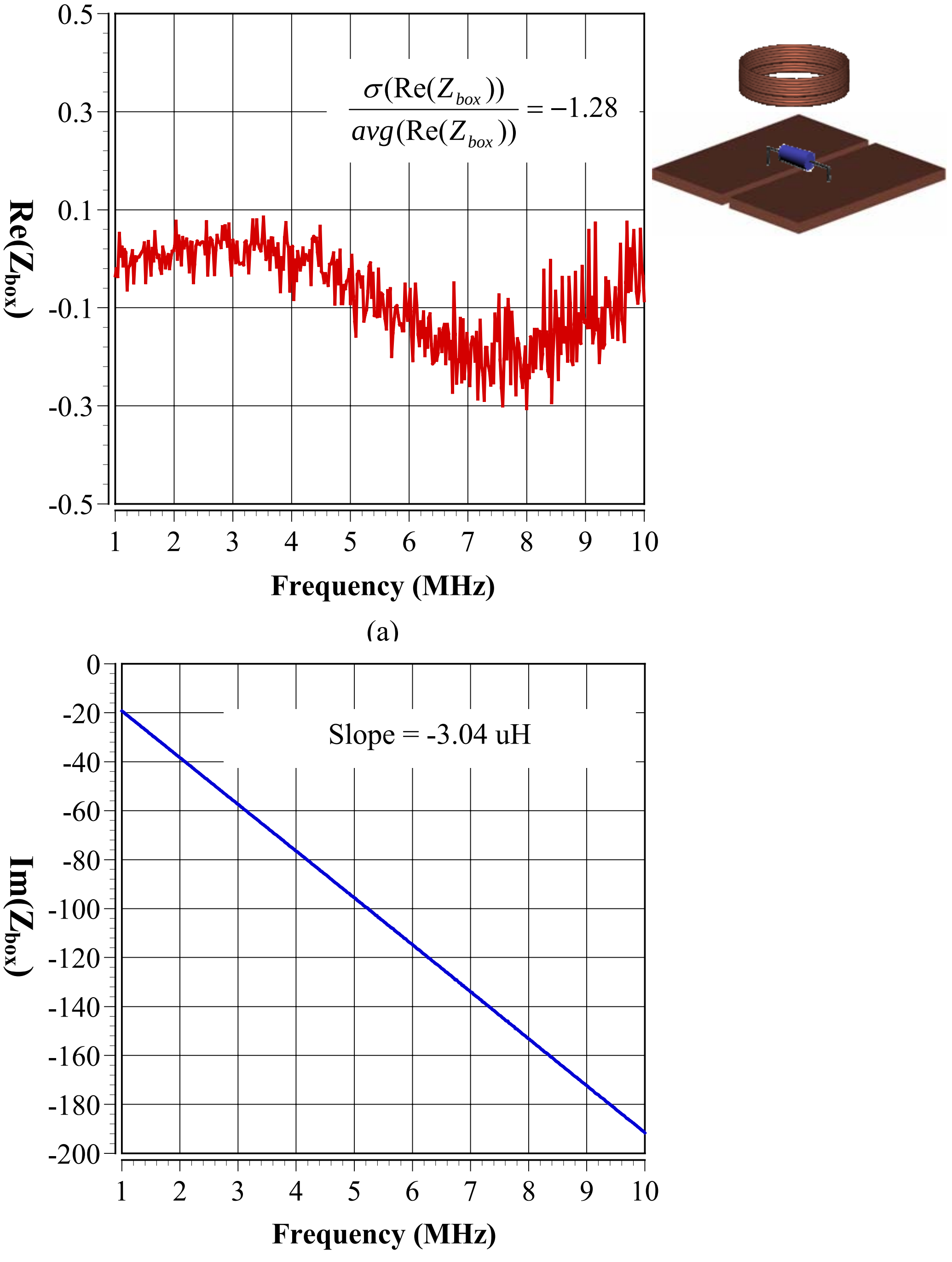

(a)

(b)

Figure 4.14: Z_{box} is computed for the system of the driver coil, the type I tag and the type V DUT. (a) The real part of Z_{box}. (b) The imaginary part of Z_{box}.

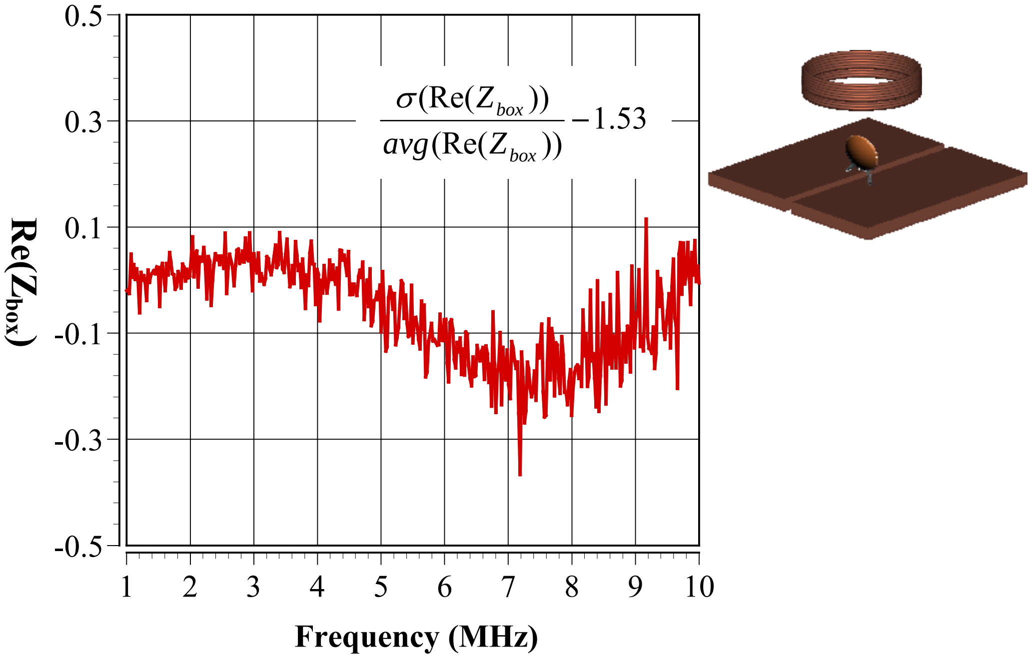

(a)

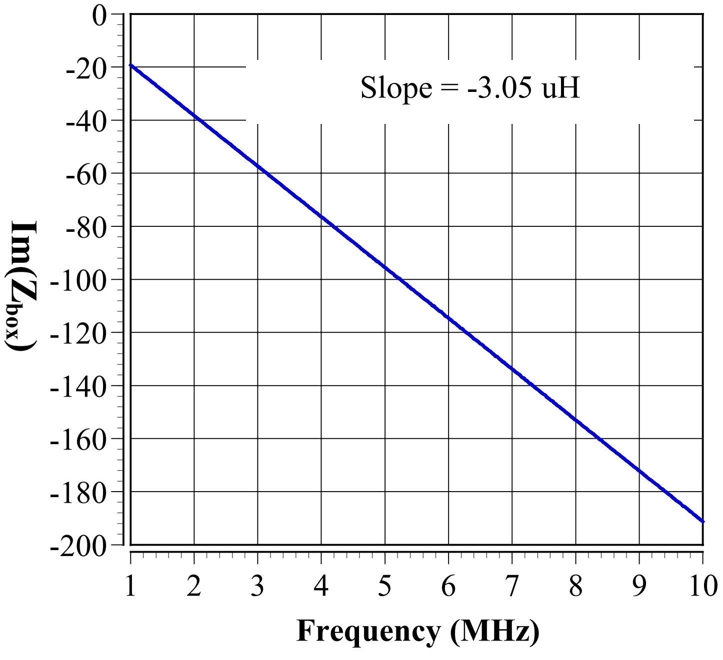

(b)

Figure 4.15: Z_{box} is computed for the system of the driver coil, the type I tag and the type VI DUT. (a) The real part of Z_{box}. (b) The imaginary part of Z_{box}.

4.2.3.3 Experiment with the system of the driver, the type II tag and various types of DUT

With the various types of DUT depicted earlier, the same experiment has been carried out with the tag type II. The tag type II is a coil with a 150 ohm resistor connected to it in series. Consequently, Z_{lumped} represents the resistance of the resistor connected to the coil. From the Figure 4.16 to Figure 4.21, the real and imaginary part of Z_{box} are plotted. The real part of the plot changes a little depending on the type of DUT. The characteristics of the real and imaginary part are tabulated in the Table 4.2. The imaginary part is also linearly dependent on the frequency and the corresponding negative slope is about -3.10 micro Henries(μH). However, the imaginary part of Z_{box} is independent of the type of DUT. Thus, the equivalent circuit of the slit could not be determined from the experiment done with the type II tag and various types of DUT.

Figure	Tag	DUT	$\mathrm{Re}(Z_{box})$	$\mathrm{Im}(Z_{box})$
4.16	Coil Loop + Resistor (150 ohm)	No Slit	1. Varies around zero (0 → -0.2→ 0.75) 2. $\frac{\sigma(\mathrm{Re})}{avg(\mathrm{Re})}$ = 5.045803	1. Linearly dependent on frequency 2. Slope = -3.16 uH
4.17	Coil Loop + Resistor (150 ohm)	Slit	1. Looks like linearly increasing (0 →2.3) 2. $\frac{\sigma(\mathrm{Re})}{avg(\mathrm{Re})}$ = 0.884133	1. Linearly dependent on frequency 2. Slope = -3.10 uH
4.18	Coil Loop + Resistor (150 ohm)	Slit + Resistor (10 ohm)	1. Looks like linearly increasing (0→1.7) 2. $\frac{\sigma(\mathrm{Re})}{avg(\mathrm{Re})}$ = 0.875448	1. Linearly dependent on frequency 2. Slope = -3.13 uH
4.19	Coil Loop + Resistor (150 ohm)	Slit + Resistor (10Kohm)	1. Looks like linearly increasing (0→ 1.7) 2. $\frac{\sigma(\mathrm{Re})}{avg(\mathrm{Re})}$ = 0.941169	1. Linearly dependent on frequency 2. Slope = -3.13 uH
4.20	Coil Loop + Resistor (150 ohm)	Slit + Inductor (3.9 uH)	1. Looks like linearly increasing (0→ 2.2) 2. $\frac{\sigma(\mathrm{Re})}{avg(\mathrm{Re})}$ = 0.828946	1. Linearly dependent on frequency 2. Slope = -3.10 uH
4.21	Coil Loop + Resistor (150 ohm)	Slit + Capacitor (471 uF)	1. Looks like linearly increasing (0→ 2.2) 2. $\frac{\sigma(\mathrm{Re})}{avg(\mathrm{Re})}$ = 0.816115	1. Linearly dependent on frequency 2. Slope = -3.10 uH

Table 4.2: Summary of the characteristics of the real and imaginary part of the Z_{box} in the plots from Figure 4.16 through Figure 4.21

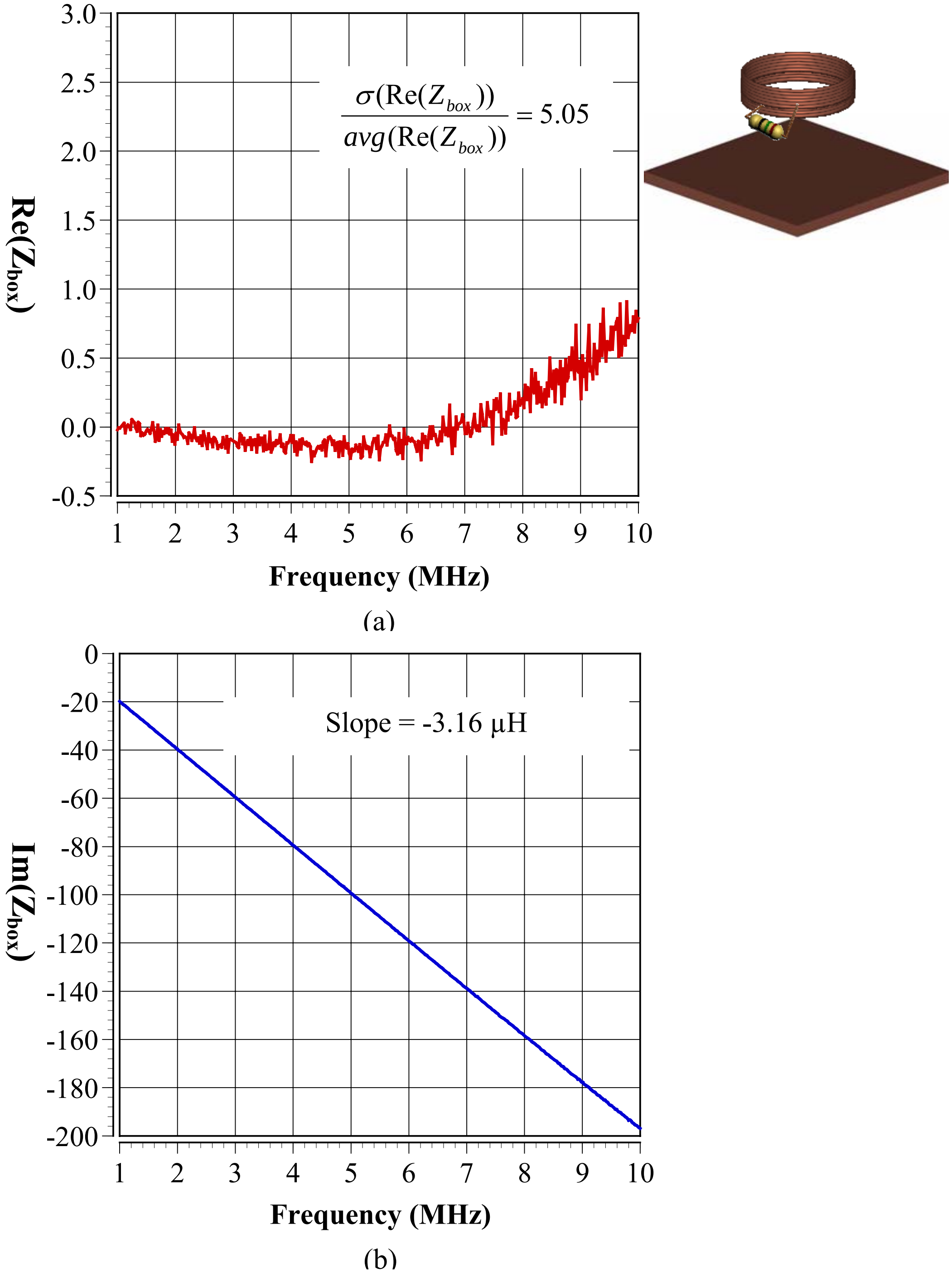

(a)

(b)

Figure 4.16: Z_{box} is computed for the system of the driver coil, the type II tag and the type I DUT. (a) The real part of Z_{box}. (b) The imaginary part of Z_{box}.

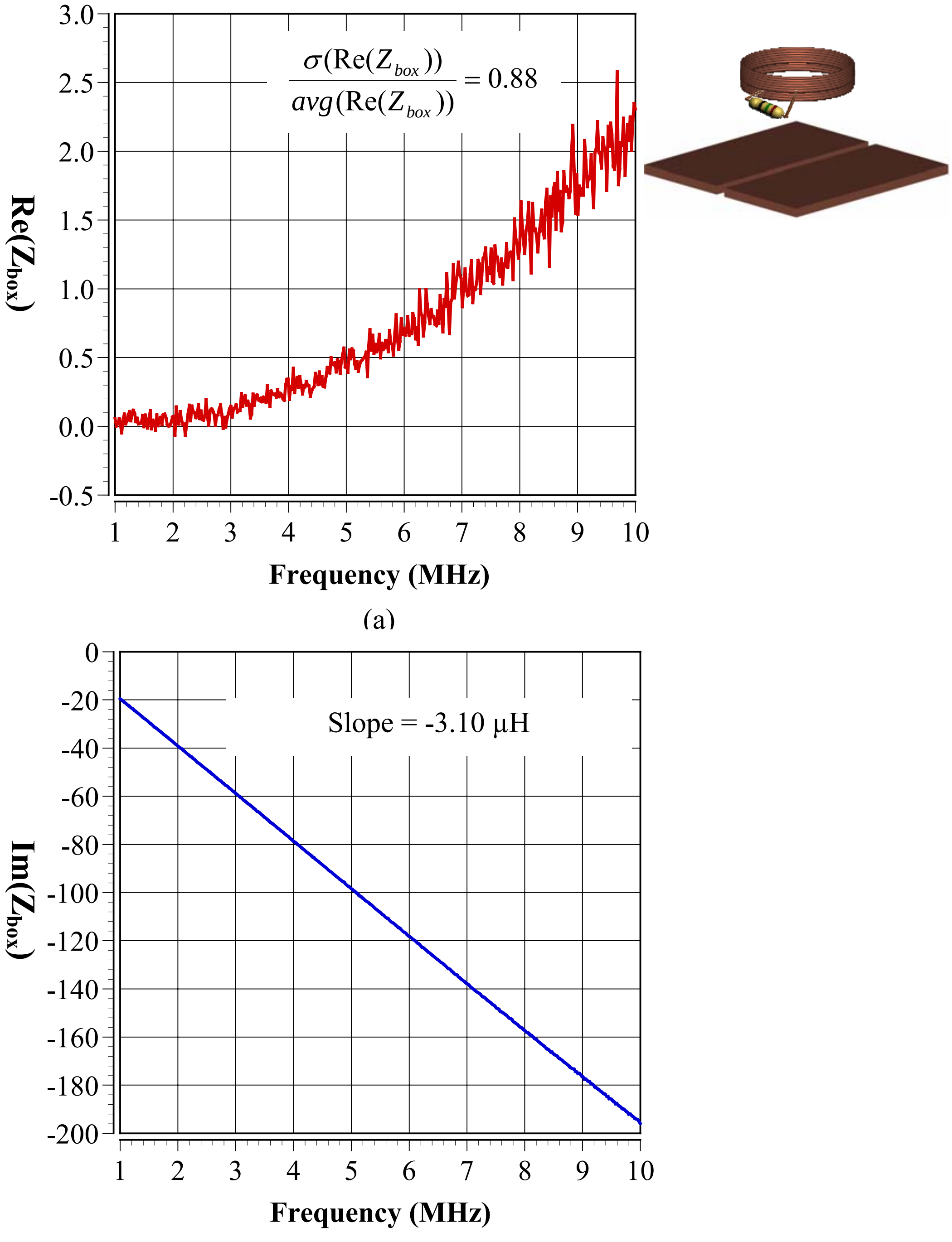

(a)

(b)

Figure 4.17: Z_{box} is computed for the system of the driver coil, the type II tag and the type II DUT. (a) The real part of Z_{box}. (b) The imaginary part of Z_{box}.

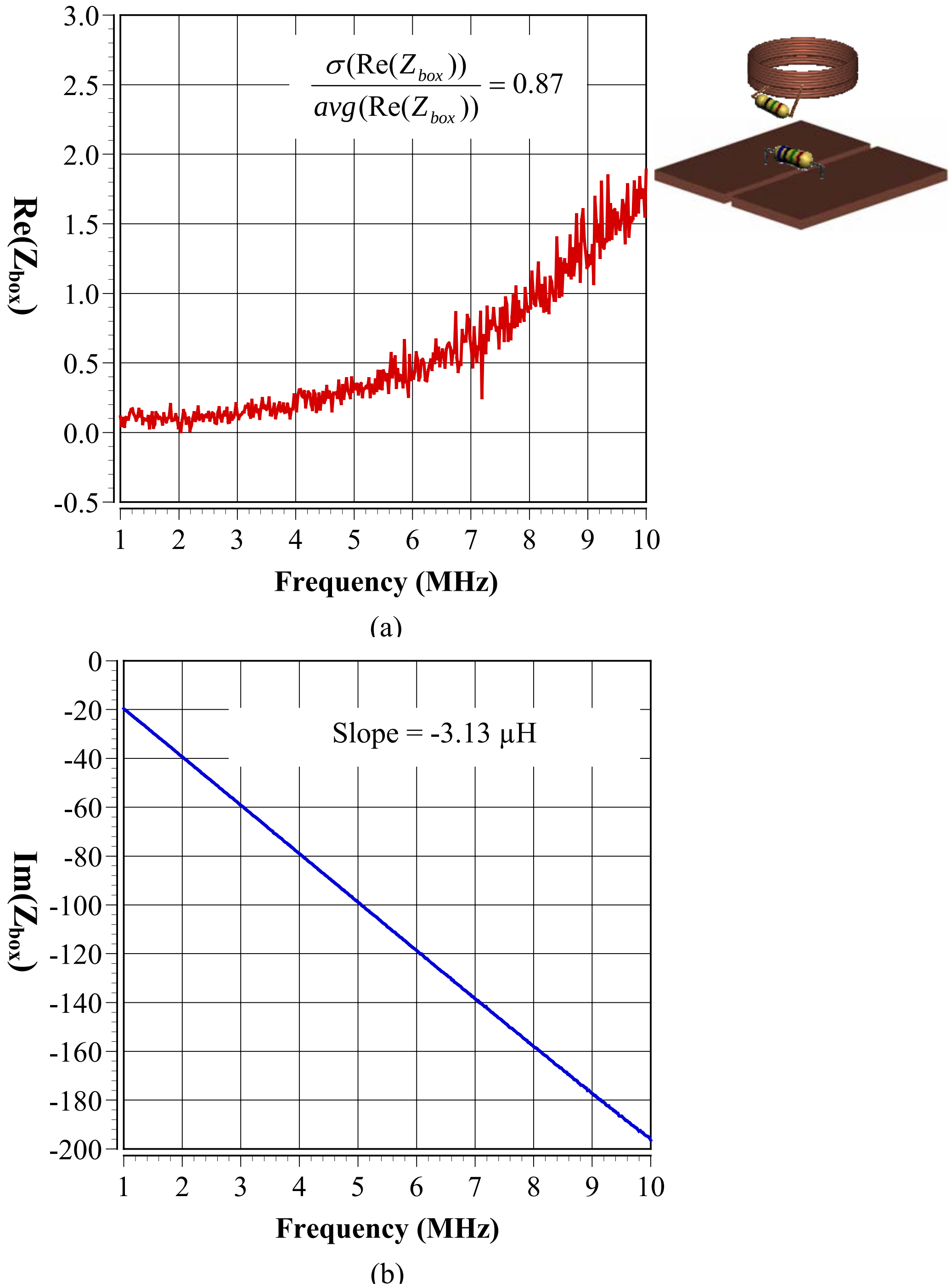

(a)

(b)

Figure 4.18: Z_{box} is computed for the system of the driver coil, the type II tag and the type III DUT. (a) The real part of Z_{box}. (b) The imaginary part of Z_{box}.

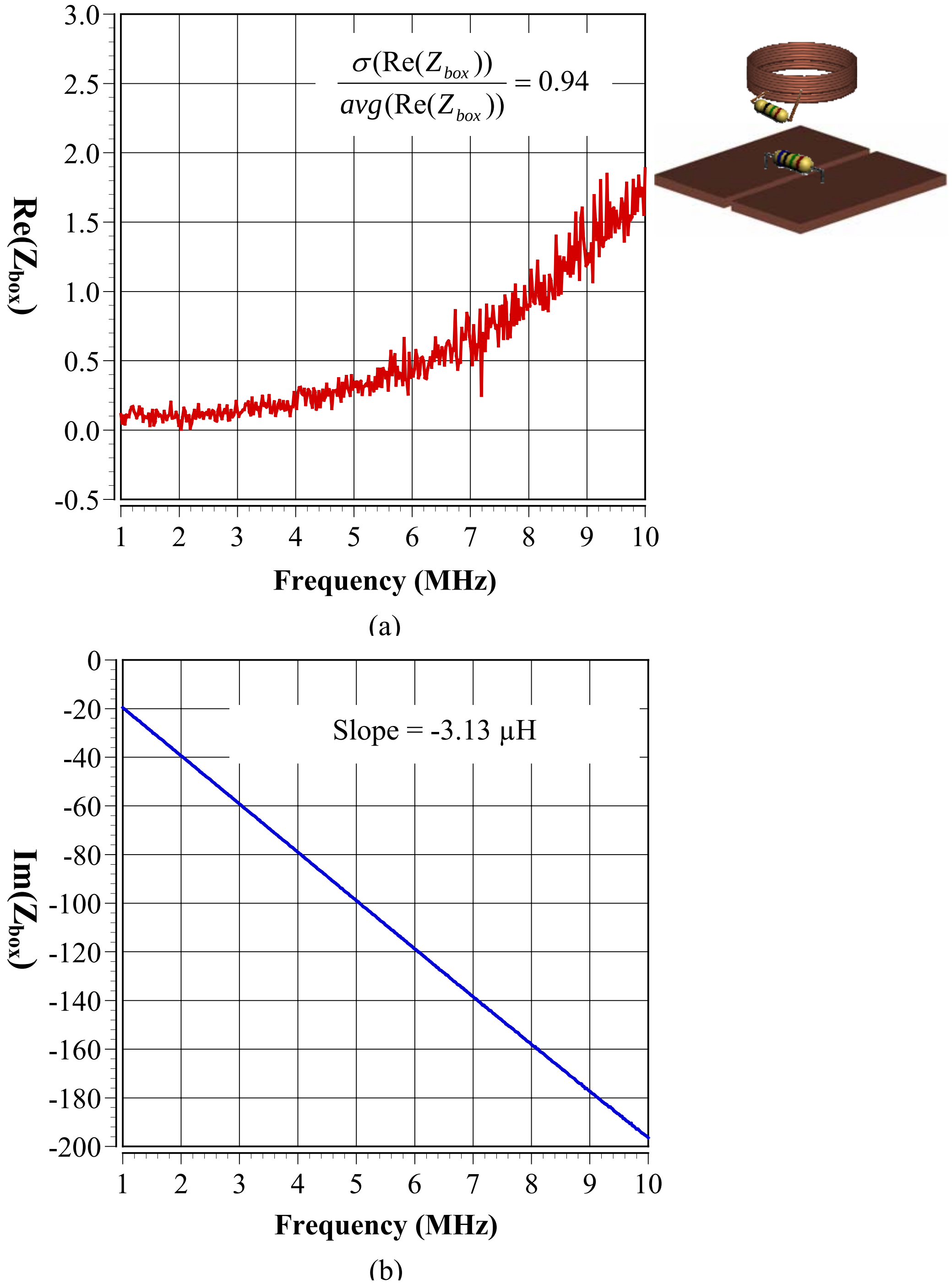

(a)

(b)

Figure 4.19: Z_{box} is computed for the system of the driver coil, the type II tag and the type IV DUT. (a) The real part of Z_{box}. (b) The imaginary part of Z_{box}.

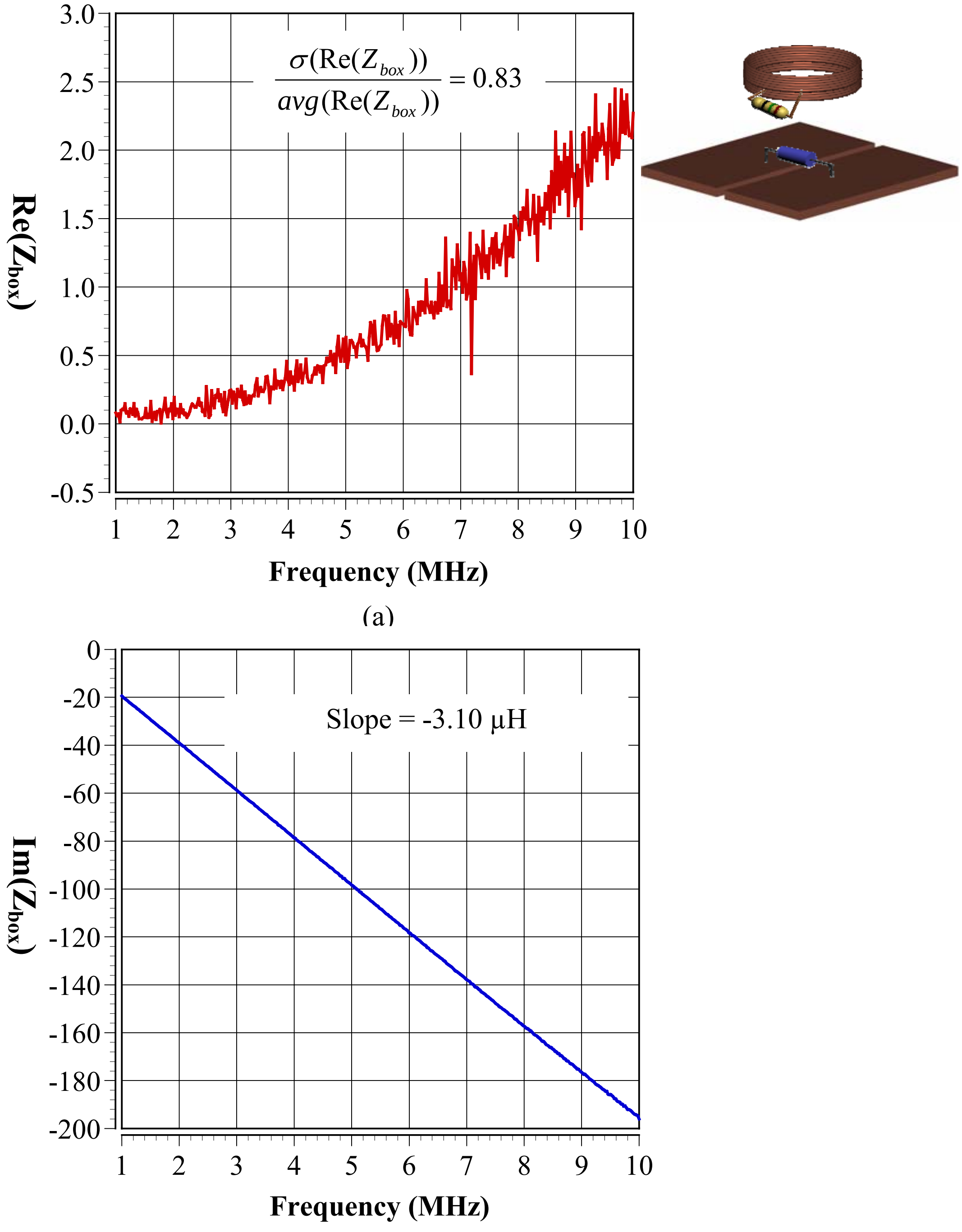

(a)

(b)

Figure 4.20: Z_{box} is computed for the system of the driver coil, the type II tag and the type V DUT. (a) The real part of Z_{box}. (b) The imaginary part of Z_{box}.

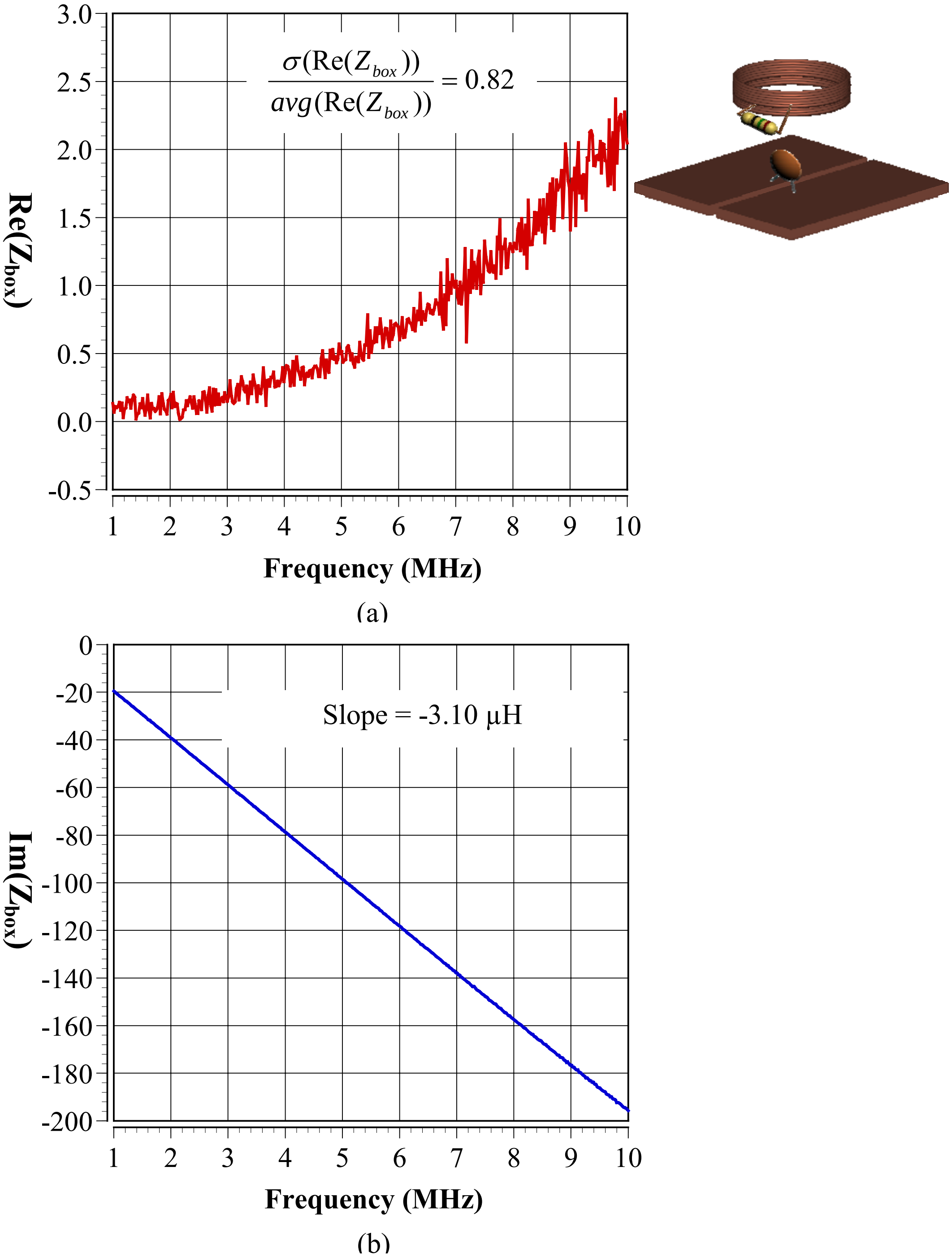

(a)

(b)

Figure 4.21: Z_{box} is computed for the system of the driver coil, the type II tag and the type VI DUT. (a) The real part of Z_{box}. (b) The imaginary part of Z_{box}.

4.2.3.3 Experiment with the system of the driver, the type III tag and various types of DUT

In this section, the results are presented regarding the experiment done with the system of the driver and the type III tag, and various types of DUT. The type III tag is the one which has a wound coil connected to a 3.9 uF inductor in series Therefore, Z_{lumped} can be expressed as the impedance of the inductor. That is to say, Z_{lumped} is $j\omega L_{inductor}$. The real and imaginary part of Z_{box} are presented in the Figure 4.22 through Figure 4.27.

Figure	Tag	DUT	$\mathrm{Re}(Z_{box})$	$\mathrm{Im}(Z_{box})$
4.22	Coil Loop + Inductor (3.9 uH)	No Slit	1. Initially looks like flat ,then start to increase linearly a little (-0.02 → 0.18) 2. $\frac{\sigma(\mathrm{Re})}{avg(\mathrm{Re})} = 5.35945$	1. Linearly dependent on frequency 2. Slope = -3.07 µH
4.23	Coil Loop + Inductor (3.9 uH)	Slit	1. Initially looks like flat ,then start to increase linearly a little (-0.1 → 0.18) 2. $\frac{\sigma(\mathrm{Re})}{avg(\mathrm{Re})} = -5.586225$	1. Linearly dependent on frequency 2. Slope = -3.05 µH
4.24	Coil Loop + Inductor (3.9 uH)	Slit + Resistor (10 ohm)	1. Initially looks like flat ,then start to increase linearly a little (-0.06 → 0.22) 2. $\frac{\sigma(\mathrm{Re})}{avg(\mathrm{Re})} = 15.938681$	1. Linearly dependent on frequency 2. Slope = -3.06 µH
4.25	Coil Loop + Inductor (3.9 uH)	Slit + Resistor (10K ohm)	1. Initially looks like flat ,then start to increase linearly a little(-0.03 → 0.38) 2. $\frac{\sigma(\mathrm{Re})}{avg(\mathrm{Re})} = 2.427593$	1. Linearly dependent on frequency 2. slope = -3.05 µH
4.26	Coil Loop + Inductor (3.9 uH)	Slit + Inductor (3.9 uH)	1. Initially looks like flat ,then start to increase linearly a little (-0.06 → 0.34) 2. $\frac{\sigma(\mathrm{Re})}{avg(\mathrm{Re})} = 4.115804$	1. Linearly dependent on frequency 2. Slope = -3.05 µH
4.27	Coil Loop + Inductor (3.9 uH)	Slit + Capacitor (471 uF)	1. Initially looks like flat ,then start to increase linearly a little(-0.02 → 0.42) 2. $\frac{\sigma(\mathrm{Re})}{avg(\mathrm{Re})} = 1.776393$	1. Linearly dependent on frequency 2. Slope = -3.05 µH

Table 4.3: Summary of the characteristics of the real and imaginary part of the Z_{box} in the plots from Figure 4.22 through Figure 4.27

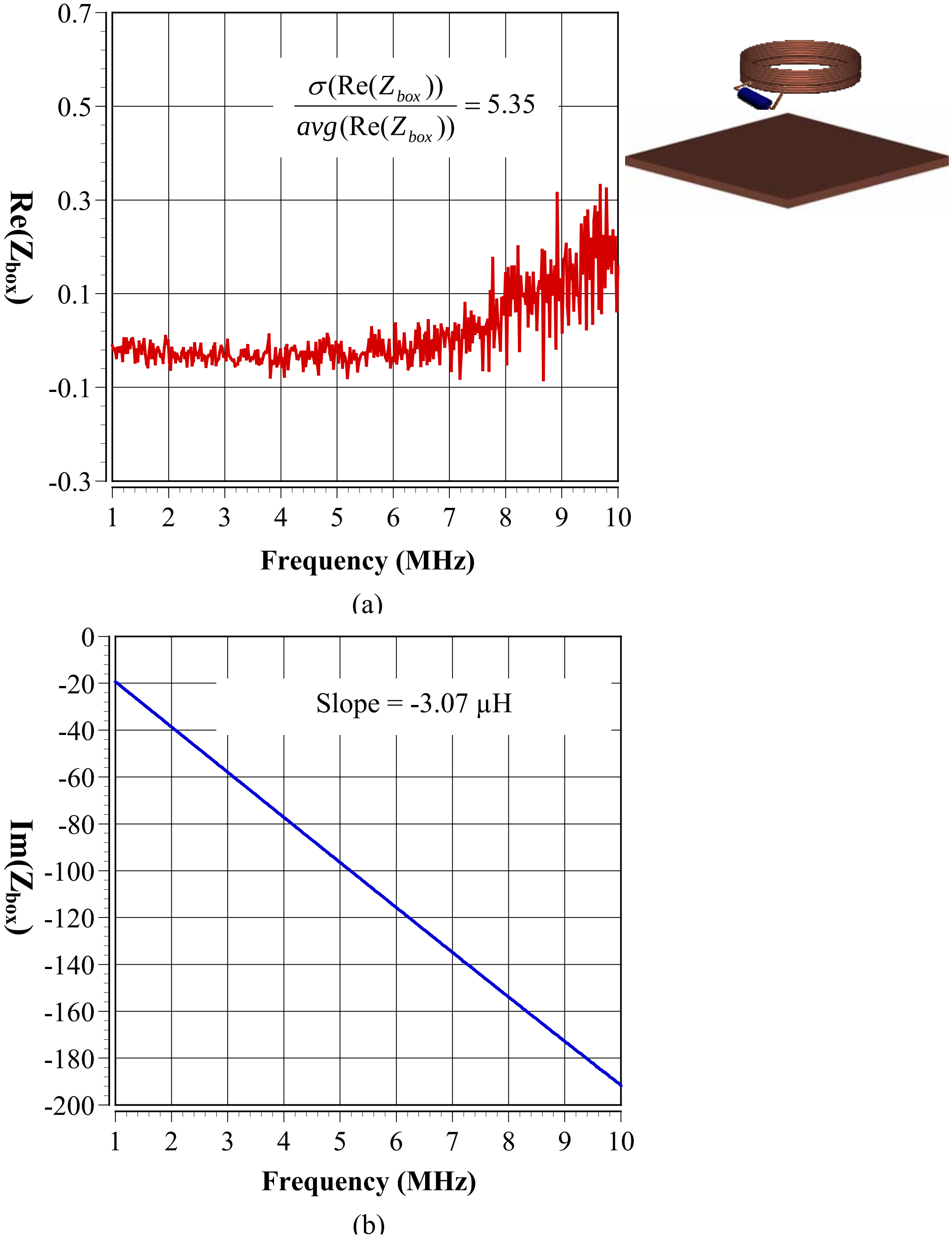

(a)

(b)

Figure 4.22: Z_{box} is computed for the system of the driver coil, the type III tag and the type I DUT. (a) The real part of Z_{box}. (b) The imaginary part of Z_{box}.

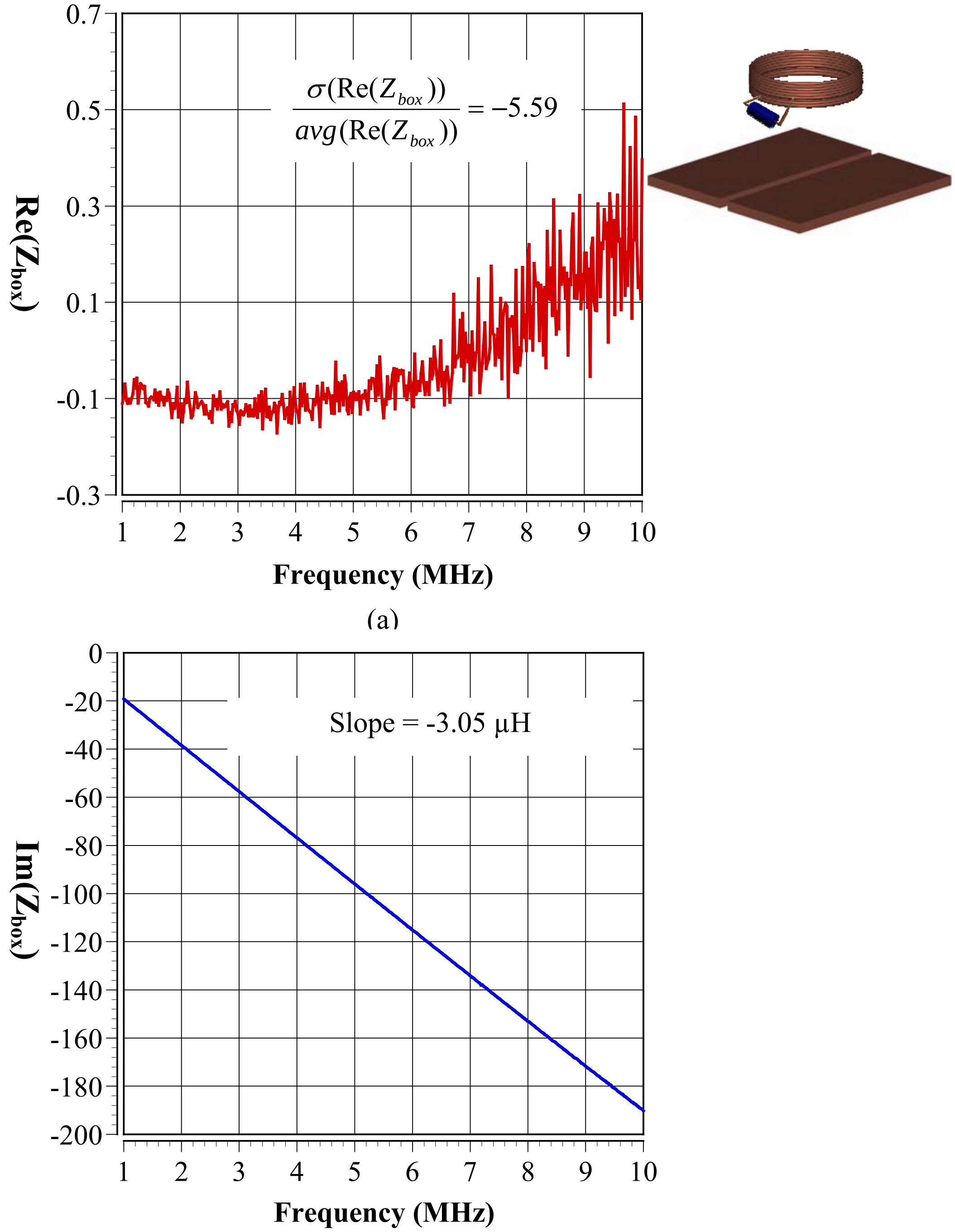

(a)

(b)

Figure 4.23: Z_{box} is computed for the system of the driver coil, the type III tag and the type II DUT. (a) The real part of Z_{box}. (b) The imaginary part of Z_{box}.

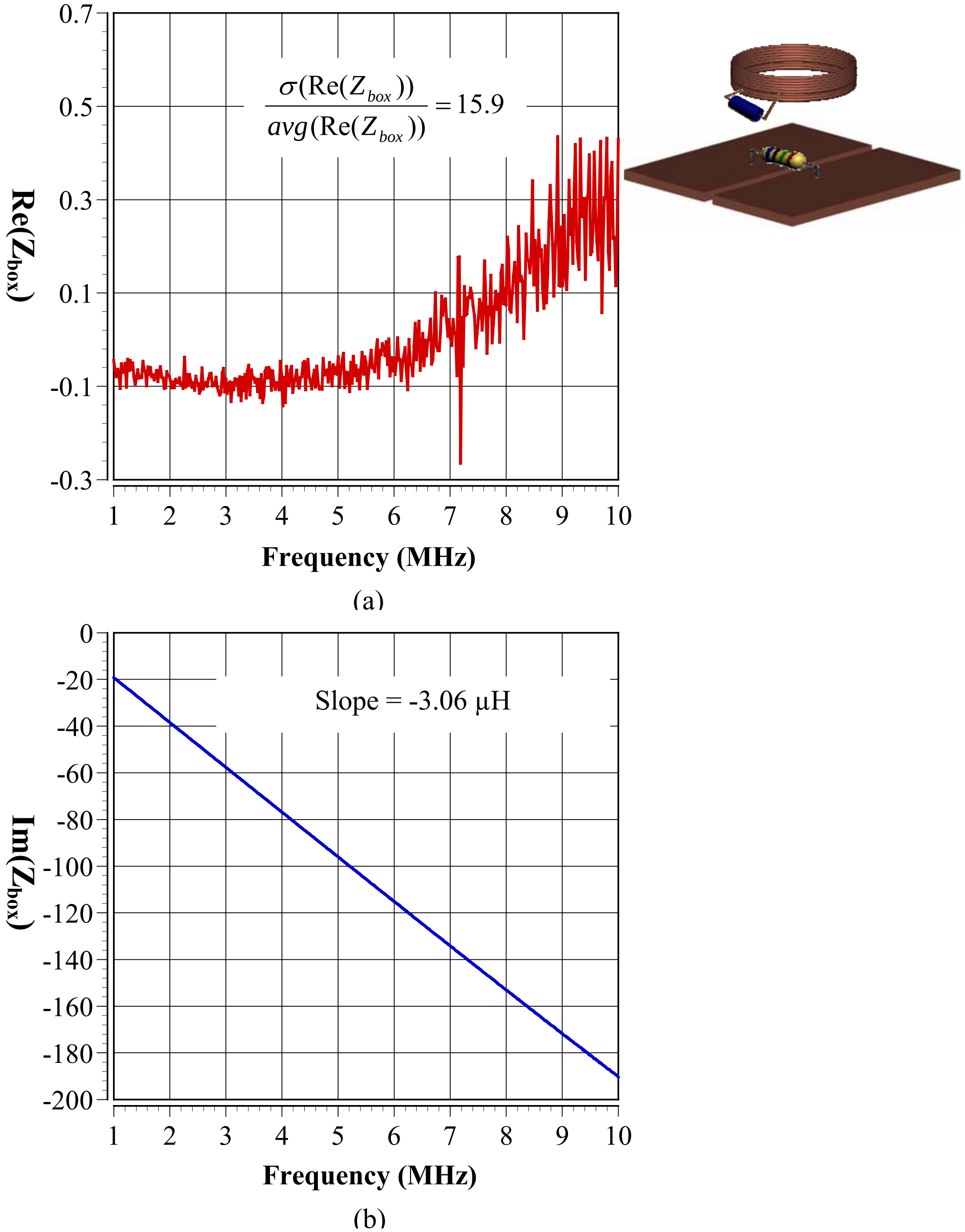

Figure 4.24: Z_{box} is computed for the system of the driver coil, the type III tag and the type III DUT. (a) The real part of Z_{box}. (b) The imaginary part of Z_{box}.

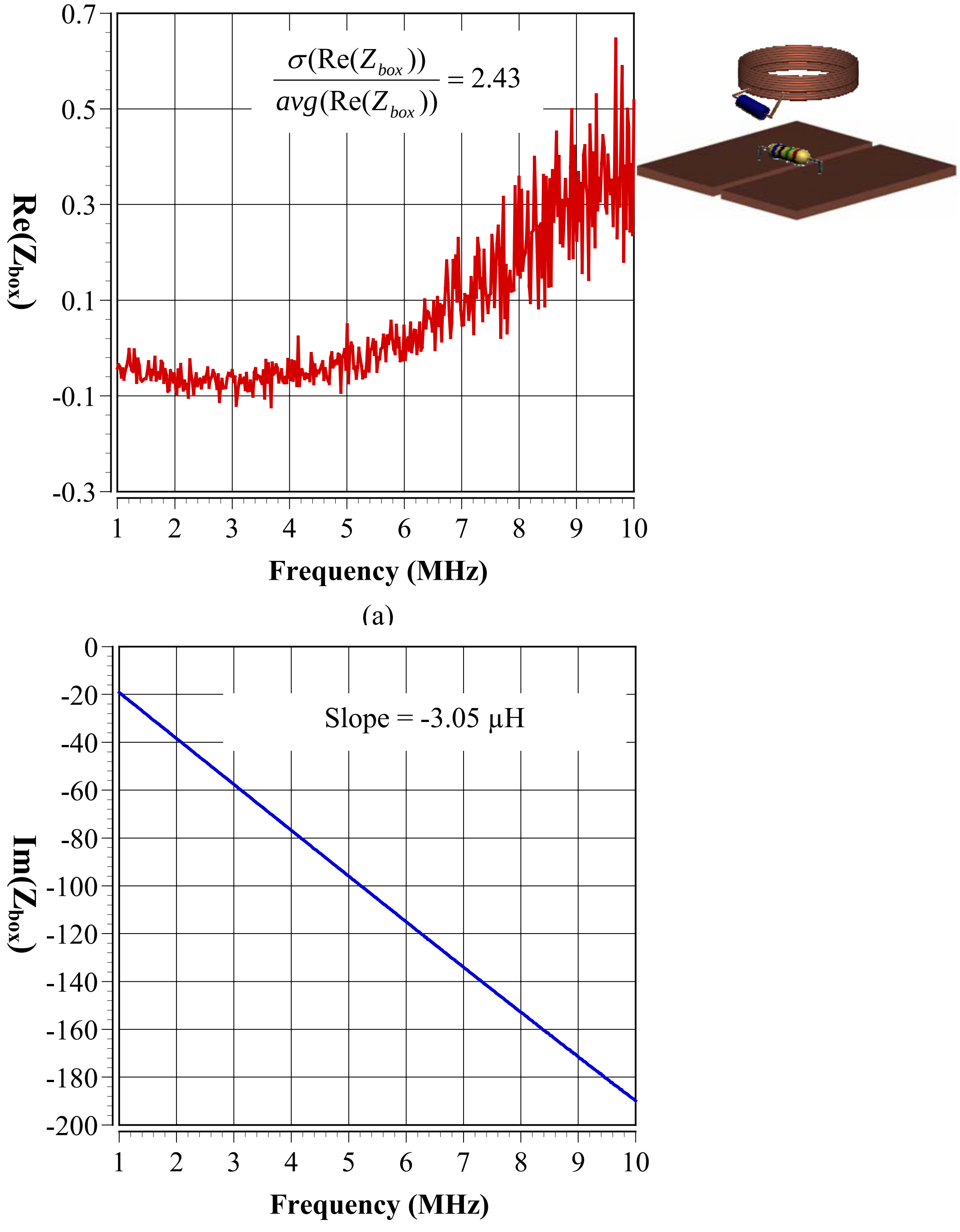

(a)

(b)

Figure 4.25: Z_{box} is computed for the system of the driver coil, the type III tag and the type IV DUT. (a) The real part of Z_{box}. (b) The imaginary part of Z_{box}.

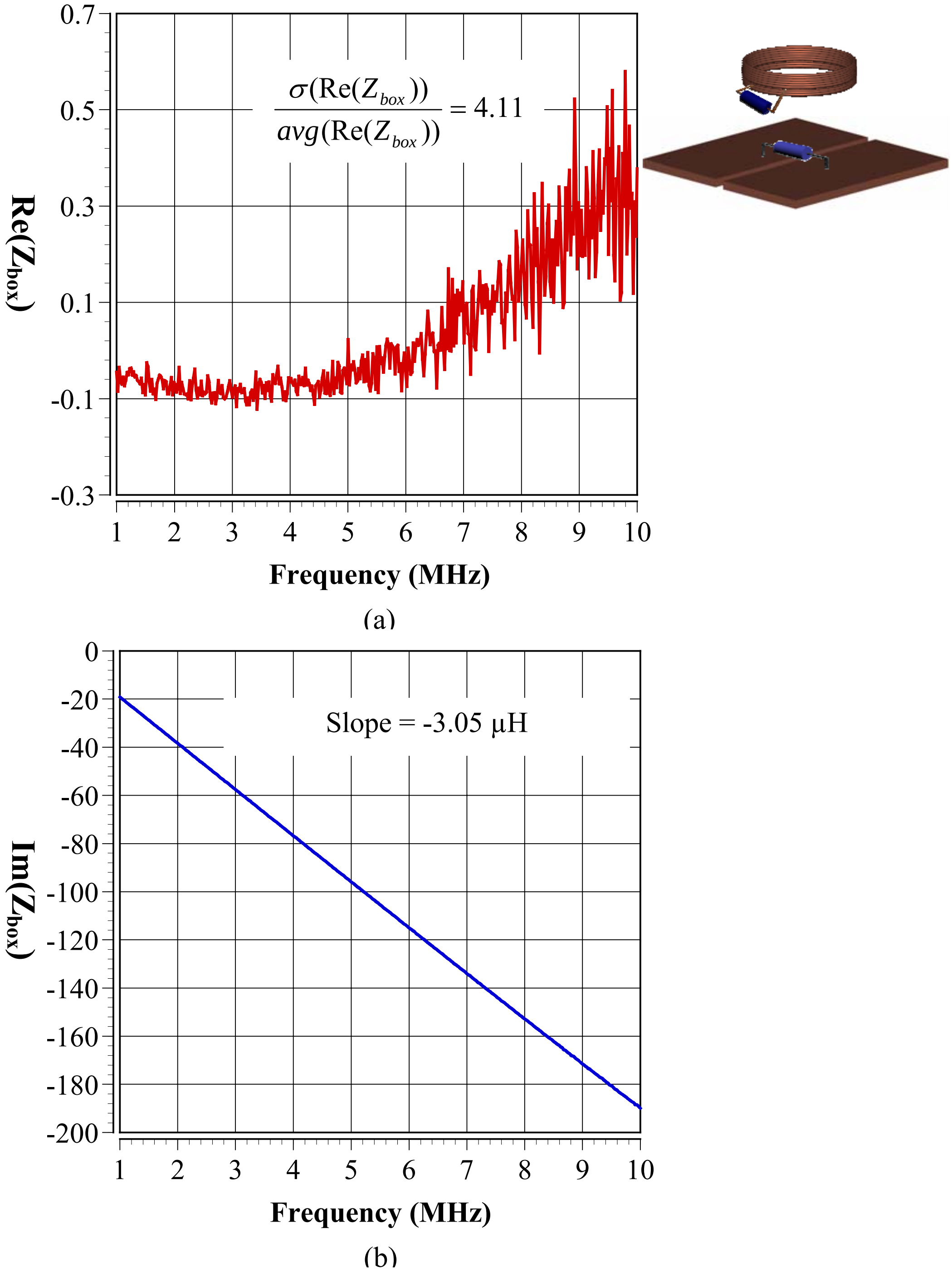

(a)

(b)

Figure 4.26: Z_{box} is computed for the system of the driver coil, the type III tag and the type V DUT. (a) The real part of Z_{box}. (b) The imaginary part of Z_{box}.

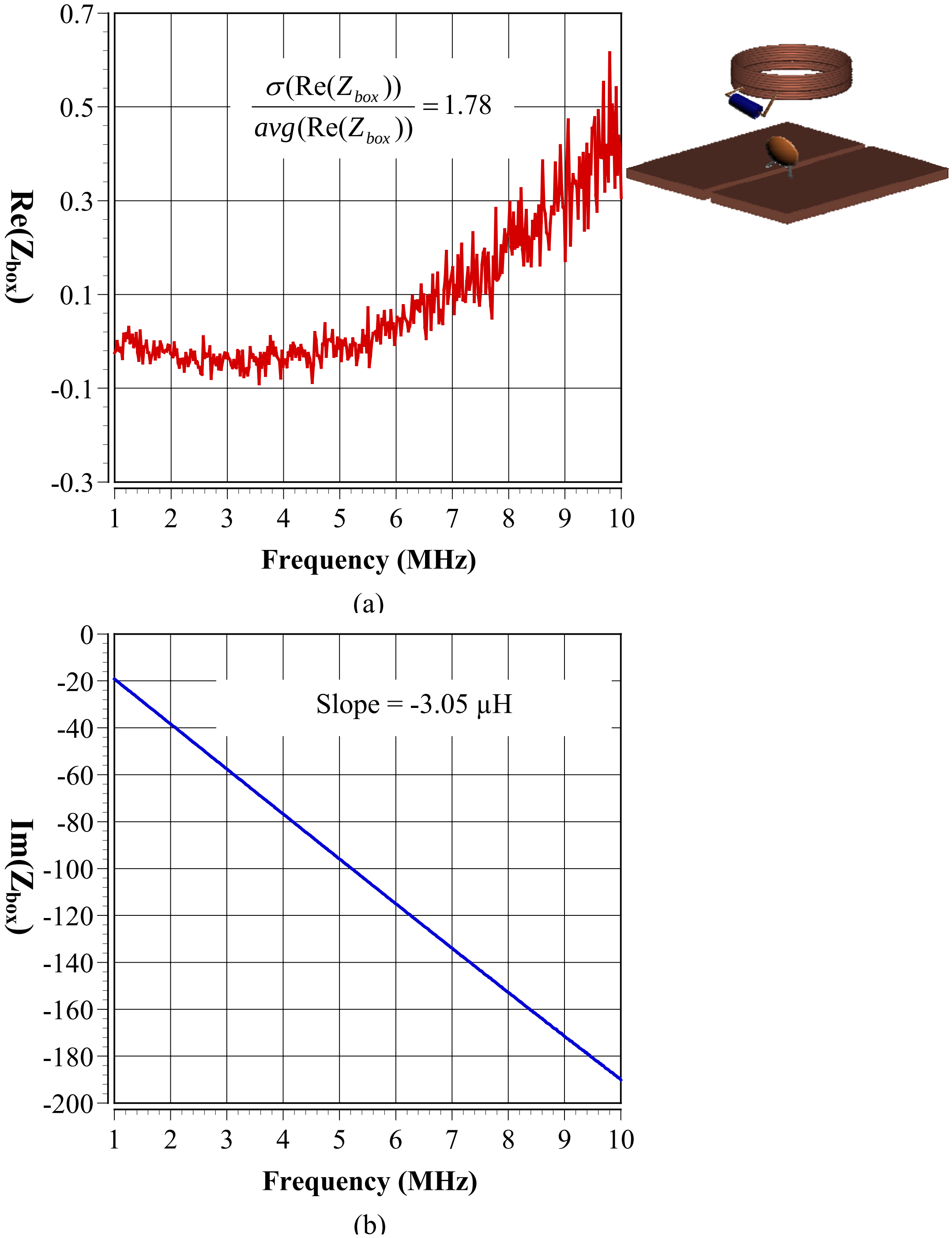

(a)

(b)

Figure 4.27: Z_{box} is computed for the system of the driver coil, the type III tag and the type VI DUT. (a) The real part of Z_{box}. (b) The imaginary part of Z_{box}.

4.2.3.4 Experiment with the system of the driver, the repeater tag(the type IV tag) and various types of DUT

In this section, the results are presented regarding the experiment done with the system of the driver and the repeater tag, and various types of DUT. The repeater tag is modeled as series resonant circuit as explained in the section 4.1.1. Therefore, Z_{lumped} can be expressed as the impedance of the capacitor, namely $\frac{1}{j\omega C_{capacitor}}$. The real and imaginary part of Z_{box} are presented in the Figure 4.28 through Figure 4.33.

Figure	Tag	DUT	$\mathrm{Re}(Z_{box})$	$\mathrm{Im}(Z_{box})$
4.28	Coil Loop + Capacitor (471 uF)	No Slit	1. Two sharp peak appear around inflection point (one is +0.8, the other is -1.2) 2. $\frac{\sigma(\mathrm{Re})}{avg(\mathrm{Re})}$ = -1.274945	1. Linearly dependent on frequency except for a certain range during which it looks like a camelback (Peak: 4.8 MHz) 2. Slope = -3.05 μH
4.29	Coil Loop + Capacitor (471 uF)	Slit	1. Two sharp peak appear around inflection point (one is +1.5, the other is -1.3) 2. $\frac{\sigma(\mathrm{Re})}{avg(\mathrm{Re})}$ = -1.84088	1. Linearly dependent on frequency except for a certain range during which it looks like a camelback (Peak: 4.6 MHz) 2. Slope = -3.06 μH
4.30	Coil Loop + Capacitor (471 uF)	Slit + Resistor (10 ohm)	1. Two sharp peak appear around inflection point (one is +1.4, the other is -1.2) 2. $\frac{\sigma(\mathrm{Re})}{avg(\mathrm{Re})}$ = -1.667899	1. Linearly dependent on frequency except for a certain range during which it looks like a camelback (Peak: 4.6 MHz) 2. Slope = -3.05 μH
4.31	Coil Loop + Capacitor (471 uF)	Slit + Resistor (10K ohm)	1. Two sharp peak appear around inflection point (one is +1.4, the other is -1.3) 2. $\frac{\sigma(\mathrm{Re})}{avg(\mathrm{Re})}$ = -1.601898	1. Linearly dependent on frequency except for a certain range during which it looks like a camelback (Peak: 4.6 MHz) 2. slope = -3.06 μH
4.32	Coil Loop + Capacitor (471 uF)	Slit + Inductor (3.9 uH)	1. Two sharp peak appear around inflection point (one is +1.5, the other is -1.3) 2. $\frac{\sigma(\mathrm{Re})}{avg(\mathrm{Re})}$ = -1.849779	1. Linearly dependent on frequency except for a certain range during which it looks like a camelback (Peak: 4.6 MHz) 2. Slope = -3.05 μH
4.33	Coil Loop + Capacitor (471 uF)	Slit + Capacitor (471 uF)	1. Two sharp peak appear around inflection point (one is +1.5, the other is -1.4) 2. $\frac{\sigma(\mathrm{Re})}{avg(\mathrm{Re})}$ = -1.829057	1.Linearly dependent on frequency except for a certain range during which it looks like a camelback (Peak: 4.6 MHz) 2. Slope = -3.05 μH

Table 4.4: Summary of the characteristics of the real and imaginary part of the Z_{box} in the plots from Figure 4.28 through Figure 4.33

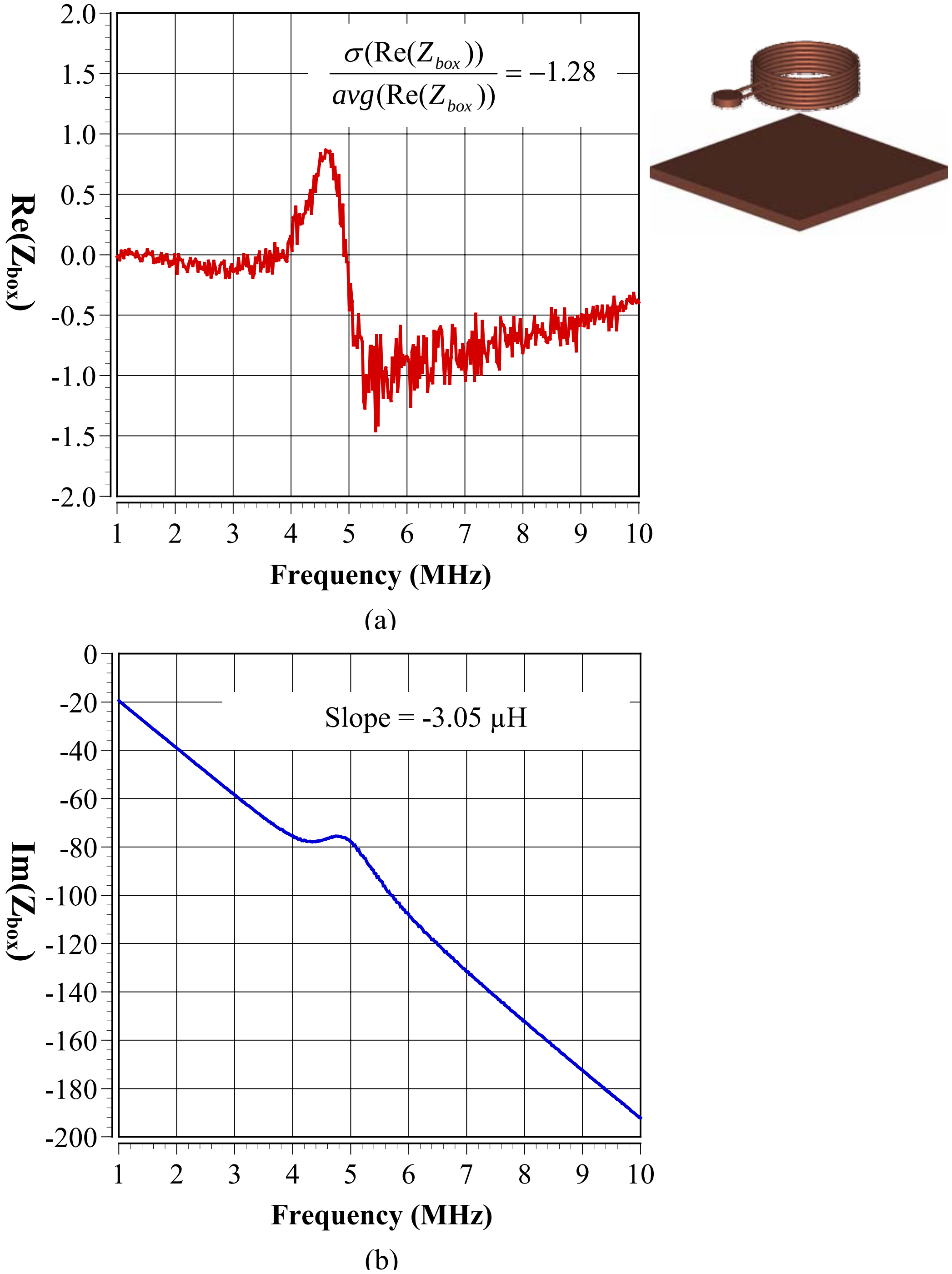

(a)

(b)

Figure 4.28: Z_{box} is computed for the system of the driver coil, the repeater tag and the type I DUT. (a) The real part of Z_{box}. (b) The imaginary part of Z_{box}.

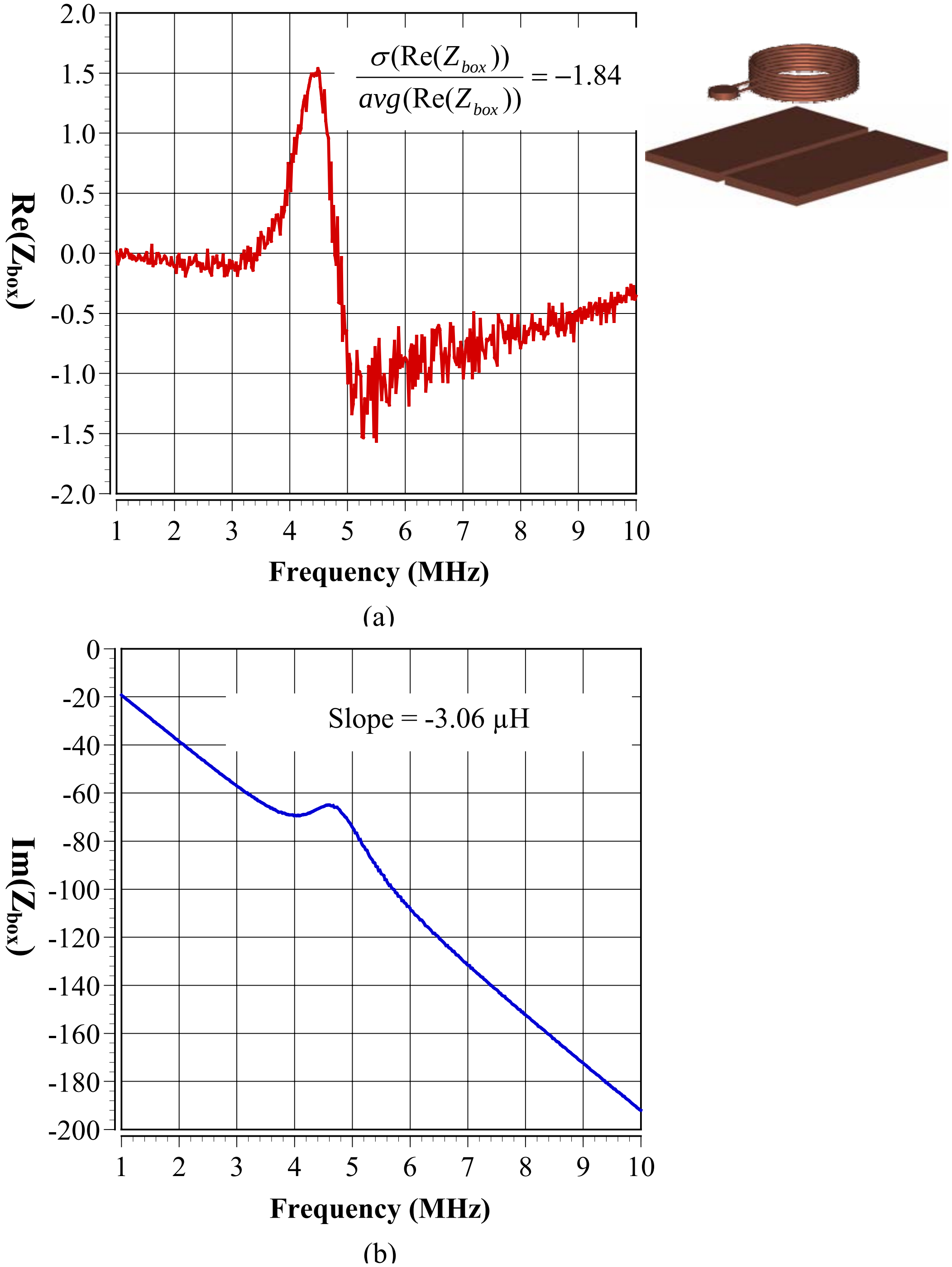

(a)

(b)

Figure 4.29: Z_{box} is computed for the system of the driver coil, the repeater tag and the type II DUT. (a) The real part of Z_{box}. (b) The imaginary part of Z_{box}.

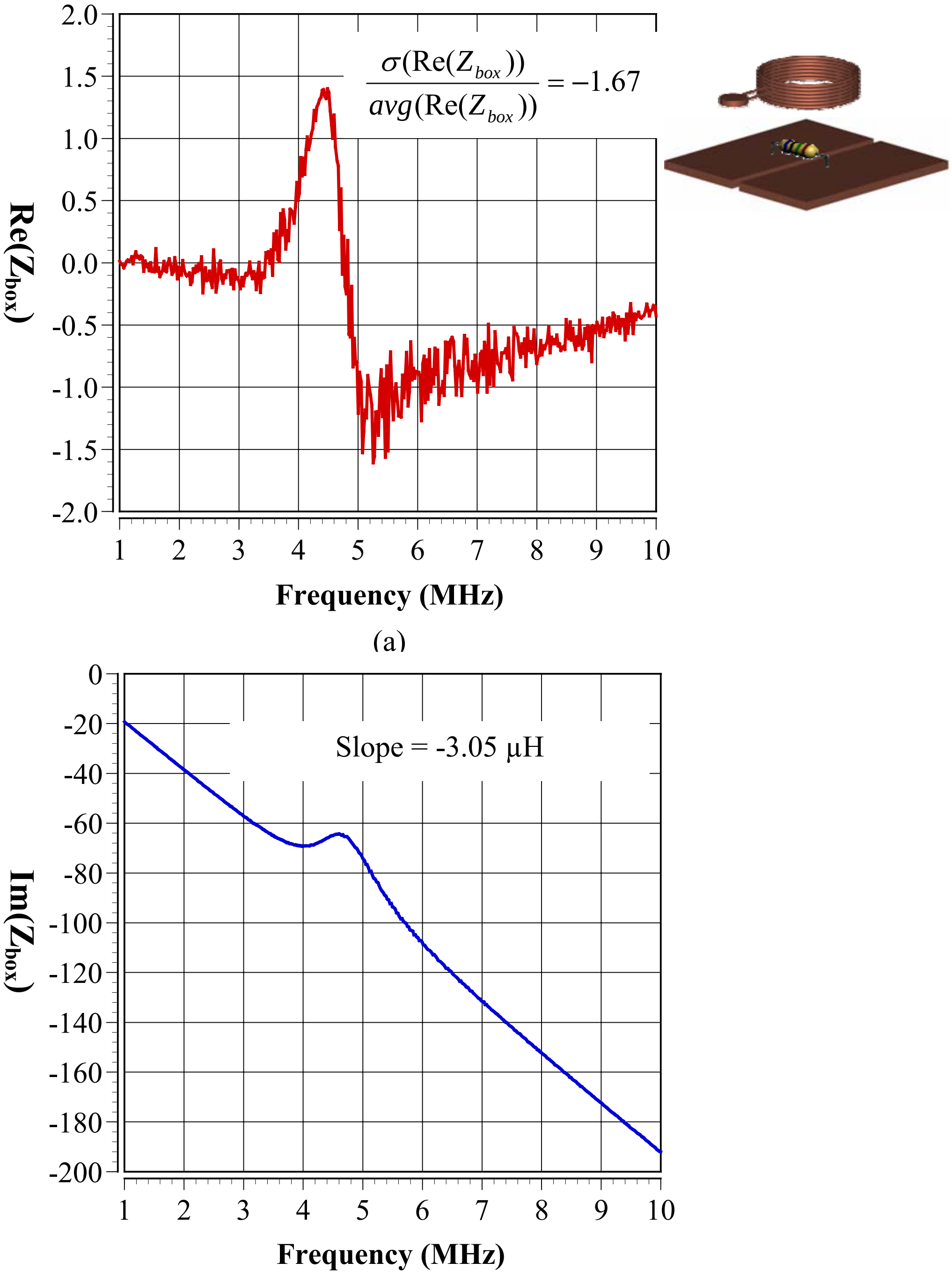

(a)

(b)

Figure 4.30: Z_{box} is computed for the system of the driver coil, the repeater tag and the type III DUT. (a) The real part of Z_{box}. (b) The imaginary part of Z_{box}.

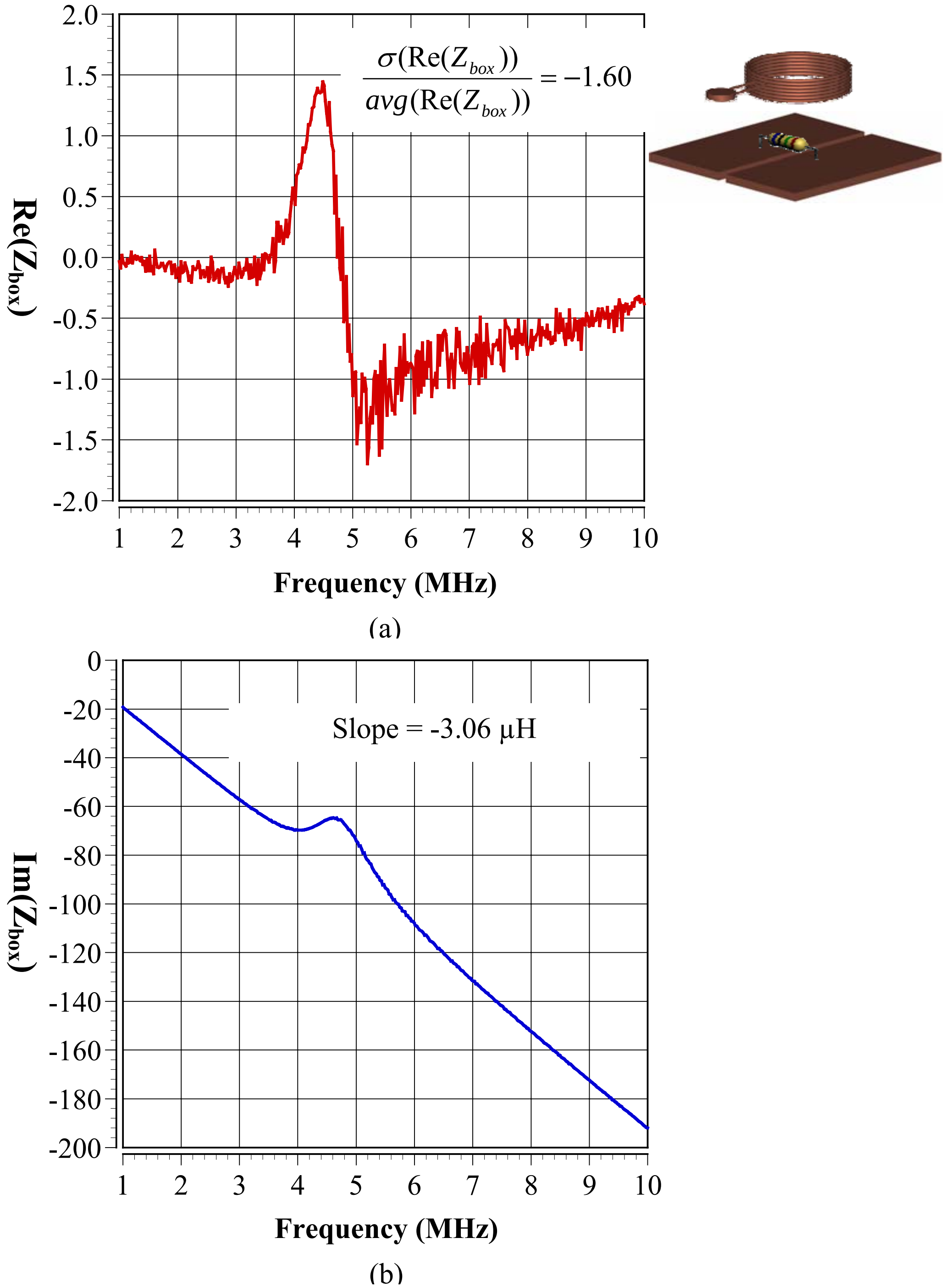

(a)

(b)

Figure 4.31: Z_{box} is computed for the system of the driver coil, the repeater tag and the type IV DUT. (a) The real part of Z_{box}. (b) The imaginary part of Z_{box}.

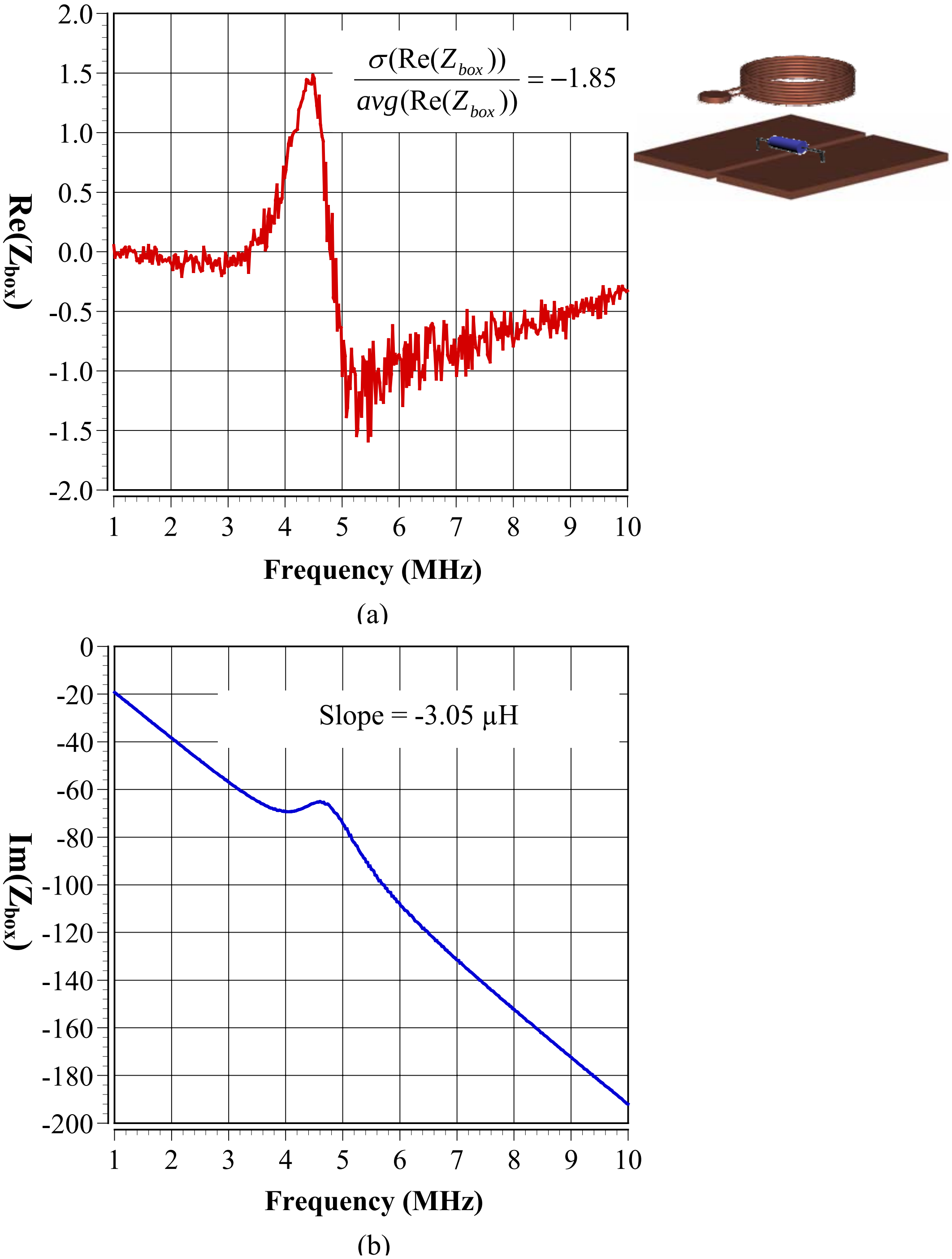

(a)

(b)

Figure 4.32: Z_{box} is computed for the system of the driver coil, the repeater tag and the type V DUT. (a) The real part of Z_{box}. (b) The imaginary part of Z_{box}.

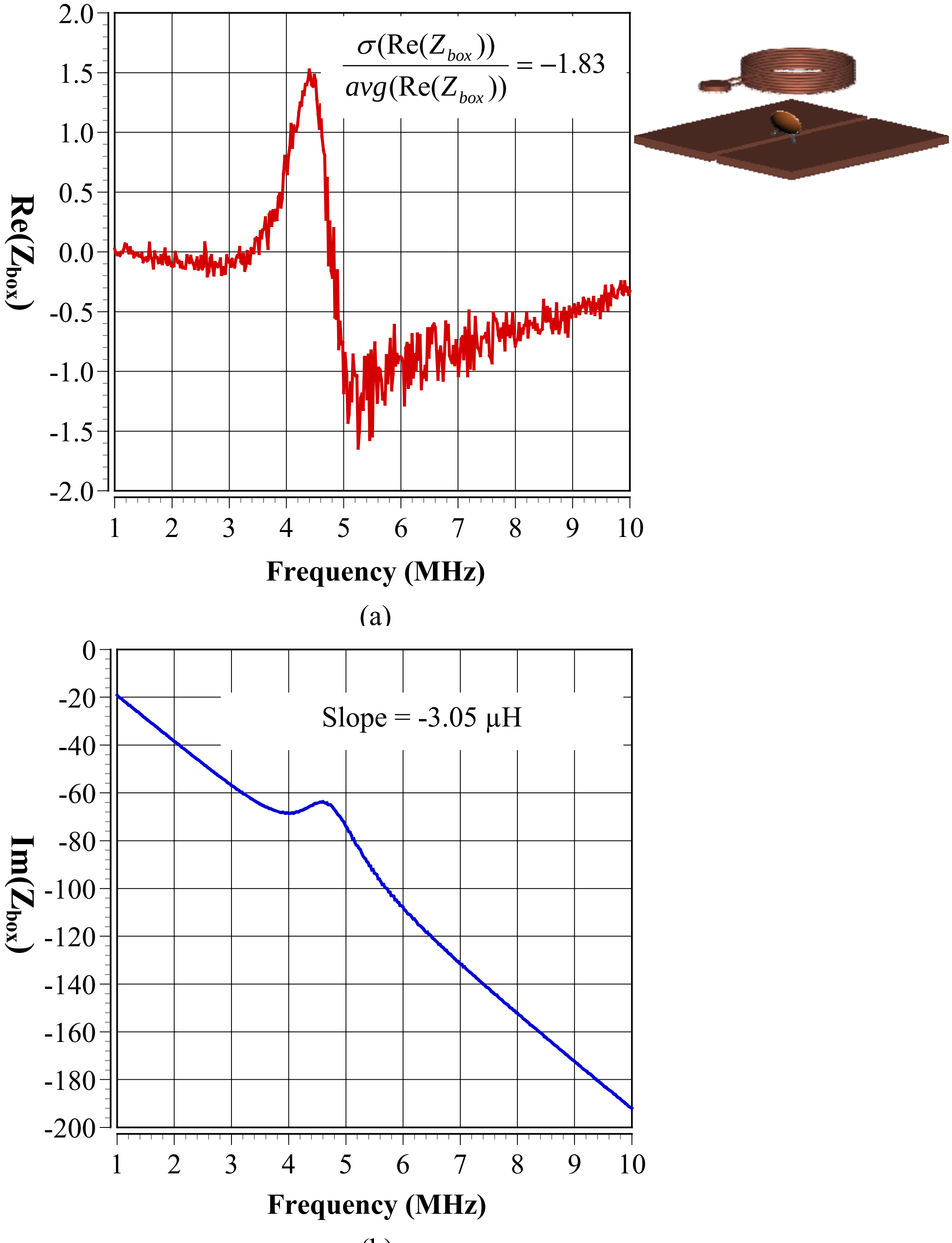

(a)

(b)

Figure 4.33: Z_{box} is computed for the system of the driver coil, the repeater tag and the type VI DUT. (a) The real part of Z_{box}. (b) The imaginary part of Z_{box}.

4.2.3.5 A short comment on the negative inductance of the imaginary part of Z_{box}

As observed in the plots in the experiment, the imaginary part of Z_{box} has a negative values and a linear dependency on the frequency. The resulting negative inductance of the imaginary part is almost the same as the inductance of the tag in magnitude. For example, the inductance of the type III tag was about 3.48 miro Henries(μH) and the resulting imaginary part had a slope of around 3.07 μH .

The mathematical equation (4.4) for the equivalent circuit enforces the voltage drop to be zero around a closed loop. As a result of this equation (4.4), the imaginary loop containing Z_{box} is also compelled to satisfy the condition. The only way to meet the conditions is to have an imaginary part, which is negative and linearly increasing in magnitude as the frequency increases as shown in the plots of previous sections. Consequently, the negative inductance of these experiments is the artifact of the mathematical requirement placed on the equivalent circuit modeling.

Chapter 5

Analysis of Experiment Data

In the previous chapter, effort to build equivalent circuits for the system has been made. However, the resulting equivalent circuits are similarly irrespective of the condition in the DUT since the artifacts forces the imaginary part of the Z_{box} to be a negative inductance which is almost the same magnitude of the inductor in the repeater tag. Even though the equivalent circuit modeling does not provide enough information on the health of the DUT, the impedance data, which are obtained from various experiments, are different depending on the conditions of the DUTs as already observed in Chapter 2. Thus, to exploit the variations of the impedance data further, a more systematic approach is devised based on the new measurements, which are used to determine the characteristics of the impedance data.

To explore how the system input impedance response changes according to variation of parameters, such as thickness of metallic DUT, gap between DUT and a repeater tag etc., additional experiments have been carried out and analyzed here.

5.1 THE FACTORS TO CHARACTERIZE THE RESPONSE OF THE SYSTEM

Since our purpose of experiments is to compare the responses due to different circumstances, the criteria to characterize each response have to be set beforehand. To explain what kinds of measure are used, a sample impedance response after calibration step, which is previously discussed in earlier chapter, is given in Figure 5.1. In the figure, the magnitude and phase of the impedance are plotted together. Since it is the phase plot that is important to determine the characteristics of the response, the magnified phase response near the resonant frequency is redrawn with the graphical description of important parameters used for definition of the factors.

The three measures that are employed to characterize the response from sets of experiment are effective resonant frequency, maximum phase dip, and pseudo quality factor. The significance of each factor will be explained next.

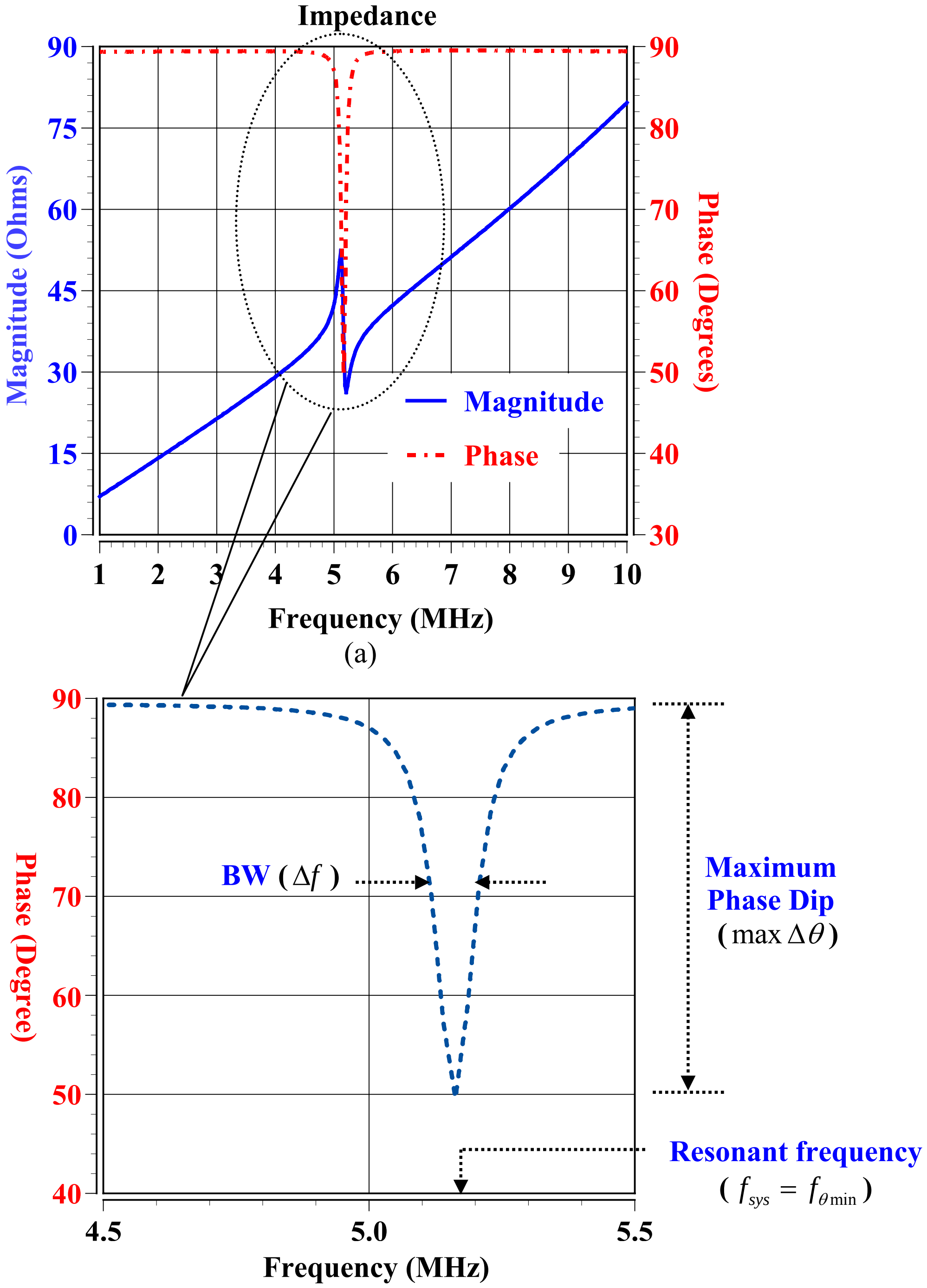
Impedance
Magnitude (Ohms)
0
15
30
45
60
75
90
Phase (Degrees)
30
40
50
60
70
80
90
1
2
3
4
5
6
7
8
9
10
Frequency (MHz)
Magnitude
Phase
Phase (Degree)
40
50
60
70
80
90
BW (Δf)
Maximum Phase Dip
(max Δθ)
Resonant frequency
(f_sys = f_θmin)
4.5
5.0
5.5
Frequency (MHz)

(a)

(b)

Figure 5.1: A sample impedance response after calibration. (a) The magnitude and phase response are plotted together. (b) The magnified phase response of impedance response from (a) with the graphical description of important parameters used for definition of the factors.

5.1.1 The effective resonant frequency

As explained in the introduction, our proposed scheme is to utilize a repeater tag to increase induced eddy current at certain frequency so that the sensitivity can be vastly improved to correctly determine the health (condition) of the metallic object which is being monitored. To achieve the purpose, a repeater is devised which can be equivalently modeled as a series *RLC* resonator depicted in Figure 5.2a.

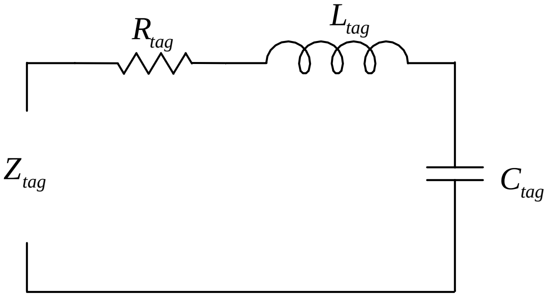

(a)

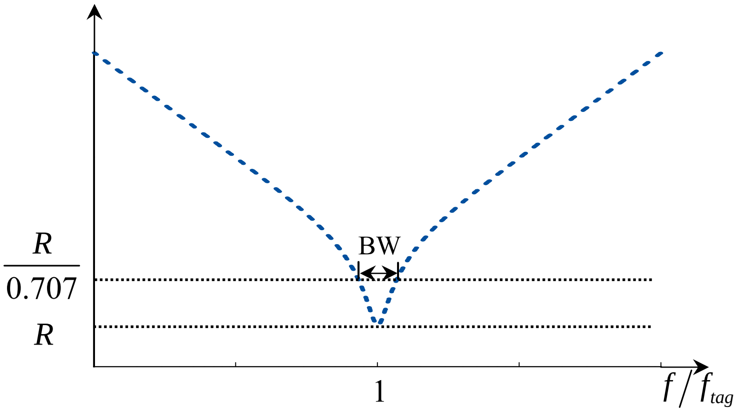

(b)

Figure 5.2: A series RLC resonator and its response (a) The series RLC circuit. (b) The input impedance magnitude versus frequency.

Resonance occurs in the repeater tag when the average stored magnetic and electric energies are equal. Then, the input impedance at resonance is

$$Z_{in} = R_{tag}, \tag{5.1}$$

which is a purely real impedance. From the fact the average stored magnetic and electric energies are equal, the resonant frequency of the tag, f_{tag}, must be defined as

$$f_{tag} = \frac{1}{2\pi\sqrt{L_{tag}C_{tag}}}. \tag{5.2}$$

Although the resonant frequency can be simply defined in a series *RLC* resonator, it is not easy to apply it to the proposed scheme without modification because a series *RLC* repeater tag is not working by itself but is only contributing to system input impedance as a component via magnetic coupling as explained in Chapter 1. Consequently, the input impedance magnitude of the system in Figure 5.2a is not similar to the input impedance magnitude of the repeater tag in Figure 5.2b when the repeater tag is embedded into the system as a component for improving sensitivity to detect the crack in the metallic DUT. Nonetheless, to exploit the resonance of a series *RLC* circuit to characterize the response of the system obtained from experiment, the input impedance phase of the system is made use of since it is very close to the input impedance magnitude of a series *RLC* resonator. As analogous to resonant frequency of a series *RLC* circuit defined at the minimum of input impedance magnitude, the effective resonant frequency is defined when the impedance phase of the system is minimum described in Figure 5.1b. Although it seems that two definitions are quite different from each other, the definition of effective resonant frequency is inherently the same as that of resonant frequency of a series *RLC* resonator because the effective inductance of a series *RLC* repeater in the system resonates with capacitor under the same condition just like a standalone series *RLC* resonator does. However, the resonance of a repeater tag contributes to system input impedance magnitude in a way that is different from the definition of resonant frequency as seen 5.1a. Thus, the system input impedance phase is used to define the effective resonant frequency as explained. The definition of the effective resonance can be defined as

$$f_{sys} = \frac{1}{2\pi\sqrt{L_{eff}C_{tag}}}, \tag{5.3}$$

where, L_{eff} is the effective inductance of the repeater tag when the interaction among the driver, the repeater tag, and a metallic DUT is taken into consideration. The effective inductance is the same as that of a repeater tag when there is no metallic DUT present under it. When a repeater tag is brought close to a metallic DUT, the effective inductance would be reduced due to induced eddy current. As a result of induce eddy current, the effective resonance of the system would be shifted to higher frequency than that of the repeater tag.

5.1.2 The maximum phase dip

Another factor to characterize the system response is the maximum dip of system input impedance phase as indicated in Figure 5.1b. Due to increased eddy current at the effective resonant frequency, the input impedance phase has changed dramatically to a lower value from 90° degree which is the characteristics of inductor. Thus, maximum change of the system impedance phase would be a good indicator to characterize the system response because the change depends on the condition of metallic DUT.

5.1.3 The pseudo Quality Factor (PseudoQ)

Another important parameter of a resonant circuit is its *Q*, or quality factor, which is defined as

$$Q = \omega \frac{\text{(average energy stored)}}{\text{(energy loss/second)}}. \tag{5.4}$$

Thus, *Q* is a measure of the loss of a resonant circuit - lower loss implies a higher *Q*. For the series resonant circuit of Figure 5.2a, the *Q* can be evaluated to give

$$Q = \frac{\omega_{tag} L_{tag}}{R_{tag}} = \frac{1}{\omega_{tag} R_{tag} C_{tag}}, \tag{5.5}$$

which shows that *Q* increases as *R* decreases.

In the case of an RLC series (or parallel) resonant circuit, the *Q* of the circuit can be defined using the half-power fractional bandwidth of the resonator as follow

$$Q = \frac{\omega_{tag}}{\Delta\omega}, \tag{5.6}$$

where $\Delta\omega$ is the half-power bandwidth of the resonator.

Figure 5.2b shows the variation of the magnitude of the input impedance versus frequency. When the frequency is such that $\left|Z_{tag}\right| = 2R_{tag}^2$, then the average (real) power delivered to the circuit is one-half that delivered at resonance. Then, using the description in the Figure 5.2b gives

$$Q = \frac{\omega_{tag}}{\mathrm{BW}}, \tag{5.7}$$

for the repeater tag.

As what was done to define the effective resonant frequency, the definition of Q can be applied to the system input impedance phase in Figure 5.2b with a little modification. A new measure is proposed which is the ratio of the frequency at the minimum impedance phase (resonant frequency) to the width of the impedance phase curve around resonant frequency. This ratio is referred to as the pseudo-Quality factor or pseudo*Q*:

$$pseudoQ \equiv \frac{f_{\theta\min}}{\Delta f}. \tag{5.8}$$

The width is defined as the full-width half-max (FWHM) of the system input impedance phase curve. The values of Δf and $f_{\theta\min}$ are shown in Figure 5.1b. This value is referred to as the pseudo*Q* in order to differentiate it from the actual *Q* of the entire magnetically coupled circuit as it is related to energy stored and energy dissipated.

5.2 THE RESPONSE OF THE SYSTEM IN VARIOUS PARAMETERS

Based on the factors defined in previous section, the system input impedance curves in various conditions are analyzed and presented in this section.

5.2.1 The thickness of metallic DUT

To see what is the effect of the thickness of metal DUT on the system response, experiments are carried out. The simplified setup is illustrated in Figure 5.3.

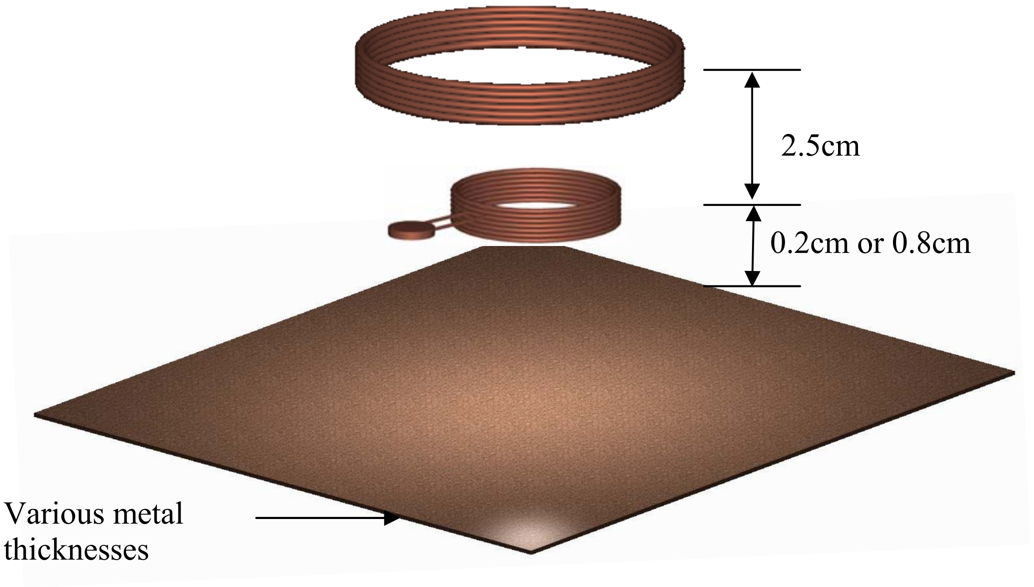

Figure 5.3: Illustration of setup to find out the effect of metal thickness on the system input impedance. The drawings are not to scale.

The results of the experiment are presented in Figure 5.4. The metal plates used as DUT are made of alloy 110 (Electrolytic Tough Pitch Copper) which has conductivity about 101% of pure copper.

The resonant frequency was 2.64 MHz when no metal plate is present under a repeater tag. However, when the copper DUT is placed under the repeater tag, the effective resonance is moved into higher frequency as can be seen in Figure 5.4a since the induced eddy current in the copper plate leads to the reduction of the effective inductance of the repeater tag. The discrepancy between resonant frequencies is due to the difference in the amount of eddy current induced in metal plate because the mutual inductance depends strongly on the distance between the repeater tag and metal plate. When the repeater is brought closer to the metal plate, it interacts more strongly with the induced eddy current, which leads to more reduction of effective inductance of repeater tag. Thus, the resonant frequency is shifted to higher frequency according to (5-3) when the repeater tag is closer to the metal plate. A little fluctuation in the effective resonant frequency versus copper thickness curve is assumed to be result of the unevenness of the surface of the copper metal plate. From the resonant frequency curve, it can be said that the thickness of the copper does not have a strong influence on the system input impedance.

The maximum phase dip is much larger when the distance between the repeater tag and the metal plate are farther away. The repeater tag does not disturb current in the driver as much since the magnetic flux density of the repeater loop is reduced considerably by the induced eddy current in the metal plate when the repeater tag is closer to the metal plate. On the contrary, the magnetic flux density of repeater loop changes inductive characteristic of driver loop at resonant frequency when the gap between the repeater and the metal plate gets bigger as can be seen the curve in Figure

5.4b. It was 68 degree phase dip when there is no metal plate present under the repeater tag.

The PseudoQ is also larger when the distance between the repeater tag and the metal plate are farther away. For the reference, pseudoQ was 116 without any metal plate under the repeater tag.

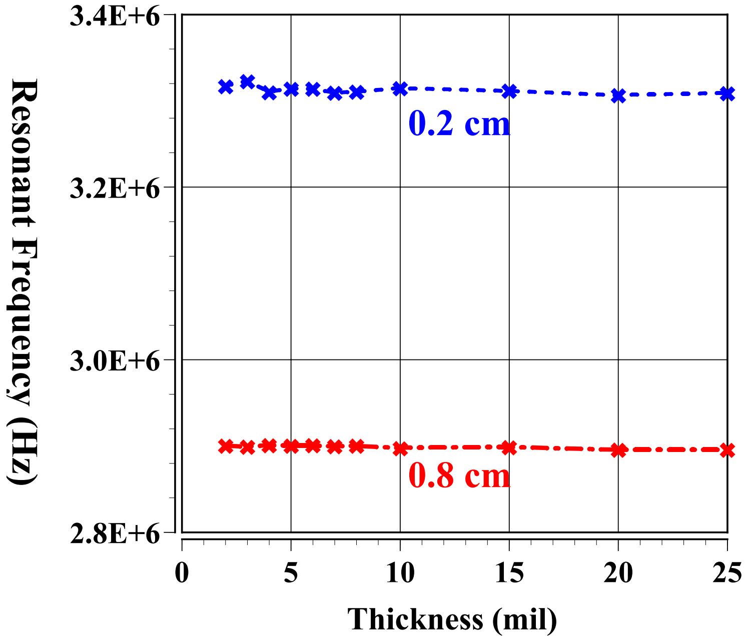
3.4E+6
3.2E+6
3.0E+6
2.8E+6
Resonant Frequency (Hz)
0.2 cm
0.8 cm
0
5
10
15
20
25
Thickness (mil)

(a)

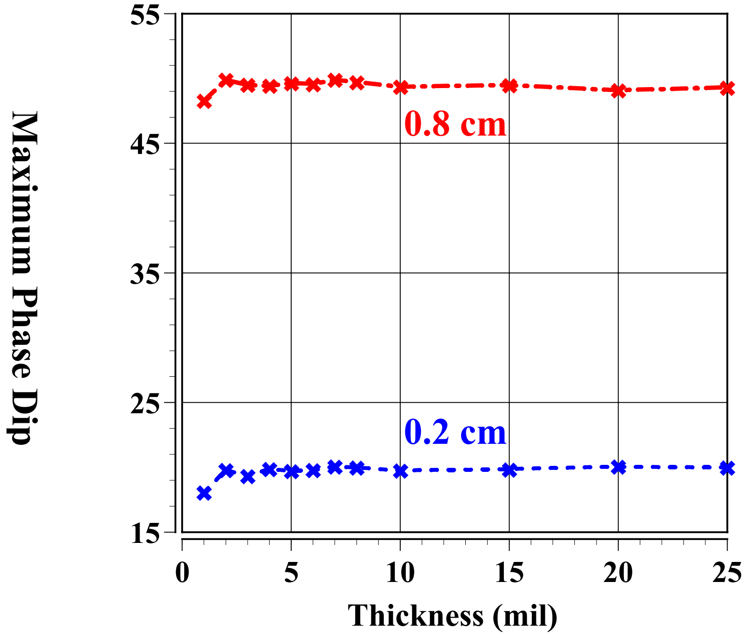
55
45
35
25
15
Maximum Phase Dip
0.8 cm
0.2 cm
0
5
10
15
20
25
Thickness (mil)

(b)

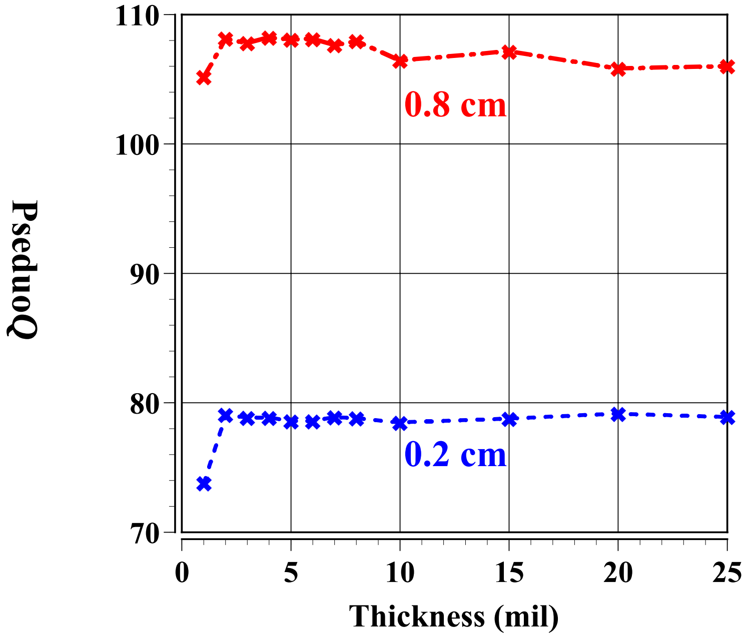

(c)

Figure 5.4: The result of experiment. The purpose of experiment is to find out what the effect of copper thickness is on the factors defined in previous section. (a) The Effective resonant frequency. (b) The maximum phase dip. (c) The pseudo*Q*.

5.2.2 The gap between DUT and repeater

Next experiment is to see the effect of the gap between the repeater tag and metal plate on the characteristics of the system response. The gap between the repeater tag and metallic DUT was set at 0.2cm, 0.3cm, 0.4cm, or 0.5cm. For each gap, two different conditions of the metal plates were used, one of which has no slit and the other has a slit as Figure 5.5.

Whether the metallic DUT has slit or not, the resonant frequency is highest when the gap between the repeater tag and DUT is smallest as can be noticed in Figure 5.6a. However, the effect due to the induced eddy current is less when there is a slit in the metal plate since the slit hinders the induced eddy current from circulating on the metal plate.

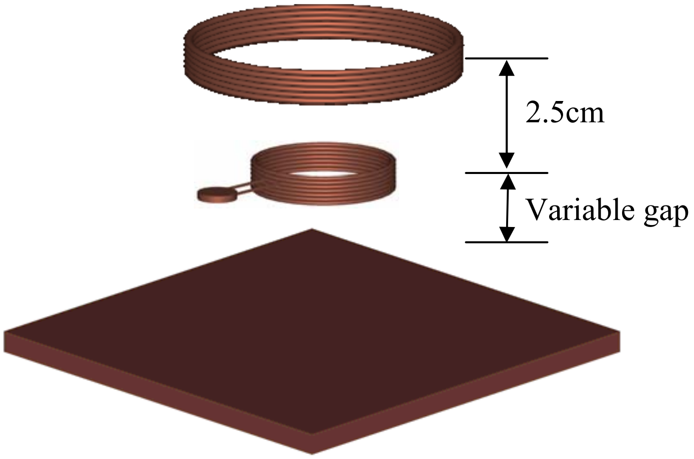

(a)

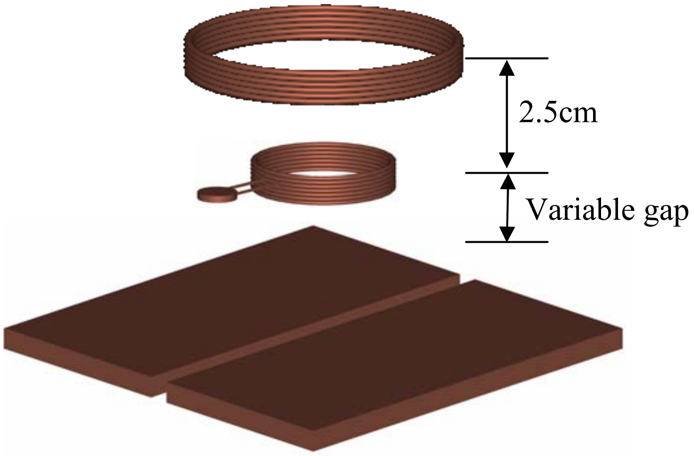

(b)

Figure 5.5: Illustration of setup to see the effect of the gap between the repeater tag and metal plate on the characteristics of the system response. The drawings are not to scale. (a) The copper plate without slit is used as DUT. (b) The copper plate with a slit is used as DUT.

As the gap gets smaller, the interaction between the repeater and the metallic DUT becomes weaker so that the shift of resonant frequency is less significant from the case when there is no metal object under the repeater. On the contrary, the maximum phase dip seems to increase linearly as the gap becomes bigger. The growing maximum dip is attributed to the increased disturbance to the driver by the repeater tag. As explained in the previous section, the reduced interaction between the repeater and the induced eddy current contributes to the increased disturbance to the driver by the repeater tag as the gap gets bigger. The pseudoQ also shows a linear dependency on the gap between the repeater tag and the metallic DUT in Figure 5.6c.

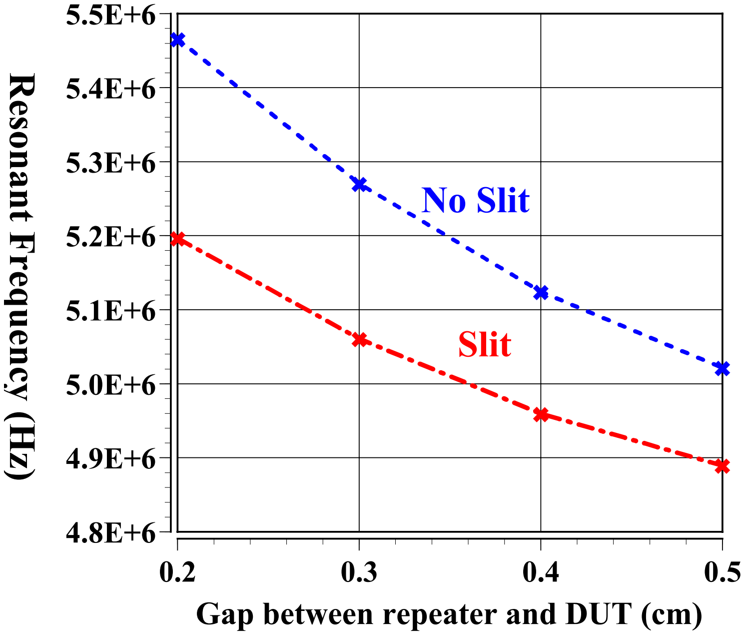

(a)

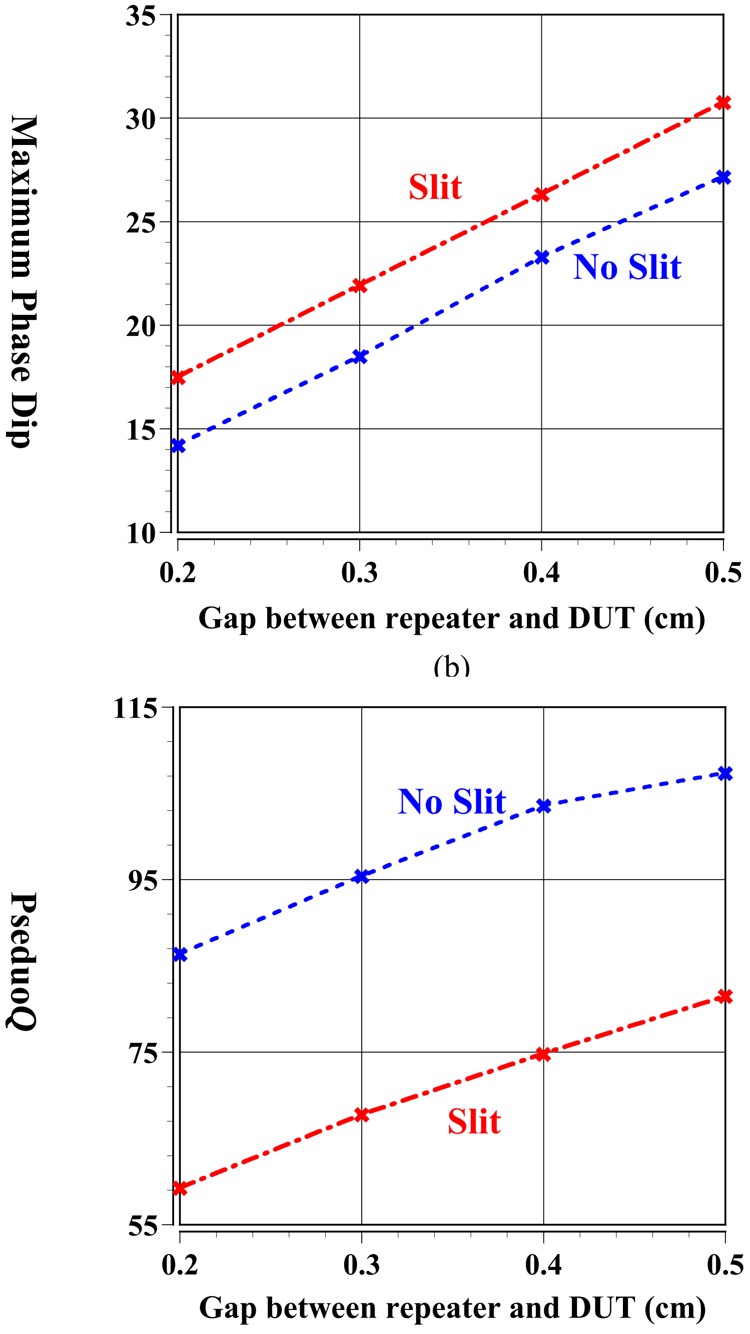

(b)

(c)

Figure 5.6: The result of experiment. The purpose of experiment is to find out what the effect of gap between the repeater tag and the DUT is on the factors defined in previous section. (a) The Effective resonant frequency. (b) The maximum phase dip. (c) The pseudo*Q*.

5.2.3 The gap between driver and repeater

To see if there is any impact on the previously defined factors due to gap between the driver and the repeater tag, another experiment has been carried out as illustrated in Figure 5.7. For each fixed gap between the driver and the repeater tag, the measurement has been taken at four different gaps, such as 0.2cm, 0.3cm, 0.4cm, and 0.5cm, between the repeater tag and the metallic DUT. The results are given in Figure 5.8.

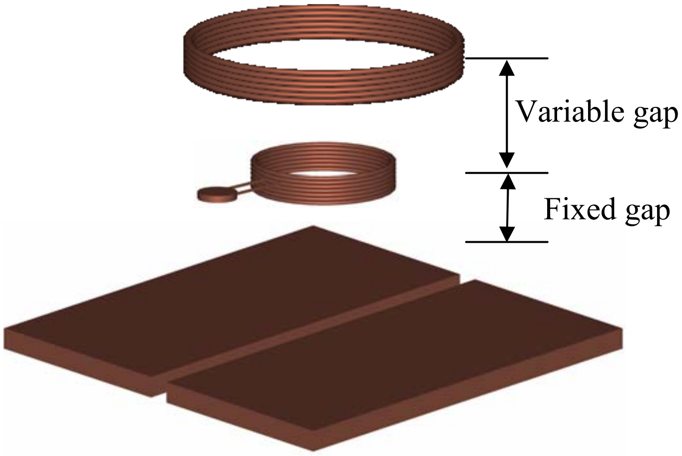

Figure 5.7: Illustration of setup to see the effect of the gap between the driver and the repeater tag on the characteristics of the system response. The drawings are not to scale.

It is very interesting that the resonant frequency does not depend on the gap between the driver and the repeater tag as noticed in the Figure 5.8a. From this, it can be deduced that the gap between the repeater tag and the metallic DUT determines the effective inductance of the repeater tag. At 2cm gap between the driver and the repeater tag, the maximum phase dip is affected by the gap between the repeater tag and the metallic DUT. However, the values of the maximum phase dip converse almost at the same point when the gap becomes 5cm as can be seen in Figure 5.8b. The pseudoQ does not seem to be very dependent on the gap between the driver and the repeater tag.

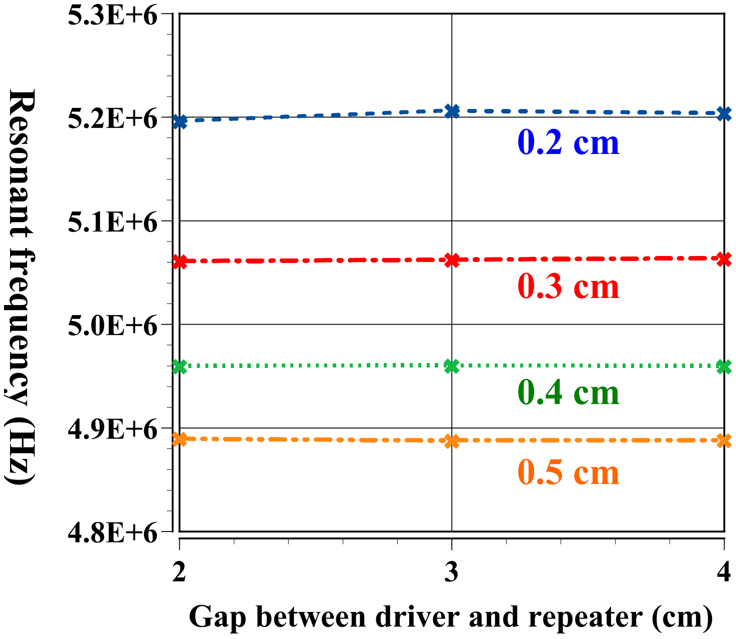

(a)

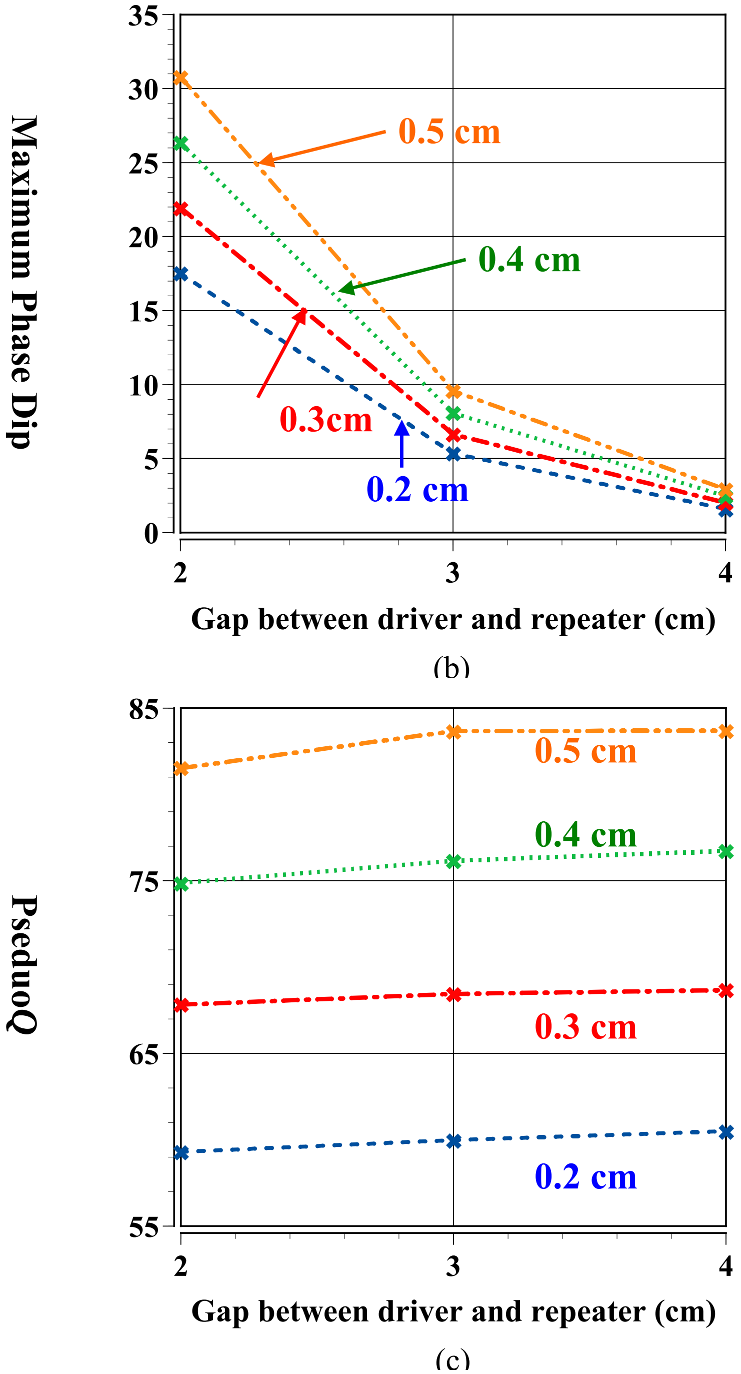

(b)

(c)

Figure 5.8: The result of experiment. The purpose of experiment is to find out what the effect of gap between the driver and the repeater tag is on the factors defined in previous section. (a) The Effective resonant frequency. (b) The maximum phase dip. (c) The pseudo*Q*.

5.2.4 The slit length

To see how the slit length impacts the characteristic of the system response, new experiment has been conducted as illustrated in Figure 5.9. After each measurement, the slit length is increased by 2mm from the center of the repeater tag to each direction. The results are plotted in terms of normalized slit length which is the slit length from center to one end of slit divided by the radius.

The resonant frequency changes slightly when the normalized slit length is smaller than 1. However, the resonant frequency drastically declines when the normalized slit length is increased from 1 to 3. If the normalized slit length is over 3, the slope of resonant frequency curve becomes less steep. Eventually, the resonant frequency settles down to a constant number if the slit length is much longer than the radius of the repeater tag.

The maximum phase dip is about 12° when there is no slit at all in the metal plate. However, it reduces to 8° when the slit length is shorter than the radius of the repeater tag. If the slit is made longer than the radius of the repeater tag, the maximum phase dip increases in proportional to the normalized slit length, but the slope of the curve slowly rolls down as the normalized slit length increases.

The pseudoQ of this experiment shows similar transition as the maximum phase dip while the slit length is shorter than the radius of the repeater tag. As the slit length increases further, the pseudoQ seems to level off at a constant number.

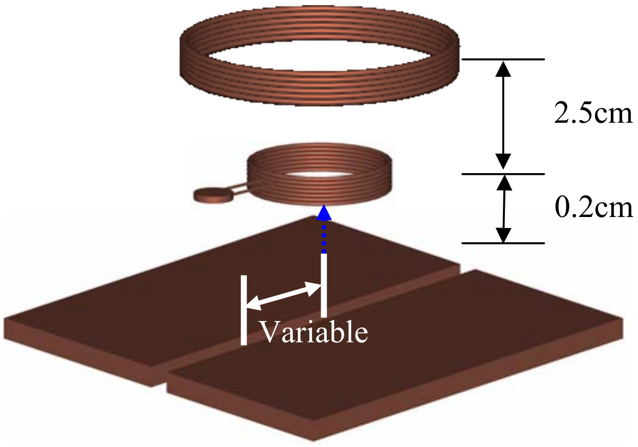

Figure 5.9: Illustration of setup to see how the slit length impacts on the characteristic of the system response. The drawings are not to scale.

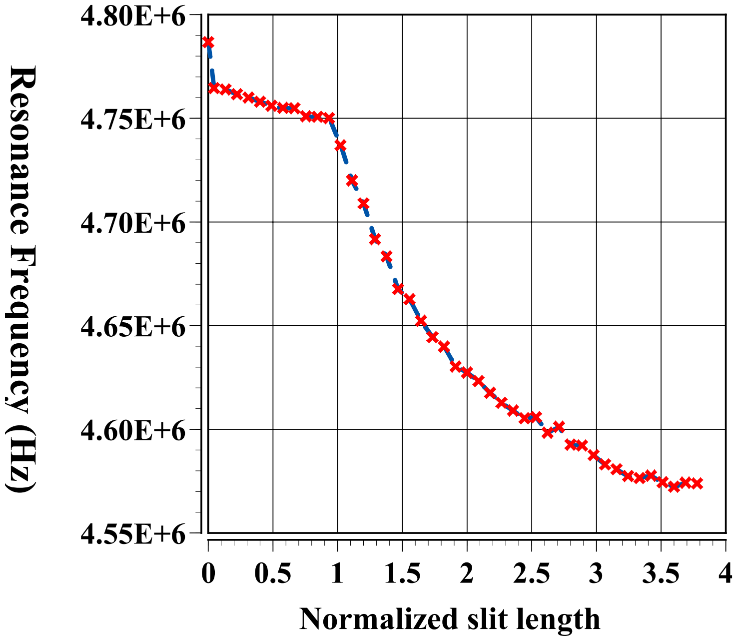
Resonance Frequency (Hz)
4.80E+6
4.75E+6
4.70E+6
4.65E+6
4.60E+6
4.55E+6
0
0.5
1
1.5
2
2.5
3
3.5
4
Normalized slit length

(a)

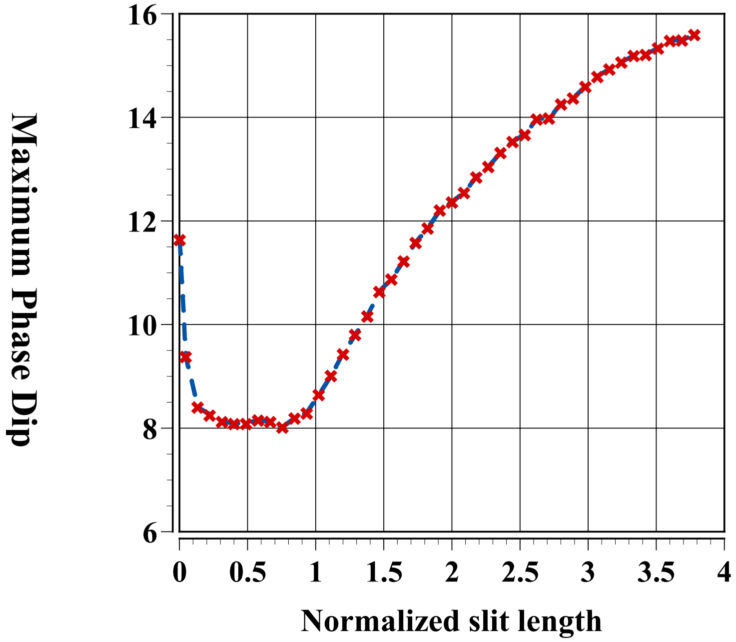
Maximum Phase Dip
16
14
12
10
8
6
0
0.5
1
1.5
2
2.5
3
3.5
4
Normalized slit length

(b)

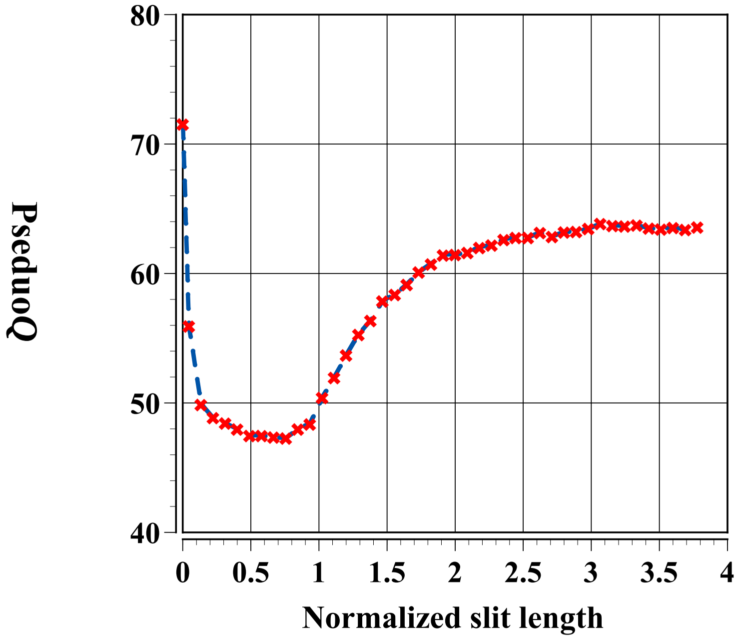

(c)

Figure 5.10: The results of experiment in which the slit length is varied to see how it impacts on the characteristic of the system response. The results are plotted in terms of normalized slit length which is the slit length from center to one end of slit divided by the radius. (a) The Effective resonant frequency. (b) The maximum phase dip. (c) The pseudo*Q*.

5.3 REVISITING THE EXPERIMENT DATA

The system responses have been analyzed based on the factors described in earlier section of this chapter. Although those analyses give some insight into the response, it is necessary to have a better understanding on how the system response is affected by the variation of parameters such as the DUT material thickness, the geometrical gap, or the slit length. Thus, new measurands were devised to evaluate the dependence of the effective inductance and loss on the variation of parameters.

5.3.1 The normalized effective inductance and resistance [43]

The effective inductance can be derived from (5.3) as

$$L_{eff} = \frac{1}{\left(2\pi f_{sys}\right)^2 C_{tag}} . \tag{5.9}$$

If two or more effective inductances are known from the experiment for which everything is the same except for one parameter like the DUT material thickness or the gap between the driver and the repeater tag, one of them can be used as a norm to estimate the others in relative perspective. For example, if L_{eff1} and L_{eff2} are two effective inductances from experiment, then the normalized effective inductance of L_{eff2} with respect to L_{eff1} can be calculated by dividing L_{eff2} by L_{eff1}:

$$\frac{L_{eff2}}{L_{eff1}} = \frac{\dfrac{1}{\left(2\pi f_{sys2}\right)^2 C_{tag}}}{\dfrac{1}{\left(2\pi f_{sys1}\right)^2 C_{tag}}} = \left(\frac{f_{sys1}}{f_{sys2}}\right)^2 . \tag{5.10}$$

Thus, the normalized effective inductance is dimensionless and can be defined as a ratio of the effective inductance to a selected effective inductance as the normalizing constant. The normalized effective inductance is meaningful only when the ratio of the effective inductances, obtained under the condition in which only one parameter is varied and the other parameters are fixed, is calculated.

The resistance of the repeater tag can be evaluated from (5.5) if the quality factor of the repeater tag is known:

$$R_{tag} = \frac{\omega_{tag} L_{tag}}{Q} . \tag{5.11}$$

However, the system impedance response needs to be investigated, not the resistance of the repeater tag. Besides, it is the pseudoQ that can be determined from the measurement. Thus, an assumption was made to utilize (5.11) for analysis of the system response in a way that the effective resistance of system has same form as the resistance of the repeater tag given in (5.11):

$$R_{eff} = \frac{\omega_{sys} L_{eff}}{pseudoQ}. \tag{5.12}$$

The usefulness of the effective resistance is not to assess the exact resistance of the system but to estimate how the loss is affected by the parameters from given experimental data. Therefore, the normalized effective resistance can be defined in similar fashion as the normalized effective inductance found in (5.10) if two effective resistance, $R_{eff\,1}$ and $R_{eff\,2}$, are given:

$$\frac{R_{eff\,2}}{R_{eff\,1}} = \frac{\dfrac{\left(2\pi f_{sys2}\right) L_{eff\,2}}{pseudoQ_2}}{\dfrac{\left(2\pi f_{sys1}\right) L_{eff\,1}}{pseudoQ_1}} = \frac{f_{sys2}}{f_{sys1}} \left(\frac{f_{sys1}}{f_{sys2}} \right)^2 \frac{pseudoQ_1}{pseudoQ_2} = \frac{f_{sys1}}{f_{sys2}} \frac{pseudoQ_1}{pseudoQ_2}. \tag{5.13}$$

The normalized effective resistance is also dimensionless and meaningful under the condition described earlier for the normalized effective inductance.

5.3.2 The thickness of the metallic DUT

The experiment data are analyzed to determine the resonant frequency, the maximum phase dip and the pseudoQ in section 5.2.1. Those data are collected by using the thickness of the metallic DUT as a parameter. The same experiment data were plotted in terms of normalized quantities defined previously in Figure 5.11.

For Figure 5.11a, the normalizing constant is the effective inductance when the DUT is 1mil thick copper metal plate. The normalized effective inductances lie within 2% of the normalizing value for 0.2cm of gap between the repeater tag and the DUT. As the gap is increased to 0.8cm, the variation is even less than 0.25% from the normalizing constant. That is because the induced eddy current is almost the same as the thickness of the copper plate varies. Hence, it can be inferred that the thickness of metallic DUT hardly has any influence on the distribution of the induced current in the metallic DUT.

The normalized effective resistance curve is plotted in Figure 5.11b. It also does not change very much from normalizing constant. The effective resistance is reduced when the thickness of metal plate was increase from 1mil to 2mil. The reason is that 1mil is less than the skin depth at the effective resonant frequency so that the loss would be more for such a case. However, if the metal plates are thicker than 2mil, the thickness is greater than the skip depth. Thus, the loss would not change much even if the thickness is increased further. The fluctuation in the effective resistance seems to be due to error in the measurement.

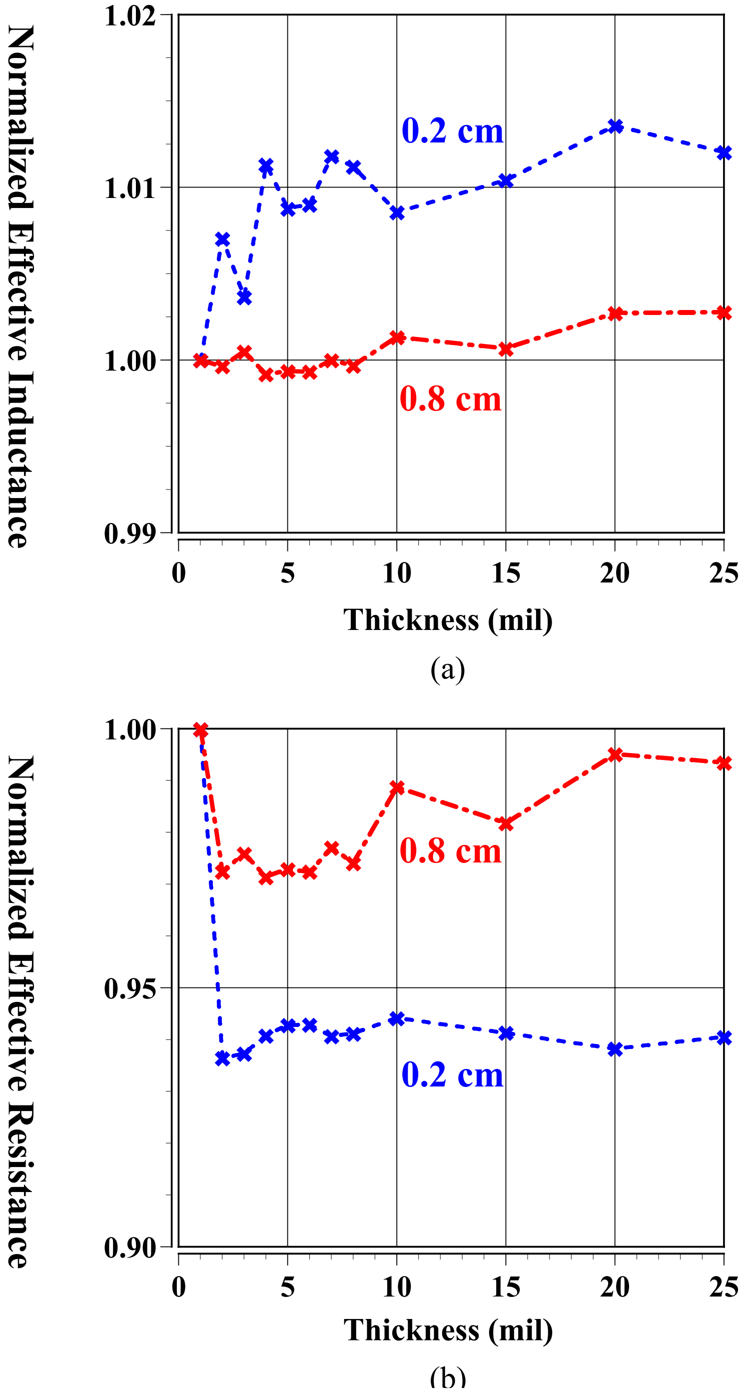

(a)

(b)

Figure 5.11: The normalized quantities derived from the same experiment data that are used to determine the resonant frequency, the maximum phase dip and the pseudoQ in section 5.2.1. (a) The normalized effective inductance. (b) The normalized effective resistance.

5.3.3 The Gap between the DUT and the repeater tag

In Figure 5.12, the normalized effective inductance and resistance are computed using (5.10) and (5.13). The normalizing constants are the effective inductance and resistance when the gap between the DUT and the repeater is 0.2cm.

Whether there is a slit or no slit in the copper metal plate, the normalized effective inductances increase as the gap is widen as can be seen in Figure 5.12a. However, the change is bigger without a slit in the metal plate. Since the current distribution is already disturbed much by the slit, the dependency of the normalized effective inductance on the gap is weakened. On the contrary, the current distribution is only affected by the gap when there is no slit. That is why the normalized effective inductance without a slit is influenced more than with a slit in the DUT.

The normalized effective resistances are reduced as the gap between the DUT and the repeater tag increases. Since the normalized effective resistance is related to the loss due to the induced eddy current in the metallic DUT, it can be concluded that the loss depends on how strong the current is induced by the repeater tag in the metallic DUT. It seems that the normalized effective resistance is affected more by the slit when there is a slit in the copper plate according to the curve in Figure 5.12b. From this observation, it can be inferred that how strongly the repeater tag interacts with the induced eddy current is a crucial factor that contributes to the normalized effective resistance. Another important factor for the normalized effective resistance is the path that the induced eddy current flows along.

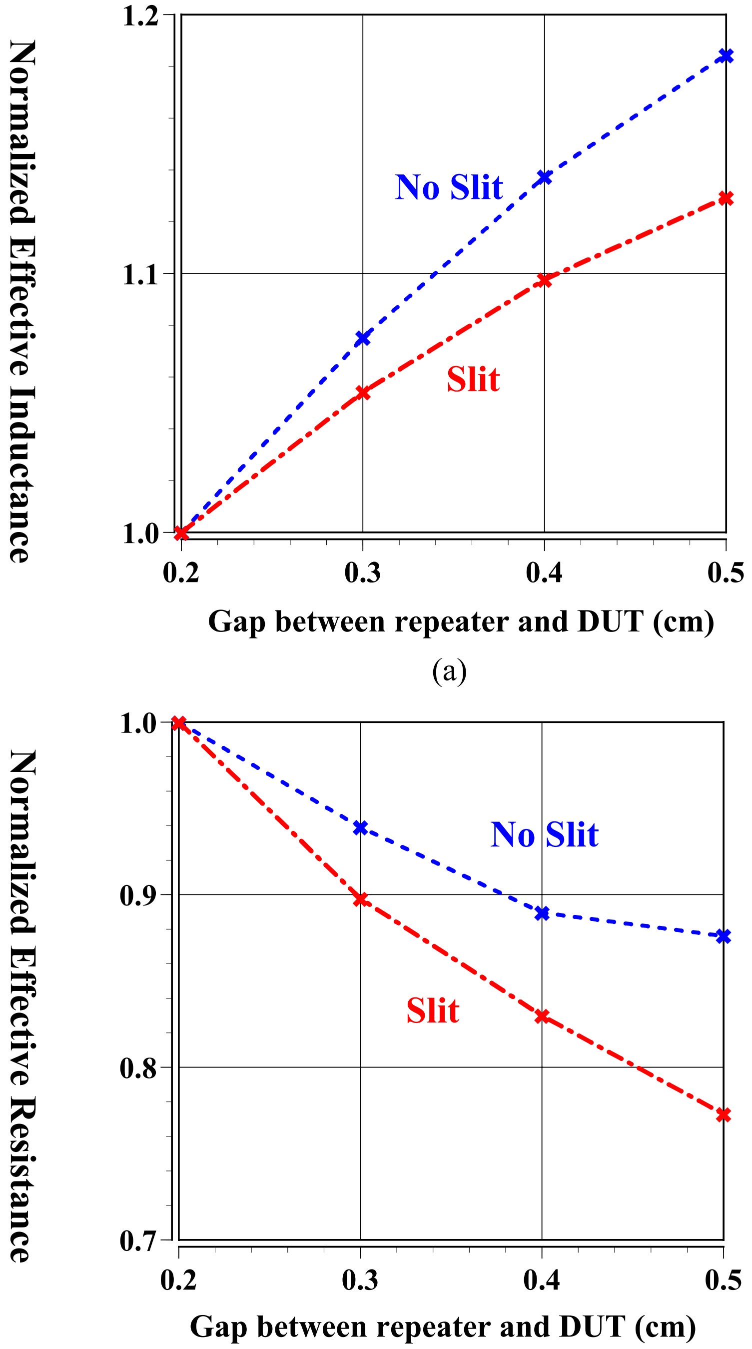

(a)

(b)

Figure 5.12: The normalized quantities derived from the same experiment data that are used to determine the resonant frequency, the maximum phase dip and the pseudoQ in section 5.2.2. (a) The normalized effective inductance. (b) The normalized effective resistance.

5.3.4 The Gap between the driver and the repeater tag

As seen in the section 5.2.3, the gap between the driver and the repeater does not have significant influence on the characteristic of the system response. Thus, it can be expected that the normalized quantities are not affected by the gap between the driver and the repeater.

As expected, the normalized effective inductances vary less than 0.5% from the normalizing constant for every curve in Figure 5.13a. For 0.4cm gap between the repeater and the copper plate, the variation is smaller than 0.05%.

Although the change in the normalized effective resistances is bigger than that of the normalized effective inductances, the variation is not significant enough to consider the gap between the driver and the repeater as an important parameter for the system response.

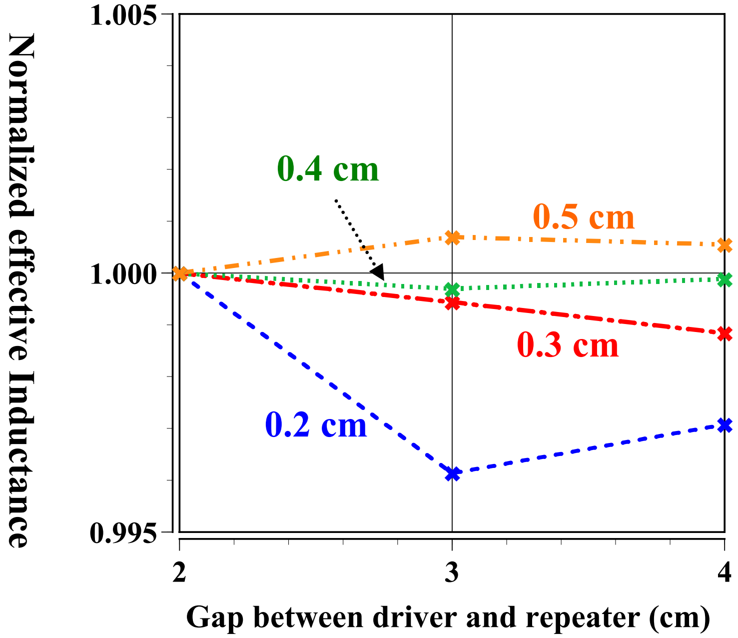

(a)

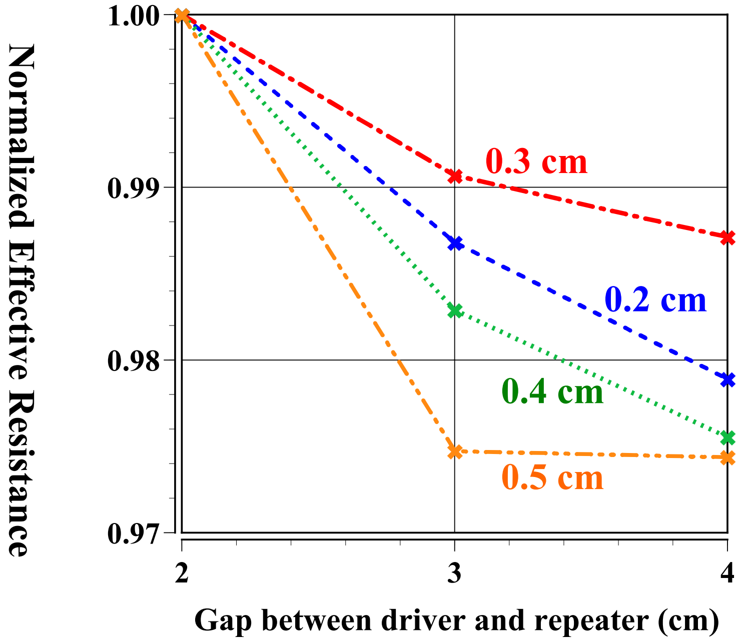

(b)

Figure 5.13: The normalized quantities derived from the same experiment data that are used to determine the resonant frequency, the maximum phase dip and the pseudoQ in section 5.2.3. (a) The normalized effective inductance. (b) The normalized effective resistance.

5.3.5 The slit length

The normalized effective inductance and resistance are plotted in Figure 5.14 when the slit length is the parameter for the experiment.

The normalized effective inductance does not vary much when the normalized slit length is less than 1. That is to say, the shift of the resonant frequency is not severe if the slit is within the radius of the repeater. However, the normalized effective inductance gradually increases as the slit becomes than the diameter of the repeater tag.

The normalized resistance increases abruptly when the slit is made on the copper plate, at the center of the repeater tag when viewed from above, as can be seen in Figure 5.14b. Surprisingly, the biggest variation comes from the first 4mm wide cut in the copper plate even if the slit is so small compared to the diameter of the repeater tag. The reason for the largest change in the first cut is that the magnetic field is strongest in the center of the repeater tag. Due to the strong magnetic field, there is a strong eddy current in the center. Even the small cut in the center has the induced eddy current flow around the cut, which makes the path, which it should flow along, much longer. Thus, even a small cut increases the normalized effective resistance very abruptly. After the first cut, the variation in the normalized resistance gradually rolls off and the normalized effective resistance culminates when the normalized slit length is about 0.75. The normalized effective resistance starts to be reduced noticeably after the peak value. However, the normalized effective resistance converges to a constant if the normalized slit length is larger than 2. Once the normalized effective resistance is saturated, the slit length does have little influence on it.

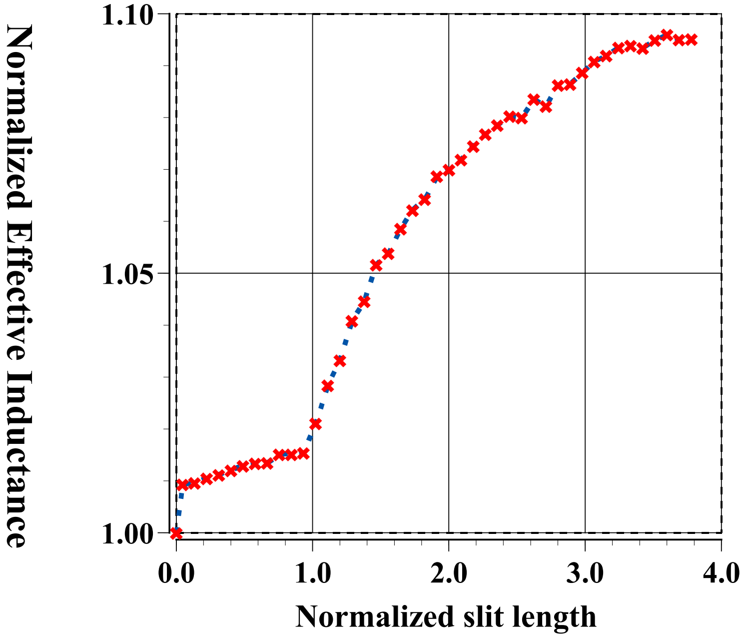

(a)

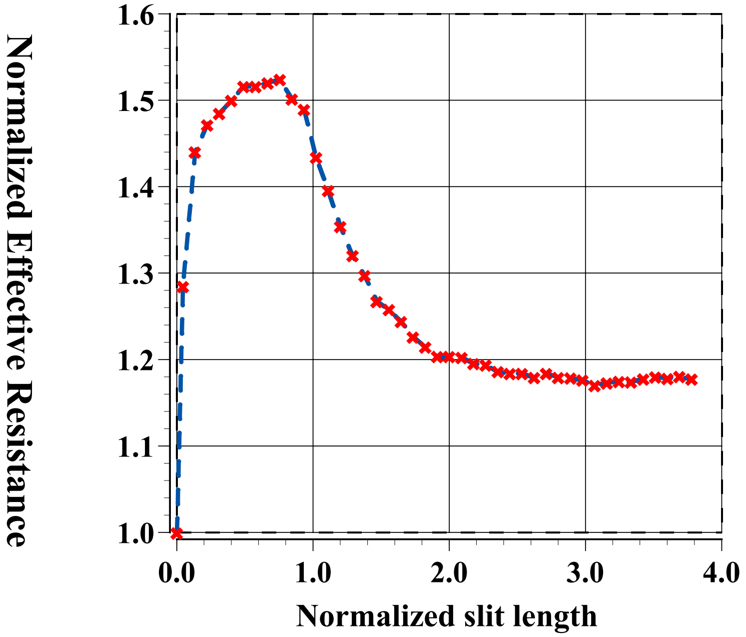

(b)

Figure 5.14: The normalized quantities derived from the same experiment data that are used to determine the resonant frequency, the maximum phase dip and the pseudoQ in section 5.2.4. (a) The normalized effective inductance. (b) The normalized effective resistance.

Chapter 6

Conclusion

The structural health monitoring is the process of implementing a damage detection strategy. The health monitoring provides a much better ways of maintaining stability of highly valuable structures through many technologies available recently. Among many of its possible applications, civil infrastructures can be maintained using the structural health monitoring to effectively sustain the reliability with the reasonable amount of cost. As a method of structural heath monitoring, the nondestructive testing technique can be utilized even though nondestructive testing methods may be said to be a little different from the structural health monitoring in a strict sense. Since the modern civil infrastructures are mostly built with structural steels or special moment resisting frames which often support whole structures, it is important to monitor the condition of those key units to ensure the proper performance of civil infrastructures. Thus, it is proposed to develop a sensor to be used for health monitoring of the civil infrastructures based on the present eddy current nondestructive testing technique. To overcome the limitation - short detection range and dependency on the surface roughness - of conventional eddy current technique, a passive repeater tag is devised which can be modeled equivalently as a series RLC resonant circuit.

To verify the idea of a passive repeater tag, a series of experiments has been carried out in the Chapter 2. As expected, the conventional eddy current technique was not successful in demonstrating the ability of identifying different conditions on a conducting medium. The result of preliminary experiment showed that the sensitivity could be much improved with the passive repeater tag as effective resonant frequency, which is not available in the conventional eddy current sensing scheme, is heavily influenced by the conditions of the copper plate.

As the inductance plays a central role in analyzing experimental results and finding equivalent circuits, a through review of inductance and mutual inductance was presented under quasi-static field assumption along with application of the rigorous definitions to practical aspect of calculations. For the comparison between the theoretical and measured inductance, the calibration process is discussed through which this parasitic due to the fixtures and cables can be removed. It is also shown that the predicted value from the theory on the inductance is very close to the measured one after the calibration. To exploit the property of very conductive DUT, such as the structural steels or special moment resisting frames, the image theory was covered with many examples. In addition, it can be concluded that the image theory is consistent with the actual measurement data.

In Chapter 4, three measures are employed to characterize the response from sets of experiment. They are effective resonant frequency, maximum phase dip, and pseudo quality factor. In terms of the characteristics, various experimental results have been analyzed. The thickness of the metallic DUT does not have much influence on characteristics of the response only if it is thicker than the skin depth. Hardly the gap between the driver and the repeater tag impacts the responses. However, the response is very dependent on the gap between the repeater tag and the DUT, or the slit length on the metallic DUT. To gain an insight into the dependence of the effective inductance and loss on the variation of parameters, new measurands, the effective normalized inductance and resistance, were devised and employed to reanalyze the same experimental data.

Based upon the theory of self and mutual inductance and the image theory, an effort to construct equivalent circuit model of the system has been made. Our approach utilized a black box in the equivalent circuit to remove the discrepancy since there is always possibility of discrepancy between the theory and actual measurement using an impedance analyzer. To make things simple, the equivalent circuit for the simplest system was made first and then more complex one was done based on the simpler one which is constructed before. To test as many combinations of the repeater tags and DUTs, the total 4 types of tags and 6 types of DUT were built and tested. The extracted real and imaginary part of the black box was given in the plots. Based on the data, it can be inferred that the repeater tag is a sensitivity enhancer since all the plots are indistinguishable except for the case when the repeater tag was used.

Bibliography

[1] M. Chang, H. Lee, and I. Akiyama, "Image reconstruction and enhancement for subsurface radar imaging using wavefield statistics," in Signals, Systems and Computers, 1994. 1994 Conference Record of the Twenty-Eighth Asilomar Conference on, 1994, pp. 1200-1204 vol.2.

[2] M. Schickert, "Ultrasonic NDE of concrete," in *Ultrasonics Symposium, 2002. Proceedings. 2002 IEEE*, 2002, pp. 739-748 vol.1.

[3] M. Chang, P. Chou, and H. Lee, "Tomographic microwave imaging for nondestructive evaluation and object recognition of civil structures and materials," in *Signals, Systems and Computers, 1995. 1995 Conference Record of the Twenty-Ninth Asilomar Conference on*, 1995, pp. 1061-1065 vol.2.

[4] S.-C. Wooh and Y. Shi, "Synthetic phase tuning of guided waves," *Ultrasonics, Ferroelectrics and Frequency Control, IEEE Transactions on,* vol. 48, pp. 209-223, 2001.

[5] S. K. Sinha, A. J. Schokker, and S. R. Iyer, "Non-contact ultrasonic imaging for post-tensioned bridges to investigate corrosion and void status," in *Sensors, 2003. Proceedings of IEEE*, 2003, pp. 487-492 Vol.1.

[6] J. T. Bernhard, K. Hietpas, E. George, D. Kuchima, and H. Reis, "An interdisciplinary effort to develop a wireless embedded sensor system to monitor and assess corrosion in the tendons of prestressed concrete girders," in *Wireless Communication Technology, 2003. IEEE Topical Conference on*, 2003, pp. 241-243.

[7] B. Sherwood, "Long submerged tunnel inspections: the Mantaro headrace tunnel, Central Andes Mountains, Peru," in *OCEANS '95. MTS/IEEE. 'Challenges of Our Changing Global Environment'. Conference Proceedings.*, 1995, pp. 2008-2012 vol.3.

[8] S. A. Wenk, R. C. McMaster, and P. McIntire, *Choosing NDT : applications, costs and benefits of nondestructive testing in your quality assurance program*. [Columbus, OH]: American Society for Nondestructive Testing, 1987.

[9] S. A. Wenk and R. C. McMaster, "A Basic Guide for amanagement's Choice of Nondestructive Tests," American Society for Testing and Materials Philadelphia, PA, Special Technical Publication No. 112. 1951.

[10] R. C. McMaster, *Nondestructive testing handbook*, 2nd ed. Columbus, Ohio : American Society for Nondestructive Testing: [Metals Park, Ohio], 1982.

[11] J. A. Tegopoulos and E. E. Kriezis, *Eddy currents in linear conducting media*. Amsterdam: New York, 1985.

[12] R. L. Stoll, *The analysis of eddy currents*. Oxford: Clarendon Press, 1974.

[13] D. Weissenburger and U. Christensen, "A network mesh method to calculate eddy currents on conducting surfaces," *Magnetics, IEEE Transactions on,* vol. 18, pp. 422-425, 1982.

[14] M. T. Thompson, "Eddy current magnetic levitation. Models and experiments," *Potentials, IEEE,* vol. 19, pp. 40-44, 2000.

[15] A. Richer and A. Adler, "Eddy Current Based Flexible Sensor for Contactless Measurement of Breathing," 2005, pp. 257-260.

[16] H. Takashima, M. Tomita, C. Zhiqian, M. Satoh, S. Doki, and S. Okuma, "Sensorless position and velocity control of cylindrical brushless," 2002, pp. 1300-1303 vol.3.

[17] E. M. Purcell, *Electricity and magnetism*, 2nd ed. New York: McGraw-Hill, 1985.

[18] "Encyclopaedia Britannica Online," Encyclopaedia Britannica,Inc., http://www.britannica.com, 2005.

[19] "Foucault's disk", http://physics.kenyon.edu/EarlyApparatus/Electricity/Foucaults_Disk/Foucaults_Disk.html.

[20] J. F. C. Chang and S. Bakhtiari, "Finite-element modeling of eddy-current probe for NDE of steam generator tubes," http://www.osti.gov/servlets/purl/791158-GZJYRV/native/, 2002.

[21] R. J. Kurtz, P. G. Heasler, and C. M. Anderson, "Performance demonstration tests for eddy current inspection of steam generator tubing," http://www.osti.gov/servlets/purl/257304-03MIvb/webviewable/, 2001.

[22] S. Bakhtiari, "Advanced Eddy current NDE steam generator tubing," http://www.osti.gov/servlets/purl/11731-L8ClWM/webviewable/, 2001.

[23] "Eddy Current Inspection of Heat Exchanger Tubing," Force Technology, http://www.force.dk/NR/rdonlyres/6B2B3133-7705-44F5-A593-655F5A7DB990/186/17571en2.pdf, 2005.

[24] "Thickness Measurements of Nonconducting Coatings on Conductive Materials," NDT Resource Center, http://www.ndt-ed.org/EducationResources/CommunityCollege/EddyCurrents/Applications/thicknessmeasurements2.htm, 2005.

[25] J. Hansen, "The eddy current inspection method: Part 4. Applications, practical testing and advanced concepts," *Insight,* vol. 46, 2004.

[26] J. Hansen, "The eddy current inspection method: Part 1. History and electrical theory," *Insight,* vol. 46, 2004.

[27] D. M. Pozar, *Microwave engineering*, 2nd ed.: Wiley, 1997.

[28] D. J. Griffiths, *Introduction to electrodynamics*, 2nd ed. Englewood Cliffs, N.J.: Prentice Hall, 1989.

[29] E. Bogatin, *Signal integrity-- simplified*. Upper Saddle River, NJ: Prentice Hall, 2004.

[30] H. Greenhouse, "Design of Planar Rectangular Microelectronic Inductors," *Parts, Hybrids, and Packaging, IEEE Transactions on,* vol. 10, pp. 101-109, 1974.

[31] A. E. Ruehli, N. Kulasza, and J. Pivnichny, "Inductance of Nonstraight Conductors Close to Ground Return Plane (Short Papers)," *Microwave Theory and Techniques, IEEE Transactions on,* vol. 23, pp. 706-708, 1975.

[32] A. E. Ruehli, "Inductance calculations in a complex integrated circuit environment," *IBM Journal of Research and Development,* vol. 16, pp. 470-481, 1972.

[33] P. A. Brennan, N. Raver, and A. E. Ruehli, "Three-dimensional inductance computations with partial element eqivalent circuits," *IBM Journal of Research and Development,* vol. 23, pp. 661-667, 1979.

[34] A. C. Cangellaris, J. L. Prince, and L. P. Vakanas, "Frequency-dependent inductance and resistance calculation for three-dimensional structures in high-speed interconnect systems," *Components, Hybrids, and Manufacturing Technology, IEEE Transactions on [see also IEEE Trans. on Components, Packaging, and Manufacturing Technology, Part A, B, C],* vol. 13, pp. 154-159, 1990.

[35] W. T. Weeks, L. L. Wu, M. F. McAllister, and A. Singh, "Resistive and inductive skin effect in rectangular conductors," *IBM Journal of Research and Development,* vol. 23, pp. 652-660, 1979.

[36] F. W. Grover, *Inductance calculations : working formulas and tables*. New York: D. Van Nostrand, 1946.

[37] I. V. Lindell, *Methods for electromagnetic field analysis*: Clarendon Press ;; New York :; Oxford University Press, 1992.

[38] I. V. Lindell, "Application of the image concept in electromagnetism," in *The Review of radio science, 1990-1992* Oxford: New York, 1993, pp. 107-126.

[39] W. T. B. Kelvin, *Reprint of papers on electrostatics and magnetism*: London Macmillan, 1872.

[40] M. H. Nayfeh and M. K. Brussel, *Electricity and magnetism*. New York: Wiley, 1985.

[41] H. A. M. J. R. Haus, *Electromagnetic fields and energy*. Englewood Cliffs, N.J.: Prentice Hall, 1989.

[42] L. O. Chua, C. A. Desoer , and E. S. Kuh, *Linear and nonlinear circuits*. New York: McGraw-Hill, 1987.

[43] "Discussions with Dean P. Neikirk," 2006.

Vita

Byungki Woo was born in Taegu, Korea, on August 1, 1969, the first son of Kyungkoo Woo and Seokhee Lee. He graduated from Keisung High School in February 1988. He received B.S. in Material Engineering from the Seoul Nation University, Seou, Korea, in February 1995 and the master's degree in electrical and computer engineering from the University of Texas, Austin, in 2001. Since September 1999 he has worked as a research assistant under supervision of Professor Dean P. Neikirk.

Permanent address: 3353 Lake Austin Blvd. Apt.#D
Austin, TX 78703
This dissertation was typed by the author